

**Silicon Detector Characterisation for Electron  
Spectroscopy: From keV Conversion Electrons to  
MeV Electron-Positron Pairs**

**Alan Devlin**

**Supervisors: Dr. Tibor Kibédi, Dr. Andrew Stuchbery, Dr. Anna Wilson**

**A thesis submitted for the degree of  
Master of Philosophy  
of The Australian National University**

**October, 2009**



Silicon Detector Characterisation for Electron  
Spectroscopy: From keV Conversion Electrons to  
MeV Electron-Positron Pairs

Alan Devlin

Supervisors: Dr. Tibor Kibédi, Dr. Andrew Stubbery, Dr. Angus Wilson

A thesis submitted for the degree of  
Master of Philosophy  
of The Australian National University

October, 2009

---

# Declaration

---

This thesis is an account of research undertaken between January 2008 and October 2009 at the Department of Nuclear Physics, Faculty of Science, the Australian National University, Canberra, Australia.

Except where acknowledged in the customary manner, the material presented in this thesis is, to the best of my knowledge, original and has not been submitted in whole or part for a degree in any university.



Alan Devlin

October, 2009

# Declaration

This thesis is a result of research undertaken between January 2005 and October 2009 at the Department of Nuclear Physics, Faculty of Science, the Australian National University, Canberra, Australia.

I declare that where acknowledged in the acknowledgments, the material presented in this thesis is, to the best of my knowledge, original and has not been submitted in whole or part for a degree in any university.



Alan P. Van  
October 2009

---

# Acknowledgements

---

I would like to humbly acknowledge the people around me without whom I could not have completed this. I would like to thank my supervisors: Dr. Tibor Kibèdi, Dr. Andrew Stuchbery and Dr. Anna Wilson for their help and guidance throughout the course of my research, and wish them all the best in future endeavours. I would like to thank other members of the department, Prof. George Dracoulis, Michael East and Petra Rickman, and the technical staff, for their help and involvement in the project. Thanks to Alex for her support and advice, and for putting up with me. I would also like to thank my parents, who managed to read this through without a physics degree. Thanks also to my house-mates Wesley Cox and Adam Mullavey, Australia's next Nobel prize winners.

## Acknowledgements

---

I would like to thank a number of people around me without whom I could not have completed this. I would like to thank my supervisors, Dr. Tibor Koppell, Dr. Andrew Fletcher and Dr. Adam White for their help and guidance throughout the course of my research and will keep an the best in their endorsement. I would like to thank other members of the department, Prof. George Orsi, Robert Hart and Peter Hickman, and the technical staff for their help and involvement in the project. Thanks to Alex for his support and advice and for putting up with me. I would also like to thank my parents who managed to read this through without a single hiccup. Thanks also to my friends in the West, Oz and Adam Maloney, Australia's next Nobel prize winners.

---

# Abstract

---

An investigation into the response of Si(Li) detectors for electron spectroscopy was carried out, to provide calibration for a proposed measurement of the radiative width of the Hoyle state in  $^{12}\text{C}$ , and to aid in the design of detectors in the future. The approach was to use Monte Carlo simulations, providing a cost-effective and reliable method of detector characterisation. The characterisation here was carried out to model proposed detector uses for both internal conversion spectroscopy in the range 20 keV - 1 MeV, and electron-positron pair spectroscopy, in the range 1 MeV to 3.5 MeV. Of interest is not only the response to electrons and positrons, but also to photons (both X-rays and  $\gamma$ -rays), as they make up the majority of the background intensity. The aim was to use the simulations to not only predict efficiency and sensitivity to background, but also the lineshape, using the Monte Carlo program PENELOPE [1]. Modifications were made to the program to reproduce charge collection effects, electronic noise, and the spatial distribution of the source. The simulation system was tested by comparing an experimental measurement of a  $^{133}\text{Ba}$  source to a simulation with identical detector geometry and input radiations. The comparison showed a close agreement with experiment in lineshapes, efficiency and sensitivity to background. Extensive simulations and a  $^{56}\text{Co}$  measurement were used to extend the characterisation up to 3.5 MeV, and derive an empirical formula for the efficiency of a 1 cm thick Si(Li) detector as a function of energy and incident angle for energies in the range  $10 \text{ keV} \leq E \leq 3.5 \text{ MeV}$  and angles in the range  $0^\circ \leq \theta \leq 60^\circ$ . The results also provide insight into the causes of efficiency loss in Si(Li) detectors over a wide energy range. At high energy, the escape of bremsstrahlung photons from the back of the detector was found to be the dominant form of energy loss; this, along with other important results of the present study are generally applicable to electron spectroscopy measurements over the specified energy range.

## Abstract

An investigation into the response of  $^{252}\text{Cf}$  detectors to electron spectroscopy was carried out to provide calibration for a practical measurement of the relative yields of the fission products in  $^{252}\text{Cf}$ , and to aid in the design of detectors for the future. The present work is to use Monte Carlo simulation, providing a quantitative and reliable method of detector characterization. The characterization was carried out to model proposed detector uses for both internal conversion spectroscopy in the range 30 keV - 1 MeV, and electron-positron pair spectroscopy in the range 1 MeV to 5.5 MeV. Of interest is not only the response to electrons and positrons, but also to photons (with X-rays and  $\gamma$ -rays) as they make up the majority of the background intensity. The aim was to give the simulation to not only predict efficiency and sensitivity to background, but also the hardware, using the Monte Carlo program GEANT4. Modifications were made to the program to reproduce charge collector effects, electronic noise, and the partial detection of the source. The simulation system was tested by comparing an experimental measurement of a  $^{252}\text{Cf}$  source to a simulation with identical detector geometry and input conditions. The comparison showed a close agreement with experiment in detection efficiency and sensitivity to background. Extensive simulations and a  $^{252}\text{Cf}$  measurement were used to extend the characterization up to 5.5 MeV, and derive an optimal geometry for the efficiency of a 1 cm thick  $^{252}\text{Cf}$  detector as a function of energy and incident angle. The results also provide insight into the causes of efficiency loss in  $^{252}\text{Cf}$  detectors over a wide energy range. At high energy, the escape of bremsstrahlung photons from the back of the detector was found to be the dominant form of energy loss, this along with other important results of the present study are generally applicable to electron spectroscopy measurements over the specified energy range.



---

# Contents

---

<b>Declaration</b>	<b>iii</b>
<b>Acknowledgements</b>	<b>v</b>
<b>Abstract</b>	<b>vii</b>
<b>1 Introduction</b>	<b>1</b>
1.1 Why Electron Spectroscopy? . . . . .	1
1.2 Why $^{12}\text{C}$ ? . . . . .	3
1.3 The Experimental Challenge: Outline of Present Work . . . . .	5
1.4 Recent Progress in Electron Spectroscopy . . . . .	6
<b>2 Experiment</b>	<b>9</b>
2.1 Fundamental Concepts in Detector Characterisation . . . . .	9
2.2 Semiconductor Detectors . . . . .	10
2.2.1 Lithium-Drifted Silicon Diodes - Si(Li) . . . . .	11
2.3 Lineshapes . . . . .	12
2.3.1 Intrinsic Semiconductor Resolution . . . . .	14
2.3.2 Energy Straggling . . . . .	17
2.3.3 Incomplete Energy Deposition . . . . .	18
2.4 Experimental Measurements . . . . .	21
2.5 Experimental Apparatus . . . . .	22
2.5.1 Further Details of Setup (a) From Figure ?? . . . . .	22
2.5.2 Further Details of Setup (b) From Figure ?? . . . . .	23
2.5.3 Honey . . . . .	23
2.5.4 SEPH-530 . . . . .	24
2.6 $^{133}\text{Ba}$ Source Experiment . . . . .	24
2.6.1 Source Preparation . . . . .	27
2.6.2 Data Collection . . . . .	28
2.7 $^{56}\text{Co}$ Source Experiment . . . . .	31

---

2.7.1	Source Preparation . . . . .	34
2.7.2	Data Collection . . . . .	35
<b>3</b>	<b>Simulation with PENELOPE</b>	<b>39</b>
3.1	Electrons and Positrons . . . . .	39
3.1.1	The Treatment of Elastic Scattering in PENELOPE . . . . .	40
3.1.2	Inelastic Scattering in PENELOPE . . . . .	47
3.1.3	Bremsstrahlung . . . . .	56
3.1.4	Positron Annihilation . . . . .	60
3.1.5	Cross Sections . . . . .	61
3.2	PENELOPE Physics: Photons . . . . .	61
3.2.1	Coherent (Rayleigh) Scattering . . . . .	62
3.2.2	Photoelectric Absorption . . . . .	64
3.2.3	Incoherent (Compton) Scattering . . . . .	65
3.2.4	Electron - Positron Pair Production . . . . .	67
3.2.5	Attenuation Coefficients . . . . .	67
3.3	Monte Carlo Simulations . . . . .	67
3.3.1	Mixed Simulation . . . . .	71
3.3.2	Sampling Methods . . . . .	72
3.3.3	Inverse-Transform Method . . . . .	72
3.4	The Input Files for PENELOPE . . . . .	75
3.4.1	Geometry . . . . .	75
3.4.2	Input File . . . . .	77
<b>4</b>	<b>Results</b>	<b>79</b>
4.1	Experimental Setup for the $^{133}\text{Ba}$ Monte Carlo Measurement . . . . .	79
4.1.1	Geometry . . . . .	82
4.1.2	Simulation Parameters . . . . .	82
4.2	Comparison of the $^{133}\text{Ba}$ Simulation and Experimental Results . . . . .	84
4.2.1	Statistics and Calibration . . . . .	84
4.2.2	Comparison of the Photon Spectra . . . . .	84
4.2.3	Comparison of the Electron Spectra . . . . .	85
4.2.4	Comparison of the Lineshape Parameters . . . . .	85
4.3	$^{133}\text{Ba}$ Monte Carlo Measurement Using a “Dead Layer” Honey Geometry . . . . .	89

4.3.1	Inspection of Figure ?? . . . . .	90
4.3.2	Low Energy Offset and Arguments For and Against the Dead Layer . . . . .	90
4.3.3	Comparison of Experimental and Simulation Lineshape Parameters . . . . .	92
4.3.4	Photon Background . . . . .	95
4.4	Efficiency as Function of Energy . . . . .	96
4.5	Empirical Formula for Efficiency as a Function of Energy and Angle . . . . .	102
4.6	Future Directions . . . . .	110
<b>5</b>	<b>Conclusions</b> . . . . .	<b>113</b>
	<b>Bibliography</b> . . . . .	<b>115</b>
<b>A</b>	<b>PENELOPE Geometry Input File for the Honey Detector Array</b> . . . . .	<b>121</b>
<b>B</b>	<b>PENELOPE Input File for the <sup>133</sup>Ba Electron Measurement</b> . . . . .	<b>125</b>
<b>C</b>	<b>PENELOPE Output File</b> . . . . .	<b>129</b>
<b>D</b>	<b>PENELOPE Output Spectrum File</b> . . . . .	<b>131</b>

10	1.1.1 Properties of Matter	10
20	1.1.2 Low Energy of Matter	20
30	1.1.3 Conservation of Momentum and Energy	30
40	1.1.4 Kinematics of Matter	40
50	1.1.5 Dynamics of Matter	50
60	1.1.6 Angular Momentum for Matter	60
70	1.1.7 Mass and Energy	70
80	1.1.8 Quantum Mechanics	80
90	1.1.9 Relativity	90
100	1.1.10 The Standard Model	100
110	1.1.11 The Future of Physics	110
120	2. Conclusions	120
130	3. Bibliography	130
140	4. Appendix A: Geometry of the Hyper-Bolton Sphere	140
150	4.1.1 The Hyper-Bolton Sphere	150
160	4.1.2 The Hyper-Bolton Sphere	160
170	4.1.3 The Hyper-Bolton Sphere	170
180	4.1.4 The Hyper-Bolton Sphere	180
190	4.1.5 The Hyper-Bolton Sphere	190
200	4.1.6 The Hyper-Bolton Sphere	200
210	4.1.7 The Hyper-Bolton Sphere	210
220	4.1.8 The Hyper-Bolton Sphere	220
230	4.1.9 The Hyper-Bolton Sphere	230
240	4.1.10 The Hyper-Bolton Sphere	240
250	4.1.11 The Hyper-Bolton Sphere	250
260	4.1.12 The Hyper-Bolton Sphere	260
270	4.1.13 The Hyper-Bolton Sphere	270
280	4.1.14 The Hyper-Bolton Sphere	280
290	4.1.15 The Hyper-Bolton Sphere	290
300	4.1.16 The Hyper-Bolton Sphere	300
310	4.1.17 The Hyper-Bolton Sphere	310
320	4.1.18 The Hyper-Bolton Sphere	320
330	4.1.19 The Hyper-Bolton Sphere	330
340	4.1.20 The Hyper-Bolton Sphere	340
350	4.1.21 The Hyper-Bolton Sphere	350
360	4.1.22 The Hyper-Bolton Sphere	360
370	4.1.23 The Hyper-Bolton Sphere	370
380	4.1.24 The Hyper-Bolton Sphere	380
390	4.1.25 The Hyper-Bolton Sphere	390
400	4.1.26 The Hyper-Bolton Sphere	400
410	4.1.27 The Hyper-Bolton Sphere	410
420	4.1.28 The Hyper-Bolton Sphere	420
430	4.1.29 The Hyper-Bolton Sphere	430
440	4.1.30 The Hyper-Bolton Sphere	440
450	4.1.31 The Hyper-Bolton Sphere	450
460	4.1.32 The Hyper-Bolton Sphere	460
470	4.1.33 The Hyper-Bolton Sphere	470
480	4.1.34 The Hyper-Bolton Sphere	480
490	4.1.35 The Hyper-Bolton Sphere	490
500	4.1.36 The Hyper-Bolton Sphere	500
510	4.1.37 The Hyper-Bolton Sphere	510
520	4.1.38 The Hyper-Bolton Sphere	520
530	4.1.39 The Hyper-Bolton Sphere	530
540	4.1.40 The Hyper-Bolton Sphere	540
550	4.1.41 The Hyper-Bolton Sphere	550
560	4.1.42 The Hyper-Bolton Sphere	560
570	4.1.43 The Hyper-Bolton Sphere	570
580	4.1.44 The Hyper-Bolton Sphere	580
590	4.1.45 The Hyper-Bolton Sphere	590
600	4.1.46 The Hyper-Bolton Sphere	600
610	4.1.47 The Hyper-Bolton Sphere	610
620	4.1.48 The Hyper-Bolton Sphere	620
630	4.1.49 The Hyper-Bolton Sphere	630
640	4.1.50 The Hyper-Bolton Sphere	640
650	4.1.51 The Hyper-Bolton Sphere	650
660	4.1.52 The Hyper-Bolton Sphere	660
670	4.1.53 The Hyper-Bolton Sphere	670
680	4.1.54 The Hyper-Bolton Sphere	680
690	4.1.55 The Hyper-Bolton Sphere	690
700	4.1.56 The Hyper-Bolton Sphere	700
710	4.1.57 The Hyper-Bolton Sphere	710
720	4.1.58 The Hyper-Bolton Sphere	720
730	4.1.59 The Hyper-Bolton Sphere	730
740	4.1.60 The Hyper-Bolton Sphere	740
750	4.1.61 The Hyper-Bolton Sphere	750
760	4.1.62 The Hyper-Bolton Sphere	760
770	4.1.63 The Hyper-Bolton Sphere	770
780	4.1.64 The Hyper-Bolton Sphere	780
790	4.1.65 The Hyper-Bolton Sphere	790
800	4.1.66 The Hyper-Bolton Sphere	800
810	4.1.67 The Hyper-Bolton Sphere	810
820	4.1.68 The Hyper-Bolton Sphere	820
830	4.1.69 The Hyper-Bolton Sphere	830
840	4.1.70 The Hyper-Bolton Sphere	840
850	4.1.71 The Hyper-Bolton Sphere	850
860	4.1.72 The Hyper-Bolton Sphere	860
870	4.1.73 The Hyper-Bolton Sphere	870
880	4.1.74 The Hyper-Bolton Sphere	880
890	4.1.75 The Hyper-Bolton Sphere	890
900	4.1.76 The Hyper-Bolton Sphere	900
910	4.1.77 The Hyper-Bolton Sphere	910
920	4.1.78 The Hyper-Bolton Sphere	920
930	4.1.79 The Hyper-Bolton Sphere	930
940	4.1.80 The Hyper-Bolton Sphere	940
950	4.1.81 The Hyper-Bolton Sphere	950
960	4.1.82 The Hyper-Bolton Sphere	960
970	4.1.83 The Hyper-Bolton Sphere	970
980	4.1.84 The Hyper-Bolton Sphere	980
990	4.1.85 The Hyper-Bolton Sphere	990
1000	4.1.86 The Hyper-Bolton Sphere	1000

---

# List of Figures

---

1.1	The triple alpha process, leading to the stellar formation of $^{12}\text{C}$ , and the subsequent electromagnetic decays from the Hoyle state. . . . .	3
1.2	Mechanisms for the electromagnetic decay of excited nuclear states. . . . .	4
2.1	The range of electrons and positrons in silicon [8]. . . . .	11
2.2	An example of the contributions to lineshape of a typical conversion-electron peak. The contributions from energy straggling, incomplete energy deposition, electronic noise, semiconductor effects and room background are summed to give the lineshape. . . . .	13
2.3	A schematic of electron detection. An electron, emitted from a nucleus with energy $E_0$ loses energy in the source ( $\Delta E_s$ ), and in the front electrode ( $\Delta E_{det}$ ) and deposits an energy signal $E = E_0 - \Delta E_s - \Delta E_{det}$ in the detector. . . . .	13
2.4	Incomplete energy deposition: (i) Secondary photon transmission ( $T_\gamma$ ): a primary electron ( $e_p^-$ ) interacts with the detector material and produces a secondary photon, $\gamma_s$ , which is transmitted (ii) Primary electron backscattering ( $\rho_{pb}$ ): a primary electron interacts with the detector material and is backscattered (iii) Secondary electron transmission ( $T_{se}$ ): a primary electron suffers interactions and produces a number of secondary electrons $e_s^-$ , one of which is transmitted. . . . .	19
2.5	Cross sectional view of the experimental setups used for the $^{133}\text{Ba}$ radioactive source measurements. Red lines indicate the envelope of the spectrometer acceptance. (a) Honey electron array to obtain the mixed photon and conversion-electron data. (b) Magnetic spectrometer used to obtain the electron spectrum. . . . .	22
2.6	The front dimensions of the Honey detector. . . . .	24
2.7	The efficiency as a function of energy for the Honey detector. . . . .	28

---

2.8	The efficiency of the magnetic spectrometer and SEPH-530 detector. Points: experimental efficiencies from the $^{133}\text{Ba}$ source experiment; Solid curve: Transport efficiency, calculated by integrating the momentum window over the current range and normalising to the experimental data. . . . .	29
2.9	$^{133}\text{Ba}$ energy spectra. Top panel: Mixed photon and electron spectrum, measured with Honey; Middle panel: Electron spectrum, measured with the SEPH-530, combined with the Lens spectrometer; Bottom panel: Pure photon spectrum deduced by subtracting the middle panel from the top panel; the features labeled * are artifacts of the subtraction. . . . .	30
2.10	Blue: $^{56}\text{Co}$ electron spectrum, black: background, *: unidentified contaminants. The magnet current was swept between 2.7 A and 12.6 A. . . . .	36
2.11	$^{56}\text{Co}$ electron spectrum, after background subtraction, *: unidentified contaminants. . . . .	37
3.1	Basic types of interaction of electrons with matter. . . . .	40
3.2	Electron interaction cross sections for silicon. . . . .	41
3.3	Electron interaction mean free paths for silicon. . . . .	42
3.4	Positron interaction cross sections for silicon. . . . .	43
3.5	Positron interaction mean free paths for silicon. . . . .	44
3.6	Calculated differential cross sections for elastic scattering of electrons (solid lines) and positrons (dashed lines) calculated by ELSEPA for silicon assuming the Dirac-Fock electron-density function and the point nucleus model [49]. The dotted line shows the relativistic Rutherford cross section. Energy of: (a) 500 eV; (b) 5000 eV; (c) 30 keV; and (d) 100 MeV. . . . .	46
3.7	Radiative and collisional stopping powers of silicon for electrons [8]. The radiative or bremsstrahlung stopping power becomes dominant for high energy. . . . .	57
3.8	Radiative and collisional stopping powers of silicon for positrons [8]. The radiative or bremsstrahlung stopping power becomes dominant for high energy. . . . .	58
3.9	Interactions of photons with matter. . . . .	62
3.10	Photon interaction cross sections for silicon. . . . .	63
3.11	Photon mass attenuation coefficients for silicon. . . . .	64

---

3.12	Random sampling from a distribution $p(x)$ using the inverse-transform method. . . . .	72
3.13	Random sampling from a distribution $p(x)$ using rejection methods. . . . .	73
3.14	A possible cross section of a PENELOPE geometry and module, with geometry family tree. . . . .	76
4.1	Honey - front view, produced in PENELOPE, see appendix A. . . . .	80
4.2	Honey - cross sectional view, produced in PENELOPE, see appendix A. . . . .	80
4.3	Comparison of experimental (see section ??) and simulated spectra. In all cases, the simulation data were obtained by using the energies and intensities of radiations, taken from table ??, incident on the bare Honey detector. Mixed: bare Honey detector; Electron: SEPH-530 detector and Lens transporter; Photon: the difference: Mixed - Electron spectra. Artifacts of the subtraction process are marked with *. . . . .	83
4.4	Fit to part of the Honey data for $^{133}\text{Ba}$ , using the Fitek code. . . . .	85
4.5	Fitting parameters, obtained by fitting the simulated (open symbols) and experimental (filled symbols) electron spectra of figure ?. . . . .	86
4.6	The energy absorption of the source, according to the simulation. . . . .	87
4.7	Experimental and Simulation results assuming a $4\ \mu\text{m}$ dead layer of silicon on the front face of the Honey detector crystal; Artifacts of the subtraction process are indicated by *. . . . .	88
4.8	Simulation of the $^{133}\text{Ba}$ measurement for a $1\ \mu\text{m}$ silicon dead layer compared to the SEPH-530 experimental data. . . . .	91
4.9	Fitting Parameters, obtained by fitting the simulated (open symbols) and experimental, (filled symbols) electron spectra of figure ?. . . . .	93
4.10	Shown in black is the spectrum extracted from the Lens - SEPH-530 measurement, described in section ??, for a small window of the magnetic field, with the magnet current between 1.68A and 2.00A. The transmission of the Lens system for this current region is shown. Shown in pink is the comparable spectrum obtained by a simulation in PENELOPE. . . . .	94
4.11	Probability of incomplete energy deposition for a 1 cm thick Si(Li) detector, 1 million particle histories per point. Also shown are four points (1 MeV, 2 MeV, 3 MeV and 3.5 MeV), calculated for $0^\circ$ incidence on a 10 cm thick detector. . . . .	97

---

4.12 Sources of efficiency loss for the $0^\circ$ curve in figure ???. The contributions of secondary photon emission, secondary photon backscattering, primary electron backscattering, secondary electron backscattering and secondary electron transmission are shown. . . . .	98
4.13 Same as figure ??, but for $15^\circ$ incidence. . . . .	99
4.14 Same as figure ??, but for $30^\circ$ incidence. . . . .	100
4.15 Same as figure ??, but for $45^\circ$ incidence. . . . .	101
4.16 Same as figure ??, but for $60^\circ$ incidence. . . . .	102
4.17 Sources of efficiency loss plotted as a function of angle for an energy of 3.5 MeV. . . . .	103
4.18 Percentage of incomplete energy deposition as a function of incident angle, and energy, for electrons incident on a 4.3 mm detector (the thickness of the Honey detector). . . . .	104
4.19 Same as figure ??, but for positrons. . . . .	104
4.20 Simulated efficiency for electrons incident on a 10 mm silicon slab. . . . .	105
4.21 Fit to simulation data, from 10 keV to 200 keV. . . . .	105
4.22 Fit parameter $a_1$ in terms of $\cos \theta$ . . . . .	106
4.23 Fit to simulation data, from 200 to 3500 keV. . . . .	106
4.24 Fit parameter $b_3$ in terms of $\cos \theta$ . . . . .	107
4.25 Fit to efficiency as a function of energy and angle for electrons incident on a 10 mm silicon slab. . . . .	110



---

# List of Tables

---

2.1	Conversion-electron, Auger, X-ray and $\gamma$ -ray energies and intensities of the $^{133}\text{Ba}$ radioactive source. . . . .	24
2.1	continued . . . . .	25
2.1	continued . . . . .	26
2.2	Conversion-electrons, photons and pairs, emitted from $^{56}\text{Fe}$ with an intensity exceeding $1 \times 10^{-5}$ particles per 100 disintegrations of $^{56}\text{Co}$ . . . . .	31
2.2	continued . . . . .	32
2.2	continued . . . . .	33
2.2	continued . . . . .	34
4.1	Simulation parameters. . . . .	82
4.2	A sample spread of results, obtained by running the same simulation 10 times. . . . .	96
4.3	Fit parameters for the region $10 \text{ keV} \leq E \leq 200 \text{ keV}$ . . . . .	108
4.4	Fit parameters for the region $10 \text{ keV} \leq E \leq 200 \text{ keV}$ . . . . .	108
4.5	Fit parameters for the region $200 \text{ keV} \leq E \leq 3.5 \text{ MeV}$ . . . . .	109

---

LIST OF TABLES

---

1	Table 1.1	1
2	Table 1.2	2
3	Table 1.3	3
4	Table 1.4	4
5	Table 1.5	5
6	Table 1.6	6
7	Table 1.7	7
8	Table 1.8	8
9	Table 1.9	9
10	Table 1.10	10
11	Table 1.11	11
12	Table 1.12	12
13	Table 1.13	13
14	Table 1.14	14
15	Table 1.15	15
16	Table 1.16	16
17	Table 1.17	17
18	Table 1.18	18
19	Table 1.19	19
20	Table 1.20	20
21	Table 1.21	21
22	Table 1.22	22
23	Table 1.23	23
24	Table 1.24	24
25	Table 1.25	25
26	Table 1.26	26
27	Table 1.27	27
28	Table 1.28	28
29	Table 1.29	29
30	Table 1.30	30
31	Table 1.31	31
32	Table 1.32	32
33	Table 1.33	33
34	Table 1.34	34
35	Table 1.35	35
36	Table 1.36	36
37	Table 1.37	37
38	Table 1.38	38
39	Table 1.39	39
40	Table 1.40	40
41	Table 1.41	41
42	Table 1.42	42
43	Table 1.43	43
44	Table 1.44	44
45	Table 1.45	45
46	Table 1.46	46
47	Table 1.47	47
48	Table 1.48	48
49	Table 1.49	49
50	Table 1.50	50
51	Table 1.51	51
52	Table 1.52	52
53	Table 1.53	53
54	Table 1.54	54
55	Table 1.55	55
56	Table 1.56	56
57	Table 1.57	57
58	Table 1.58	58
59	Table 1.59	59
60	Table 1.60	60
61	Table 1.61	61
62	Table 1.62	62
63	Table 1.63	63
64	Table 1.64	64
65	Table 1.65	65
66	Table 1.66	66
67	Table 1.67	67
68	Table 1.68	68
69	Table 1.69	69
70	Table 1.70	70
71	Table 1.71	71
72	Table 1.72	72
73	Table 1.73	73
74	Table 1.74	74
75	Table 1.75	75
76	Table 1.76	76
77	Table 1.77	77
78	Table 1.78	78
79	Table 1.79	79
80	Table 1.80	80
81	Table 1.81	81
82	Table 1.82	82
83	Table 1.83	83
84	Table 1.84	84
85	Table 1.85	85
86	Table 1.86	86
87	Table 1.87	87
88	Table 1.88	88
89	Table 1.89	89
90	Table 1.90	90
91	Table 1.91	91
92	Table 1.92	92
93	Table 1.93	93
94	Table 1.94	94
95	Table 1.95	95
96	Table 1.96	96
97	Table 1.97	97
98	Table 1.98	98
99	Table 1.99	99
100	Table 1.100	100

---

# Introduction

---

This thesis describes the development of simulations aimed at supporting future measurements of electron-positron pairs emitted by the Hoyle state in  $^{12}\text{C}$ . In the following chapter, an explanation of the unique opportunities offered by electron spectroscopy is given, followed by a brief overview of the Hoyle state measurement. The experimental challenge addressed in the present work is then described.

## 1.1 Why Electron Spectroscopy?

In comparison to  $\gamma$ -ray studies, less progress has been made in pushing the limits for the detection electrons [2], however the need to develop more sophisticated electron detection systems is great. In the following we will focus on measurements of electrons from internal conversion and electron-positron pairs from pair production, and their applications to nuclear spectroscopy.

The probability that an excited nucleus decays via internal conversion (IC) increases with increasing atomic number ( $Z$ ) and with decreasing transition energy. This makes  $\gamma$ -ray spectroscopy less suitable for low-energy transitions in nuclei with high  $Z$  (where the transitions are highly converted) meaning electron spectroscopy can be crucial to observe these states. Furthermore, an experimental bias toward  $\gamma$  spectroscopy has hampered the study of odd mass nuclei and  $K \neq 0$  rotational bands in even-even nuclei where the probability of  $M1$  decay (which again have large conversion coefficients) becomes large compared to other electromagnetic modes [3]. The transition energies for the lowest states in the ground state rotational bands of well deformed, even-even nuclei with high mass cannot be measured using  $\gamma$ -ray spectroscopy, because the transitions are nearly fully converted. Traditionally, they are deduced by extrapolation from higher spins; electron spectroscopy allows the direct observation of these transitions.

The conversion electron or pair spectra can provide information beyond that which the  $\gamma$  spectrum alone provides:

1. *The observation of  $E0$  transitions.* Transitions between states of 0 angular momentum may only proceed via an  $E0$  transition. Low energy  $E0$  transitions are the signature of the decay between nuclear states with different intrinsic shapes [2]. The physics behind  $E0$  transitions is not fully resolved; they are known to be related to the rearrangement of charge in a nucleus, but the manner of the rearrangement is not fully understood.  $E0$  transitions may only proceed via IC or pair production ( $\gamma$ -ray emission is not allowed), so electron spectroscopy is critical for studying these transitions. A pure  $E0$  transition cannot emit any photons, therefore they cannot be observed using only the  $\gamma$  spectrum. An  $E0$  transition may be observed by comparison of the conversion electron and  $\gamma$  spectra. If the conversion-electron spectrum shows a conversion-electron peak and the  $\gamma$  spectrum shows no corresponding peak, the transition must be of pure  $E0$  character.

2. *Determination of the multipolarity.* The conversion coefficient, determined for a given transition, is

$$\alpha_i = \frac{I_{CE}}{I_\gamma}, \quad (1.1)$$

where  $I_\gamma$  and  $I_{CE}$  are the  $\gamma$ -ray and conversion-electron intensities respectively. The conversion coefficient  $\alpha_i(Z, E_\gamma, B(\pi, L))$  depends on  $Z, E_\gamma$ , and the multipolarity ( $B(\pi, L)$ ). Measurements of  $\alpha_i$  can usually determine, or at least help determine, the multipolarity of the transition.

3. *Determination of the atomic number  $Z$ .* The  $\gamma$  - conversion-electron coincidence data can be used to determine  $Z$  of the nucleus emitting the radiation. This is important in beam experiments, where the desired products may be obscured by strong competing reaction channels, prompt fission products, *etc.*. Gating on a  $\gamma$ -ray will show the conversion lines that are in coincidence (from the same nucleus). The energy differences between the K, L, and M conversion lines and the corresponding  $\gamma$ -ray are the K, L, and M binding energies, which give  $Z$  directly.

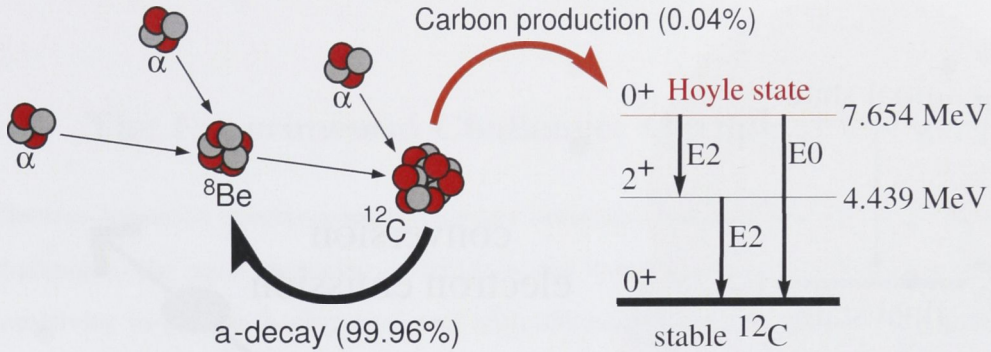


**Figure 1.1:** The triple alpha process, leading to the stellar formation of  $^{12}\text{C}$ , and the subsequent electromagnetic decays from the Hoyle state.

4. *Observation of the energy of a transition when the  $\gamma$  data cannot provide it.* In heavy atoms, the atomic X-ray emissions tend to be high in energy compared with low- $Z$  nuclei, and may interfere with the  $\gamma$ -ray spectrum from nuclear decay in the desired energy region. The electron spectrum may reveal a transition whose  $\gamma$ -ray is obscured by an X-ray because (i) the conversion-electron peaks are lower in energy (by the binding energy of each shell) and therefore may be in a clearer part of the spectrum, and (ii) with magnetic transportation the electron detector can be shielded from the X-rays.

## 1.2 Why $^{12}\text{C}$ ?

Carbon is created in the universe via the triple-alpha process (see figure 1.1), occurring in red giant stars. The rate of this process is known with an uncertainty of 12.5% [4]. The large uncertainty is a stumbling block in developing stellar evolution models. The rate cannot be predicted accurately by theoretical models, as the Hoyle state, at 7.654 MeV, and the states to which it decays, the 4.439 MeV  $2^+$  state and the  $0^+$  ground state, are very different in structure. The current theoretical treatments based on the shell model, do not describe both states and the transition between them in a reliable way. For example, in the most sophisticated no-core shell model calculations [5] the first excited  $0^+$  state is predicted at around 18 MeV. A proposed experiment at the ANU aims to measure the rate of the triple alpha-process with an uncertainty of 3%.

As shown in figure 1.1, once formation of the Hoyle state occurs, an estimated 99.96% of the time it will decay via spontaneous alpha emission. Only the remaining 0.04% will

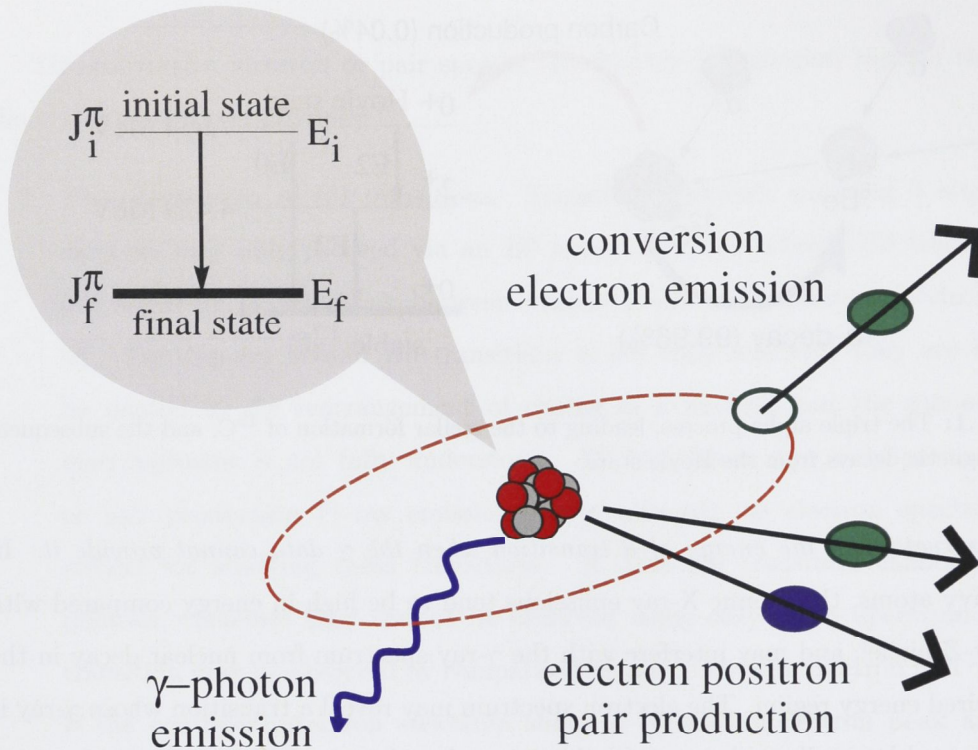


**Figure 1.2:** Mechanisms for the electromagnetic decay of excited nuclear states.

result in the formation of stable carbon in the Hoyle state. The excited nucleus will decay by one of the electromagnetic mechanisms shown in figure 1.2, namely photon emission, electron-positron pair production and conversion-electron emission.  $E2$   $\gamma$  emission to the first  $2^+$  state is the dominant decay branch, accounting for 98.5% of the decay intensity [6], with the remaining intensity almost completely shared between the  $E0$  pairs (1.5%) and the  $E2$  pairs (0.09%). The novel experimental approach proposed [7] hinges upon the accurate determination of the ratio  $\Gamma_{e^+e^-}^{E2}/\Gamma_{e^+e^-}^{E0}$ , where  $\Gamma_{e^+e^-}^{E2}$  is the rate of formation of  $E2$  electron-positron pairs and  $\Gamma_{e^+e^-}^{E0}$  is the rate of formation of  $E0$  pairs for the  $E0$  and  $E2$  transitions de-exciting the Hoyle state as shown in figure 1.1. The proposed accuracy for the measurement of the  $\frac{\Gamma_{e^+e^-}^{E2}}{\Gamma_{e^+e^-}^{E0}}$  ratio is 3%, which will require (amongst other things), accurate knowledge of the detector response at relatively high energies: the combined kinetic energy of the  $E0$  pairs is 6.6 MeV, and the combined kinetic energy of the  $E2$  pairs is 2.2 MeV. The proposed method is to record only those pairs where the electron and positron share the kinetic energy nearly evenly. Thus, the  $E0$  and  $E2$  pairs will be detected at energies near 3.3 MeV and 1.1 MeV, respectively. These two energies are far enough apart to expect that the detector response could be significantly different.

---

### 1.3 The Experimental Challenge: Outline of Present Work

Electron/positron spectroscopy for nuclear structure research poses several experimental challenges, the most imposing of which is the  $\gamma$ -ray background. For this reason, low sensitivity to photon background and high efficiency for electrons are paramount to the success of an electron spectroscopy measurement. The geometry of the electron detector has the dominant influence on its response, and must be manipulated in order to increase the efficiency for electrons relative to photons, and to improve the energy resolution. However, the geometry of a silicon detector cannot be altered once built, so experimental geometry must be optimised in advance. Because analytical equations for radiation interaction are solvable only in the simplest cases [8], Monte Carlo methods have become accepted as the most accurate method for calculating large scale radiation transport. A crucial advantage of Monte Carlo experiments is that the geometry can be altered at will, allowing the effect of the detector geometry to be studied in detail.

It is common for electron detectors to be designed based on rudimentary calculations of electron stopping power and solid angle concerns. However, the approach is superficial, as the detector response depends upon its geometry in a complex way, due to competing effects, such as energy straggling, backscattering, transmission and other effects to be discussed in chapter 2. The physical interactions of radiation with matter, from which these effects originate, are discussed in chapter 3. One goal of this study is to manipulate the Monte Carlo routine PENELOPE [1] to create a calculational system that can yield not only the efficiency as a function of energy, but also lineshapes and the sensitivity of the detector to sources of background. Effectively, for a given input of radiations, the system will give a numerical simulation of the experimental energy spectrum that can be expected in a real measurement. The aim is to develop a tool for the design of future detectors, and to assist in pushing the boundaries of electron detection sensitivity. An important goal is to provide a method of calibration for existing detectors, to “fill in the gaps” where experimental calibration is not available.

PENELOPE, along with GEANT4 [9], GEANT3 [10] and MNCP [11] are the most highly sophisticated radiation transport programs, in terms of both the accuracy of the

physical models used, and the computational efficiency. It should be noted that the very popular GEANT4 was primarily designed for high energies ( $>10$  MeV). The option exists in GEANT4 to choose a “low energy” simulation scheme, which uses exactly the same physical models and input data as PENELOPE. A comparative study of these four code systems found that PENELOPE and GEANT4 agreed quite closely over the entire energy range of interest to the present work (up to 3.5 MeV), but that these two codes differed dramatically from the other two below 100 keV [12].

As well as extensive simulations, two experiments were carried out, one using a radioactive  $^{133}\text{Ba}$  source and the Honey [13] Si(Li) detector, and the other using a  $^{56}\text{Co}$  source and the SEPH-530 detector [14]. The experiments were used for two purposes: first, to determine the effectiveness of the Monte Carlo system, and second, to provide calibration across the range of higher energies needed for the upcoming experiment to determine the radiative width of the Hoyle state in  $^{12}\text{C}$ . A detailed model of the experimental setup of the  $^{133}\text{Ba}$  source measurement was recreated in the PENELOPE simulations, for comparison between simulation and experiment. Further simulations allowed the detector response to be extended to 3.5 MeV, and enabled a critical analysis of the sources of efficiency loss. These studies were combined with the  $^{56}\text{Co}$  source and simulations for calibration of the  $^{12}\text{C}$  measurement.

Experimental data on the scattering of electrons and positrons directly relevant to the present experimental conditions, are scarce. Two relevant studies known to us are: Kulchitsky [15], who studied the scattering of 2.25 MeV electrons by foils of different materials from aluminium to lead; and Hanson [16] who measured the angular distributions of 15.7 MeV incident electrons scattered by thin Be and Au foils.

## 1.4 Recent Progress in Electron Spectroscopy

Reflecting the current importance of electron spectroscopy, there has been extensive work recently. Most of this work has been directed at low energy electron detection - the sub keV to few keV energy region - due to the applications in electron microscopy and radiation therapy. Recently, extensive studies of Auger electron spectra have been carried out. These lie in the low keV region up to  $\approx 50$  keV [17, 18]. There is extensive



---

interest in this area, due to the applications in radiation therapy, where Monte Carlo methods are commonly used for dosimetry evaluations. Monte Carlo methods are well established in electron microscopy and recently have been used for efficiency calibration of Ge detectors for  $\gamma$ -rays [19], and of Si(Li) detectors for X-rays [20]. Monte Carlo simulations of electron transport have been widely used in electron microscopy for the last few decades [21]. Estimating the backscattering probability is the main focus of these studies, and Monte Carlo methods are currently the most reliable and accurate for this purpose [22, 23]. Recently, experimental and Monte Carlo methods were combined to characterise a Si(Li) detector [20]. The approach was similar to the one presented here, using both radioactive sources and Monte Carlo experiments using the GEANT4 [9] code. The studies were aimed at characterisation of a Si(Li) detector for X-rays in the 0 keV - 60 keV energy region. One of the few examples in the literature of electron-positron pair spectrometer characterisation at higher energy (up to 8 MeV), is that of Tur *et al.* [24]. The approach was to use four scintillator detectors to improve the uncertainty on the radiative width of the Hoyle state in  $^{12}\text{C}$ . Comparisons were made between experiment and GEANT4 simulations in the MeV energy range, for continuous electron-positron pair spectra. Final results on the radiative width of the Hoyle state are yet to be published.

For applications to nuclear spectroscopy research, progress has been made using the Recoil-Decay-Tagging (RDT) technique, in combination with the GREAT spectrometer at the University of Jyväskylä [25]. In this technique, the recoils from a nuclear reaction are implanted into a double sided silicon strip detector (DSSSD). Electrons are then detected in surrounding silicon detectors, the signal from the electron detector is added to the corresponding signal in the DSSSD, to give the total energy signal. The silicon detectors surround the DSSSD in a box-like setup, the normal to each detector being perpendicular to the beam direction. The “add-back” results in some worsening of energy resolution. There is also a relatively large “dead layer”, as the electrons are detected at very extreme angles. The detector is designed to observe  $\alpha$ , proton and electron decays. Some resolution on the electron spectrum must be sacrificed therefore, to allow for this versatility. The detector must accommodate  $\alpha$  particles with energies of 5-10 MeV and  $< 1$  MeV electrons. The thickness of the silicon strips cannot be optimised for either particle alone, and must represent a trade-off between the optimal arrangement for both decays. The SACRED conversion electron array, also

at Jyväskylä, uses a solenoid to transport conversion electron decays to a matrix of segmented PIN silicon diodes [26]. An energy resolution of 3-4 keV was reported for a test case of the 320 keV transition in  $^{133}\text{Cs}$ . In other recent work, the use of arrays of multiple mini-orange detectors has been reported, e.g. the ICEBALL [27] array designed for low resolution studies of high energy ( $>200$  keV) electrons. Using  $\gamma$ -ray and conversion-electron spectroscopy a number of rotational bands have been observed in heavy nuclei including:  $^{254}\text{No}$  [2],  $^{252}\text{No}$  [28],  $^{253}\text{No}$  [2],  $^{250}\text{Fm}$  [29],  $^{251}\text{Md}$  and  $^{255}\text{Lr}$  [30].

---

# Experiment

---

## 2.1 Fundamental Concepts in Detector Characterisation

The two key properties measured in electron spectroscopy are energy and intensity. Energy is the easier of the two to measure to useful precision. If the energy is taken as that which corresponds to the centroid of the full energy peak, energy calibration can be achieved by using a radioactive source with clear and well known lines. Generally a linear fit of the known energies to the centroids of two or more peaks will be adequate.

Absolute intensity is challenging to measure; on practical grounds a relative intensity measurement is preferred whenever it can fulfill the experimental aims (such as the proposed  $^{12}\text{C}$  measurement). Even relative efficiency, though, is far from trivial to measure for electron detectors, especially when there is a significant energy gap between the lines measured. A simple linear calibration may be applicable to some experiments, but in general, the efficiency response is non linear, and shows a more complex dependence on energy; the exact nature of this dependence is determined by the physical interactions of radiations with the bulk material of the detector, which are discussed in the next chapter. The separator/transporter, if used, introduces an additional energy dependence to the efficiency.

An added complication in electron spectroscopy is the presence of competing radiations, such as photons. It is often preferable to use a transporter or separator to separate the electrons/positrons from the background radiation (predominantly  $\gamma$ -rays). The  $^{12}\text{C}$  experiment will use a magnetic transporter that transports to the detector only those particles with the correct energy and charge to mass ratio. A series of baffles absorbs other radiations. While this greatly reduces the background, it also reduces the efficiency of the system, due to the angular acceptance of the transporter. The overall efficiency of the

spectrometer  $\eta(E)$ , including the transporter and detector, can be defined as

$$\eta(E) = \frac{A}{N_{emitted}}; \quad (2.1)$$

where  $A$  is the peak area at energy  $E$  recorded in the detector and  $N_{emitted}$  is the number of electrons/positrons emitted from the source with energy  $E$ . The overall efficiency can be written in terms of the two contributions:

$$\eta(E) = T(E) \times \eta_{det}(E) \quad (2.2)$$

where  $T(E)$  is the transmission of the magnetic transporter, and  $\eta_{det}(E)$  is the detector efficiency, defined by

$$\eta_{det}(E) = \frac{A}{N_{incident}}, \quad (2.3)$$

where  $N_{incident}$  is the number of particles that are transported and strike the detector.

The focus of this work is not on the transmission of the magnetic transporter, but rather on the response of the detector as a function of the energy and angle of incident electrons. The efficiency is the primary, but not the only, concern. Also of interest are the lineshapes and energy resolution that can be expected.

## 2.2 Semiconductor Detectors

A number of different types of detectors are used for electron spectroscopy. Here the focus is exclusively on semiconductor detectors. The detector generally consists of a single crystal of a semiconductor such as silicon or germanium, doped with an appropriate impurity. The passage of radiation in a solid-state detector creates electron-hole pairs, which are collected by an applied electric field. There is thus a flow of current and a drop in the voltage across the detector, which gives the observed output pulse. The amplitude of the signal is a measure of the energy of the particle.

As shown in figure 2.1, even energetic electrons completely stop in a few millimeters or less of silicon (a 1 MeV electron has a range of approximately 2.5 mm). Because silicon can be cut into extremely thin wafers, the higher stopping power of electrons relative to

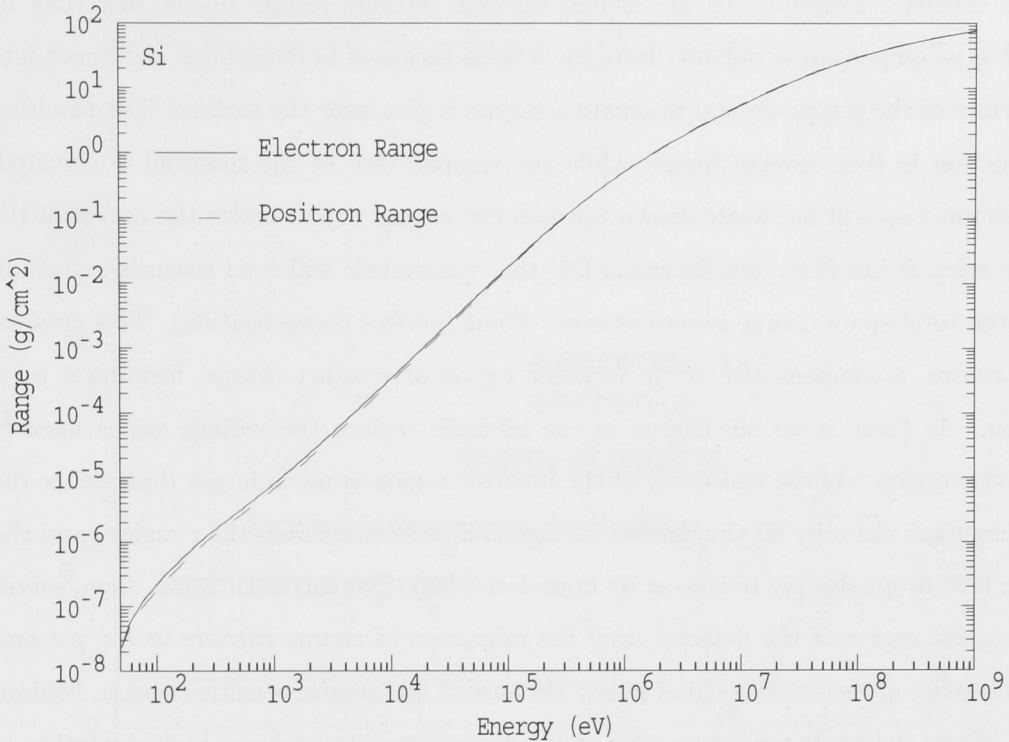


**Figure 2.1:** The range of electrons and positrons in silicon [8].

photons can be exploited. By allowing most photons to pass through without interaction, while ensuring that most electrons are stopped completely, the photon background can be greatly reduced. Solid state detectors have better energy resolution than, say, scintillator detectors because of the low amount of energy required to create an electron-hole ( $E_{pair}$ ) pair, which improves the statistics of the charge collection process (more electron-hole pairs are created for a given radiation). For silicon the energy required to create an electron hole pair is 3.62 eV at 300 K and 3.81 eV at 77 K.  $E_{pair}$  is not the same as the band-gap in silicon, 1.1 eV at room temperature, as most of the deposited energy goes into exciting lattice vibrations. Although,  $E_{pair}$  is a fundamental limitation on the energy resolution. However, as will be seen below, other contributions to the intrinsic energy resolution of the detector are much larger than this.

### 2.2.1 Lithium-Drifted Silicon Diodes - Si(Li)

Lithium-drifted diodes were developed to increase the depletion zone, or the sensitive region of the semiconductor. The maximum thickness that can be achieved using a conventional silicon diode is 1-2 mm; but thicknesses of up to 10 mm can be achieved with

---

lithium drifting. Lithium ions are drifted through initially *p*-type silicon, and may be termed as a compensating dopant. Initially, a large excess of Li donor ions is diffused into one surface of the *p*-type crystal to create a *n*-type region near the surface. The resulting *p-n* junction is then reverse biased while the temperature of the material is elevated. The lithium ions will be slowly drawn towards the *p*-type region under the action of the electric field. It has been demonstrated [31] that the system will tend towards a state in which the total space charge is zero at every point (perfect compensation). This creates, in the centre, a compensated, or an intrinsic region of zero-net charge, forming a *p-i-n* junction. As there is no net charge in the intrinsic region, the voltage varies linearly across this region. As the resistivity of the intrinsic region is much larger than either the *p* or *n* regions, virtually all the applied voltage is distributed across the *i* region, and the electric field drops sharply to zero at its boundaries [32]. The intrinsic region, then, serves as the active region of the detector, and the migration of charge carriers to the *p-i* and *i-n* boundaries gives rise to a signal pulse. Because of the greater sensitive region, lithium drifted silicon detectors must be cooled to low temperatures to achieve high resolution.

## 2.3 Lineshapes

A common challenge of electron spectroscopy is to measure electron radiations with intensities far lower than the competing radiations. For example, the E2 3.2 MeV *E2* pair line in  $^{12}\text{C}$  is 1136 times weaker than the corresponding  $\gamma$ -ray, and  $2.8 \times 10^6$  times weaker than the  $\alpha$ -decay rate. Increasing the efficiency for electron detection will of course improve the peak to background ratio, but the importance of energy resolution should not be overlooked. For example, doubling the energy resolution will double the height of the peak, possibly allowing a peak to be measured that would otherwise be hidden by the background level in the spectrum. As such, energy resolution as well as efficiency are crucial factors in detector design.

Internal conversion produces monoenergetic lines; however, peaks with a definite energy spread and distinctive lineshape are observed, as shown in figure 2.2. The observed experimental lineshapes, can be explained as the sum of various physical phenomena associated with the interactions of radiation with matter and the properties of the semiconductor. The lineshapes of the electron peaks can be attributed to the following effects:

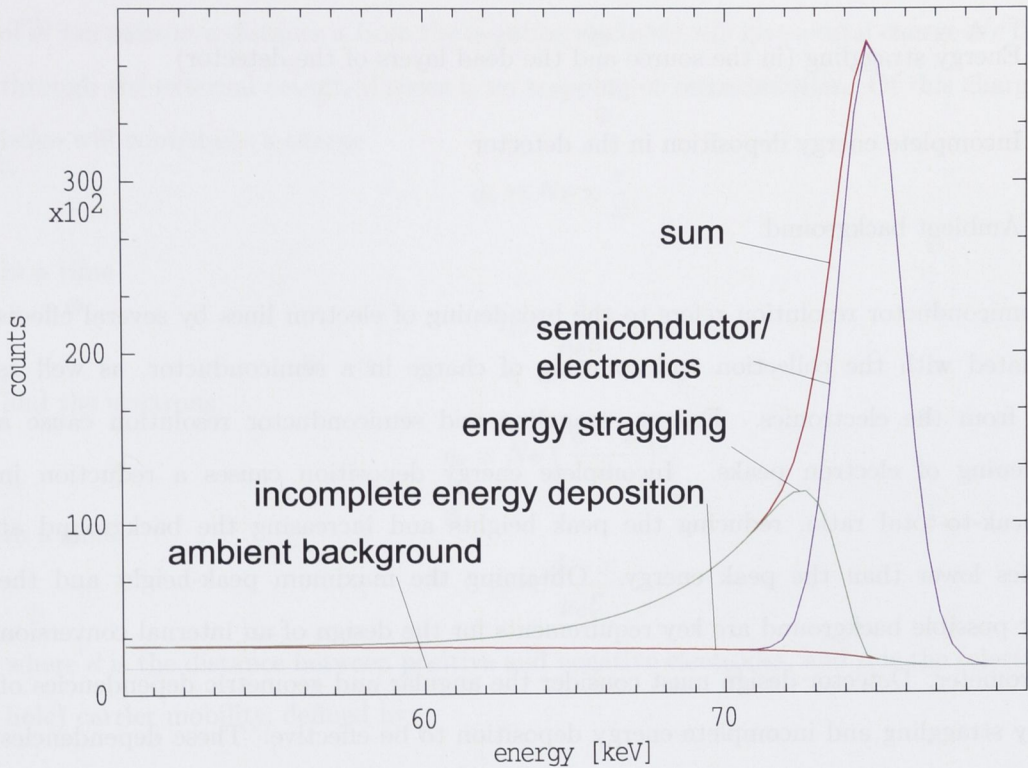


**Figure 2.2:** An example of the contributions to lineshape of a typical conversion-electron peak. The contributions from energy straggling, incomplete energy deposition, electronic noise, semiconductor effects and room background are summed to give the lineshape.

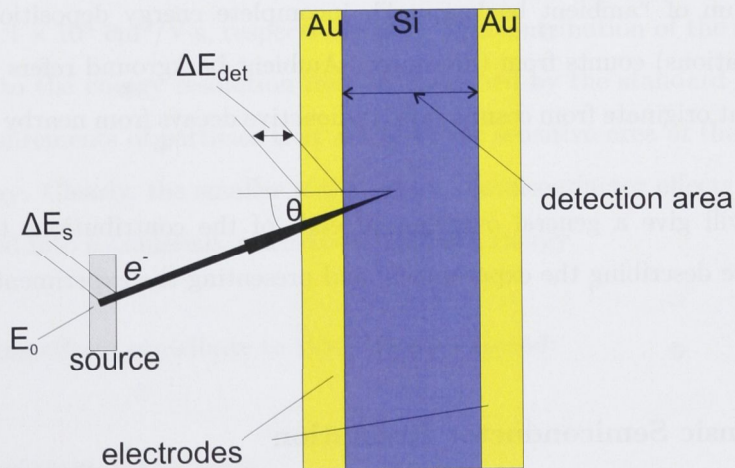


**Figure 2.3:** A schematic of electron detection. An electron, emitted from a nucleus with energy  $E_0$  loses energy in the source ( $\Delta E_s$ ), and in the front electrode ( $\Delta E_{det}$ ) and deposits an energy signal  $E = E_0 - \Delta E_s - \Delta E_{det}$  in the detector.

1. Semiconductor resolution (intrinsic as well as electronics)
2. Energy straggling (in the source and the dead layers of the detector)
3. Incomplete energy deposition in the detector
4. Ambient background

Semiconductor resolution refers to the broadening of electron lines by several effects associated with the collection and counting of charge in a semiconductor, as well as noise from the electronics. Energy straggling and semiconductor resolution cause a broadening of electron peaks. Incomplete energy deposition causes a reduction in the peak-to-total ratio, reducing the peak heights and increasing the background at energies lower than the peak energy. Obtaining the maximum peak-height and the lowest possible background are key requirements for the design of an internal conversion spectrometer. Detector design must consider the angular and geometric dependencies of energy straggling and incomplete energy deposition to be effective. These dependencies are dictated by electron scattering theory (to be discussed in chapter 3). The term “background” is often used fairly loosely to refer to unwanted radiations or counts in the spectrum. From here on, “ambient background” will be used to refer to random decays that do not originate from the source or the target, approximated by a straight line in figure 2.2; whereas “background” will refer to the sum of all unwanted detector counts, the sum of “ambient background”, incomplete energy deposition, and photon (or other radiations) counts from the source. Ambient background refers to mostly photon events, that originate from cosmic rays, radioactive decays from nearby materials, *etc.*

Here we will give a general overview of each of the contributions to the detector response before describing the experiments, and presenting the experimental spectra.

### 2.3.1 Intrinsic Semiconductor Resolution

An ideal detector would be one in which particles of the same incident energy always produced signals of the same amplitude. In practice this is never the case; there is always some spread.



Upon interacting with the detector crystal, an incident radiation that generates a total of  $N$  ion pairs at a distance  $x$  from the negative electrode will give a total charge  $Ne$  flowing through the external circuit, if there is no trapping or recombination. Of this charge, the holes will contribute a charge

$$q_h = Ne \times \frac{x}{d} \quad (2.4)$$

in a time

$$\tau_c = \frac{x}{\mu_h \mathcal{E}} \quad (2.5)$$

and the electrons

$$q_e = Ne \left( \frac{d-x}{d} \right) \quad (2.6)$$

in a time

$$\tau_c = \frac{d-x}{\mu_e \mathcal{E}} \quad (2.7)$$

where  $d$  is the distance between positive and negative electrodes, and  $\mu$  is the (electron or hole) carrier mobility, defined by:

$$v_h = \mu_h \mathcal{E} \quad (2.8)$$

$$v_e = \mu_e \mathcal{E} \quad (2.9)$$

where  $v_e$  and  $v_h$  are the electron and hole drift velocities in an applied electric field of magnitude  $\mathcal{E}$ . The electron and hole mobilities  $\mu_e$  and  $\mu_h$  in silicon at 77 K are  $2.1 \times 10^4$  cm<sup>2</sup>/V·s and  $1.1 \times 10^4$  cm<sup>2</sup>/V·s, respectively [32]. The contribution of the semiconductor detector itself to the energy resolution may be described by the standard deviation  $\sigma$  in the set of measurements of particles that arrive at the sensitive area of the detector with the same energy. Clearly, the smaller  $\sigma$  the better. Semiconductor effects cause the line to be broadened into a Gaussian, centred on the peak energy.

The following effects contribute to this Gaussian spread:

1. *Number of electron-hole pairs*

Perhaps the most fundamental source of intrinsic semiconductor resolution is the distribution in  $N$ , the number of electron-hole pairs created by a given particle of a given energy entering the sensitive region of the detector. Due to the statistical nature of electron scattering, the number of electron-hole pairs created by

radiations of a given energy will not be the same every time. This contributes a roughly Gaussian spread to the lineshape, and is a fundamental property of the semiconductor detection method.

## 2. *Incomplete charge collection*

An electron incident on a semiconductor detector will be stopped almost instantaneously, in most cases between  $10^{-12}$  and  $10^{-11}$  sec. But the electrons and holes created may (depending upon where they are created in the material, and the drift velocity) have longer travel times. As such, some of the electrons and holes created by an incident radiation may not reach the electrodes within the charge collection period  $\tau_c$ , see equations 2.5 and 2.7. Clearly incomplete charge collection can also produce a low-energy skew to the lineshape along with making a contribution to the Gaussian width.

## 3. *Thermal noise*

Thermal noise occurs in any conductor. It arises because the velocity distribution of carriers in a medium at non-zero temperature leads to a fluctuating and non-uniform distribution of these carriers in the medium. This leads to a fluctuating voltage between the ends of the semiconductor, whose average value is zero. There are also some small contributions from the effects of high fields and from the temperature distribution to the thermal noise - a given temperature implies a given *average* energy, however the maximum thermal energy is larger.

## 4. *Current noise*

Applying a bias voltage generates a current through the semiconductor. Current noise, as distinct from charge collection noise, arises due to fluctuations in the current that results from applying this bias voltage rather than the current that arises from incident radiations. This unwanted current is made up of discrete movements of electrons and holes, which may be trapped, recombined or generated thermally within the counter. Any process that disrupts the continuous flow of current is an additional source of noise. It requires a different treatment to charge collection noise.

---

(a) *Generation-Recombination noise*

Generation-Recombination noise may be regarded as the noise that occurs from the breaking up of electron trajectories into stages. The charge carriers that make up the current flow in a semiconductor may suffer recombination or may be generated at some point in the bulk material. Such carriers traverse only part of the distance between the electrodes, and so contribute pulses which are shorter than those that cross the entire medium. Similarly, single carriers that become trapped for varying times and cross the crystal in two or three stages also do not contribute fully to the signal.

(b) *Shot noise*

One source of *current noise* is *shot noise*, the well known quantum effect that results from the quantisation of charge carriers in the medium. The current flows by means of individual electrons and holes and therefore cannot be continuous.

(c) *Excess Noise*

Excess noise refers to the current noise that is not due to shot noise or generation-recombination noise. Although it may be significant, there is little known about the physical causes of it. It depends upon the nature of the surface treatment applied to the semiconductor, and the type of electrodes used, and is probably related to imperfections in the contact on the crystal.

### 2.3.2 Energy Straggling

Energy straggling describes the process whereby an electron loses part of its energy before reaching the sensitive part of the detector. This results in the electron depositing less than its full energy in the sensitive part of the detector, and of course, a lower energy signal is recorded. Energy straggling occurs if there is any material between the radiation source and the sensitive area of the detector. In experiments described below there are contributions from the gold window on the detector and the depth distribution of the source. Straggling arises because the absorption of energy by matter is a statistical process, causing an originally monoenergetic electron line to no longer

be “sharp”. The thicker the material through which the electrons must pass, the greater the straggling, and the lower the energy resolution. A thick target not only broadens the peak but shifts it to a lower energy and worsens the lineshape (giving it an extra “tail”). This hampers conversion-electron spectrometry, making determination of intensities and energies less accurate, and decreasing the ease with which nearby lines can be resolved. In conversion-electron spectrometry, at energies in the range of hundreds of keV, with very thin targets ( $\leq 1 \text{ mg cm}^{-2}$ ), a reasonable rule of thumb is that an addition of  $1 \text{ mg cm}^{-2}$  to the target thickness worsens the resolution by 1 keV [33, p136].

The energy straggling increases as the solid angle subtended by the detector increases, simply because geometry then allows a bigger range of path lengths through the source and detector dead region. Electrons that hit the edges of the detector will travel through more target material than those that hit near the centre, making them likely to lose more of their energy in the target and therefore contribute less than their starting energy in the detector (see figure 2.3). This poses a conflict with the desire to increase the efficiency, which clearly increases with solid angle. A large range of incident angles also causes a longer low energy “tail”, to the left of the electron peak. The lineshape caused by energy straggling is affected by the detector geometry, but also depends upon the material, in which the energy loss occurs. In the  $^{12}\text{C}$  measurement, there are expected to be two materials that will cause energy straggling, the gold window on the detector and the carbon target foil (see figure 2.3). The straggling in the latter will depend heavily upon the solid angle and the implantation depth.

### 2.3.3 Incomplete Energy Deposition

Of crucial importance to the planned electron spectroscopy measurements on  $^{12}\text{C}$  is the efficiency as a function of energy and angle. The proposed methods involve taking ratios of measurements, meaning it is not necessary to determine the *absolute efficiency* of the device. The solid angle efficiency will cancel upon taking the ratio, and the measurements can be corrected for the transmission of the Lens transporter, the energy dependence of which is known accurately. The quantity of interest is the detector efficiency  $\eta_{det}$  of equation 2.3. If all the particles that hit the detector deposit their full energy in the detector, the detector efficiency  $\eta_{det}$  will be 100%. Traditionally, deviations from 100%

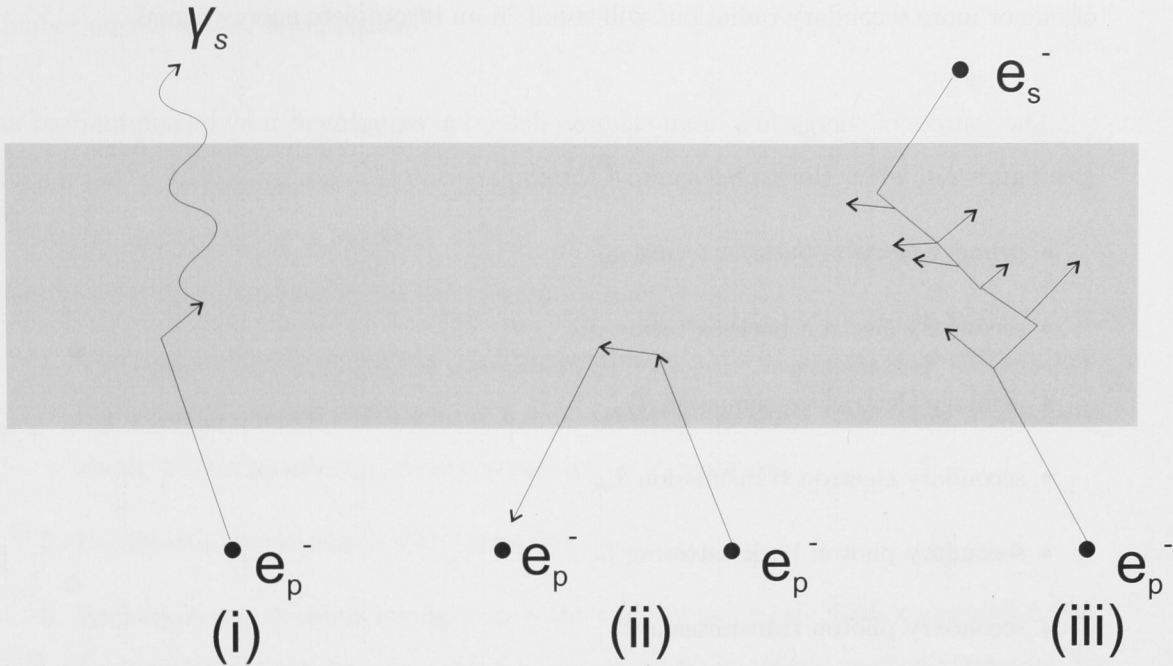


**Figure 2.4:** Incomplete energy deposition: (i) Secondary photon transmission ( $T_\gamma$ ): a primary electron ( $e_p^-$ ) interacts with the detector material and produces a secondary photon,  $\gamma_s$ , which is transmitted (ii) Primary electron backscattering ( $\rho_{pb}$ ): a primary electron interacts with the detector material and is backscattered (iii) Secondary electron transmission ( $T_{se}$ ): a primary electron suffers interactions and produces a number of secondary electrons  $e_s^-$ , one of which is transmitted.

have been attributed to backscattering, the ejection of the primary particle from the detector with a negative velocity (if the initial direction is defined as positive) see figure 2.4. However, this treatment neglects several sources of efficiency loss that can be equally or even more important.

Several different effects can be responsible for incomplete energy deposition. The most obvious is when the incident (primary) particle leaves the detector with some non-zero energy. It may pass through the entire detector and exit at the back (transmission) or be reflected out the front of the detector (backscattering). In general, upon interacting with the detector material, the incident particle will create a multitude of secondary electrons and photons from ionisation events and excitation-relaxation events. For example, a 3 MeV electron can be expected to create somewhere in the order of  $10^{15}$  secondary radiations. The incident energy  $E$ , will then be shared among these “secondary” radiations. The entire family, consisting of a primary and its secondary radiations, may be called a “shower”. In order for a complete energy signal to be recorded, the secondary radiations must also be stopped fully in the detector; any transmission or backscattering

of one or more secondary radiations will result in an incomplete energy signal.

The sources of energy loss in an electron detection experiment may be summarised as (see figure 2.4, which illustrates some of these):

- primary electron backscattering  $\rho_{pb}$
- secondary electron backscattering  $\rho_{sb}$
- primary electron transmission  $T_{pe}$
- secondary electron transmission  $T_{se}$
- secondary photon backscattering  $\rho_{\gamma}$
- secondary photon transmission  $T_{\gamma}$

As already noted, all secondary radiations must be fully absorbed in order for the full energy signal to be recorded. The detector efficiency will be 100% less the probability of incomplete energy deposition,  $\chi$ :

$$\eta_{det} = 1 - \chi. \quad (2.10)$$

Alternatively, rewriting in terms of the specific contributions to the incomplete energy depositions  $\chi$ :

$$\eta_{det} = 1 - \rho_{pb} - \rho_{sb} - T_{pe} - T_{se} - \rho_{\gamma} - T_{\gamma}. \quad (2.11)$$

The focus of the literature on primary backscattering is probably due to the fact that electron spectroscopy has been predominantly conducted at low energies (*i.e.*  $< 500$  keV), where primary backscattering is indeed dominant. As bremsstrahlung radiation becomes the dominant form of energy loss in silicon for electrons above 1 MeV, minimising the photon transmission becomes crucial for studies of electrons and positrons above a few hundred keV in energy.

Incomplete energy deposition events can deposit any energy  $E$  between 0 and  $E_{inc}$ , where  $E_{inc}$  is the energy of the particle upon entering the detector. Most of these events will not be recorded as part of the peak, as they can take any energy in the range  $0 \leq E \leq E_{inc}$ . In fact it is common to approximate the contribution of incomplete energy signals to the spectrum by a step function (see figure 2.2). As well as reducing efficiency, these events will also have an effect on the lineshape, effectively making the background

higher on the side of lower energy.

In the low energy region, where primary backscattering is dominant, the backscattering coefficient  $\rho$ , defined as the number of backscattered electrons divided by the number of electrons impinging on a material surface, is an important quantity. Some important results relating to backscattering may be summarised as follows:

1. The backscattering coefficient  $\rho$  increases strongly with increasing  $Z$  of the medium. For example backscattering of 100 keV incident electrons from carbon produces about 4% backscattering events, whereas it is 50% for gold.
2. Backscattering decreases with increasing energy.
3. Backscattering depends strongly upon the angle of incidence. Geometry implies that backscattering will increase with any departure from normal incidence because, in effect, the trajectory of the electron remains nearer the front surface of the detector. For example, a  $60^\circ$  angle of incidence typically produces about twice as many backscattered electrons as normal incidence. Since energy straggling also increases as the angle departs from normal incidence, a key point of detector design is to minimise the departures from normal incidence for which radiation strikes the detector.

## 2.4 Experimental Measurements

In order to study the efficiency and lineshape response of silicon detectors, and to provide a reference for simulations, radioactive source experiments were made, with a  $^{133}\text{Ba}$  source and a  $^{56}\text{Co}$  source. The  $^{133}\text{Ba}$  measurement was designed to calibrate the detector at low energy (20 keV - 400 keV) and the  $^{56}\text{Co}$  measurement was designed to calibrate the detector in the MeV range (up to 3.5 MeV). The decays from the 7.654 MeV Hoyle state to the ground state will be detected at roughly 3.3 MeV, as the experimental method proposed measures those pairs that share the energy roughly equally. These results are crucial for the following purposes:

1. Characterisation of existing Si(Li) detectors
2. Design of future electron detectors
3. Detector calibration in anticipation of an upcoming measurement of the decay rate of the Hoyle state in  $^{12}\text{C}$

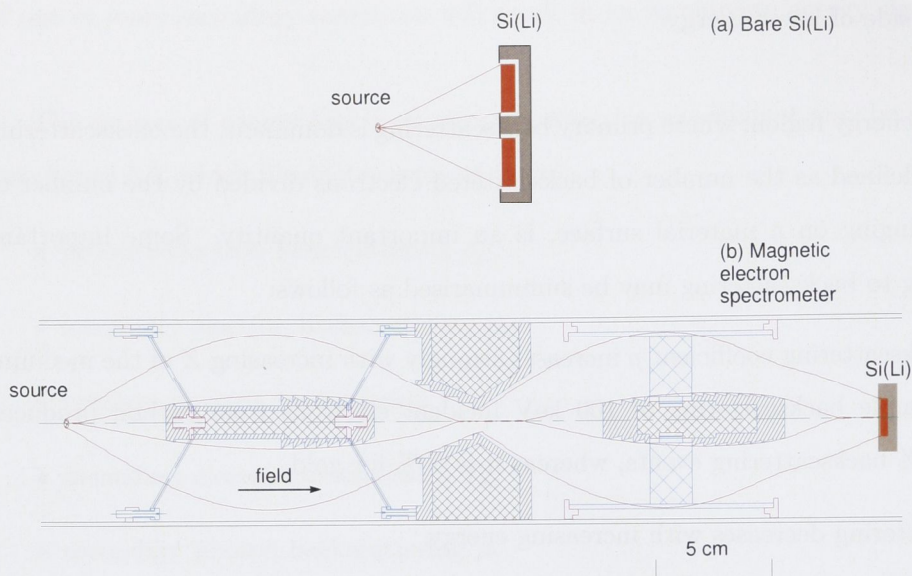


**Figure 2.5:** Cross sectional view of the experimental setups used for the  $^{133}\text{Ba}$  radioactive source measurements. Red lines indicate the envelope of the spectrometer acceptance. (a) Honey electron array to obtain the mixed photon and conversion-electron data. (b) Magnetic spectrometer used to obtain the electron spectrum.

Two experimental setups were used as shown in fig 2.5: (a) a bare Si(Li) detector in front of a radioactive source; and (b) a radioactive source, magnetic transporter and Si(Li) detector. Setups (a) and (b) can accommodate either of two Si(Li) detectors, the Honey [34] detector array or the SEPH-530 [14] detector. For these measurements, Honey was in (a) and SEPH-530 in (b). The  $^{133}\text{Ba}$  measurement used the Honey detector and setup (a). The  $^{56}\text{Co}$  measurement used setup (b) with the SEPH-530 detector.

## 2.5 Experimental Apparatus

### 2.5.1 Further Details of Setup (a) From Figure 2.5

Setup (a) shows the Honey detector, a bare Si(Li) detector, in front of a radioactive source. In this case, there is no material between the detection area of the crystal and the decaying nuclei (except the source material itself, and the electrode on the Si(Li) detector). The angles of acceptance are given by trigonometry. This setup avoids any efficiency loss from a transporter, but it also means that the detector will be sensitive to all source emissions and ambient background. For example, if a conversion-electron emitter is used, the detector will be sensitive to  $\gamma$ -rays, X-rays, Auger electrons, internal conversion-electrons, as well



electrons and positrons, if emitted.

### 2.5.2 Further Details of Setup (b) From Figure 2.5

Setup (b) shows the combined magnetic electron spectrometer and Si(Li) detector, which is sensitive to electrons and positrons only. A solenoidal magnetic field is applied, which causes the electrons and positrons to travel in a helical path. The radius of curvature ( $\rho$ ) is obtained by the magnetic rigidity, which, assuming a (nearly) homogeneous field (the momentum resolution  $\Delta p/p$  is 12% [35]) is given by (in units of Tm) [35]:

$$B\rho = \frac{1.704433 \times 10^{-3} \sqrt{E^2 + 2m_0c^2E}}{m_0c^2}, \quad (2.12)$$

where  $B\rho$  is the magnetic rigidity for electrons and  $m_0c^2$  is the electron rest mass energy, and  $E$  is the electron's kinetic energy, in keV. Only those electrons whose magnetic rigidity falls within a narrow region will be transported (for a given applied magnetic field). The selected particles traverse two loops before detection. There is no straight line view from the source to the detector, so the photon emissions interact with either the axial absorbers or diaphragm. The power supply is operated remotely by a computer, controlling a digital to analog converter (DAC). The field can either be fixed at a value calculated for a specific conversion line or electron-positron pair, or swept, to measure a wide energy range. The computer steps the output voltage of the DAC based on a timer, or after a certain beam charge. For radioactive source measurements timer based control is used. The field is incremented in small steps, typically  $\approx 3$  mA and  $\approx 0.0002$  T in current and field, respectively. Once the field has swept up to the maximum value, it is ramped back down to the initial value, stepping by the same process (making 1 cycle). There is some lag between the magnetic field and the control voltage caused by the impedance of the solenoid, however this has been measured to be less than 1% of the step-time at the sweeping speeds used [35].

### 2.5.3 Honey

The Honey detector array consists of a six-segmented Si(Li) array. Each individual detector is a 4.3 mm thick equilateral triangle, 285.6 mm<sup>2</sup> in area. The front and cross-sectional views are shown in figure 2.6 (and in figures 4.1 and 4.2). The detectors are housed in a copper cylinder. To reduce leakage current and thermal noise, the detector array is cooled to liquid nitrogen temperatures, through a copper conductor. Honey has

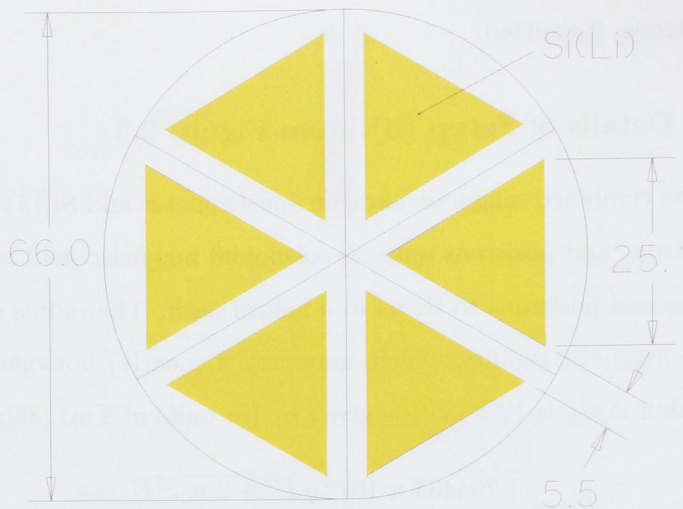


**Figure 2.6:** The front dimensions of the Honey detector.

a 200 Å thick gold electrode on the front and back, and is operated with a reverse bias voltage, which is limited to a maximum of 1000 V. The best energy resolution of about 2 keV full-width at half-maximum (FWHM) comes at low energies ( $\approx 300$  keV), where semiconductor effects (leakage current, thermal noise, etc.) have less impact.

#### 2.5.4 SEPH-530

The SEPH-530 detector is a single, cylindrical Si(Li) detector, 9 mm in thickness, and 19.8 mm in diameter. Like the Honey array, it has a 200 Å thick gold entry window, and is operated with a reverse bias voltage, limited to a maximum of 1000 V.

## 2.6 $^{133}\text{Ba}$ Source Experiment

Table 2.1: Conversion-electron, Auger, X-ray and  $\gamma$ -ray energies and intensities of the  $^{133}\text{Ba}$  radioactive source.

$E_{\gamma}^{(a)}$ [keV]	Multi- <sup>(b)</sup> polarity	Mixing <sup>(b)</sup> Ratio	Line	$E^{(a),(c)}$ [keV]	$I^{(d)}$
			Auger L	2.5 - 5.6	138.0
			Auger KLL	24.41 - 25.80	9.3 (4)
			Auger KLX	29.00 - 30.96	4.39 (19)
			Auger KXY	33.51 - 35.95	0.517 (21)

Table 2.1: continued

$E_\gamma^{(a)}$ [keV]	Multi- <sup>(b)</sup> polarity	Mixing <sup>(b)</sup> Ratio	Line	$E^{(a),(c)}$ [keV]	$I^{(d)}$
			XL	3.8 - 5.7	16.0 (8)
			XK $\alpha_2$	30.625	34.0 (4)
			XK $\alpha_1$	30.973	62.8 (7)
			XK $\beta_3$	34.92	6.17 (19)
			XK $\beta_1$	34.987	11.9 (3)
			XK $\beta_5$	35.259	0.127 (6)
			XK $\beta_2$	35.818	4.03 (16)
			XK $\beta_4$	35.907	0.032 (15)
			XKO $_{2,3}$	35.972	0.53 (6)
53.1622(6)	M1+E2	-0.15 (+6-5)	$\gamma$		2.14 (3)
			K	17.18	10.30 (21)
			L	47.61	1.8 (3)
			M+	52.20	0.46 (9)
79.6142(12)	M1+E2	0.124 (15)	$\gamma$		2.65 (5)
			K	43.63	3.96 (9)
			L	73.98	0.575 (19)
			M+	78.62	0.147 (5)
80.9979(11)	M1+E2	-0.151 (2)	$\gamma$		32.9 (3)
			K	45.01	47.0 (7)
			L	75.38	7.04 (9)
			M+	80.01	1.803 (24)
160.6121(16)	M1+E2	0.96 (5)	$\gamma$		0.638 (4)
			K	124.63	0.149 (3)
			L	155.14	0.0300 (9)
			M+	159.67	0.00780 (20)
223.2368(13)	M1+E2	-0.114 (14)	$\gamma$		0.453 (3)
			K	187.25	0.0379 (6)
			L	217.56	0.00500 (8)
			M+	222.23	0.001271 (20)
276.3989(12)	E2		$\gamma$		7.16 (5)
			K	240.41	0.330 (6)
			L	270.90	0.0603 (10)
			M+	275.44	0.0156 (3)
302.8508(5)	M1+E2	0.022 (20)	$\gamma$		18.34 (13)
			K	266.87	0.684 (12)

Table 2.1: continued

$E_{\gamma}^{(a)}$ [keV]	Multi- <sup>(b)</sup> polarity	Mixing <sup>(b)</sup> Ratio	Line	$E^{(a),(c)}$ [keV]	$I^{(d)}$
356.0129(7)	E2		L	297.16	0.0887 (14)
			M+	301.84	0.0225 (3)
			$\gamma$		62.05 (19)
			K	320.03	1.309 (19)
			L	350.47	0.215 (4)
383.8485(12)	E2		M+	355.04	0.0553 (7)
			$\gamma$		8.94 (6)
			K	347.86	0.151 (21)
			L	378.29	0.0241 (4)
			M+	382.88	0.00619 (8)

(a) Taken from [38]

(b) Taken from [39]

(c) Energy of conversion-electron, Auger-electron, or X-ray

(d) Conversion electron, Auger-electron,  $\gamma$ -ray or X-ray intensity per 100  $^{133}\text{Cs}$  decays

The nucleus  $^{133}\text{Ba}$  decays to excited states in  $^{133}\text{Cs}$  via electron capture with a half-life of 10.540(6) years [38]. The excited nucleus  $^{133}\text{Cs}$  then decays to its ground state via a number of converted electromagnetic transitions, with the conversion-electron energy ranging from 17.18 keV up to 382.88 keV. The energies, intensities and multiplicities of these transitions are well known [38, 39].

The complete spectrum of radiations emitted in the electron capture decay of  $^{133}\text{Ba}$  is listed in table 2.1. The intensities and energies of the  $\gamma$  emissions from  $^{133}\text{Cs}$  were obtained from the ‘‘Decay Data Evaluation Project’’ (DDEP) [38] and the mixing ratios and multiplicities were taken from the ‘‘Evaluated Nuclear Structure Data File’’ (ENSDF) [39]. These parameters were input into the ‘‘Band-Raman Internal Conversion Coefficients’’ code (BrIcc) [40] to obtain the internal conversion coefficients and energies for each shell. The M+ line corresponds to the weighted average energy and summed intensity of the M,N,O,P lines, which are too close in energy to be resolved in most silicon detectors. Similarly, the energies of the conversion-electrons for the L-shell have been evaluated from

the partial values as:

$$I = \sum_i I_i, \quad (2.13)$$

$$E = \frac{\sum_i E_i I_i}{I}. \quad (2.14)$$

The Auger emissions were taken from the DDEP [38]. The X-Ray intensities were calculated by combining data from the DDEP [38] and the Table of Radioactive Isotopes [41]. In summary, for every 100 decays,  $^{133}\text{Ba}$  emits: 152.2 Auger electrons; 78.4 conversion-electrons; 135.6 X-rays and 135.23  $\gamma$ -ray photons.

### 2.6.1 Source Preparation

The source was prepared by dropping a hydrochloric acid solution of  $^{133}\text{Ba}$  on to a  $2.4 \times 10^2 \mu\text{g}/\text{cm}^2$  Mylar foil, depositing a cylindrical distribution of barium chloride. The specific activity,  $3.7 \times 10^5 \text{ Bq}/\text{g}$  and activity,  $7.4 \times 10^4 \text{ Bq}$ , were specified by the supplier [14]. The diameter was measured at 4 mm. The source thickness was determined as follows:

$$\begin{aligned} \frac{\text{Activity}}{\text{Specific activity}} &= \text{mass} \\ \frac{7.4 \times 10^4 \text{ Bq}}{3.7 \times 10^5 \text{ Bq}/\text{g}} &= 2 \times 10^{-7} \text{ g} \\ \rho &= 3.586 \text{ g}/\text{cm}^3 \\ \text{Area} = \pi(0.2 \text{ cm})^2 &= 0.126 \text{ cm}^2 \\ t &= \frac{2 \times 10^{-7} \text{ g}}{0.126 \text{ cm}^2 \times 3.586 \text{ g}/\text{cm}^3} \\ &= 4.4 \text{ nm}, \end{aligned} \quad (2.15)$$

or  $1.59 \mu\text{g}/\text{cm}^2$ . A thin gold layer was evaporated onto the Mylar to prevent the build up of electrostatic charge. The source, with the Mylar foil, was housed within a square 19 mm  $\times$  19 mm aluminium frame of thickness 0.5 mm. Electrons (and positrons) emitted from within the source can lose part of their energy traversing the source material. This will have an effect on the lineshape observed, causing broadening and asymmetry in the peaks, due to energy straggling. For example, a 100 keV electron will lose an average of 0.1 keV on traversing the source material and the gold window of the detector [42].

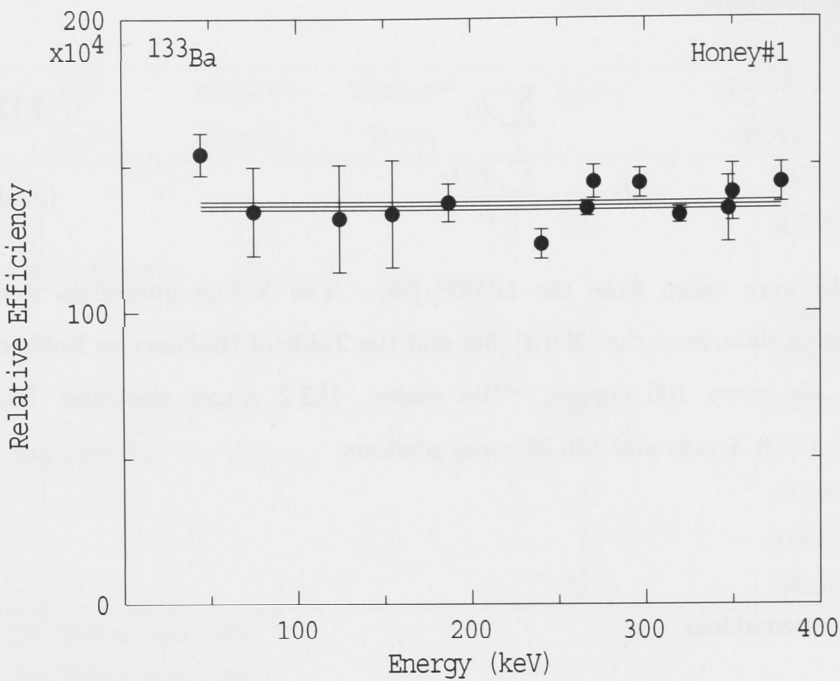


**Figure 2.7:** The efficiency as a function of energy for the Honey detector.

### 2.6.2 Data Collection

Two sets of measurements were taken on the  $^{133}\text{Ba}$  source, using:

- (a) No magnetic transporter, and the Honey detector array
- (b) The magnetic transporter and the SEPH-530 detector

The efficiencies of both setups were determined experimentally by comparing the peak areas of the conversion-electron peaks to the intensities given in table 2.1. The efficiency of the bare Honey detector was found to be constant with energy (see figure 2.7). The efficiency of the magnetic spectrometer and SEPH-530 detector data shows a more complex dependence, see figure 2.8, due to the transmission of the magnetic transporter. The solid line is the fit to the data obtained by integrating the momentum window over the energy region [43], and applying a scaling factor.

The Honey data were recorded over 23 hours. The SEPH-530 data were taken over 17 hours, the magnetic field was swept over 77 cycles. Figure 2.8 shows the transport efficiency of the Lens magnetic transporter. To correct for the energy dependent efficiency of the transporter the raw data were divided by the efficiency of the Lens transporter. The two spectra were normalised to each other using the 356 K line. By fitting the

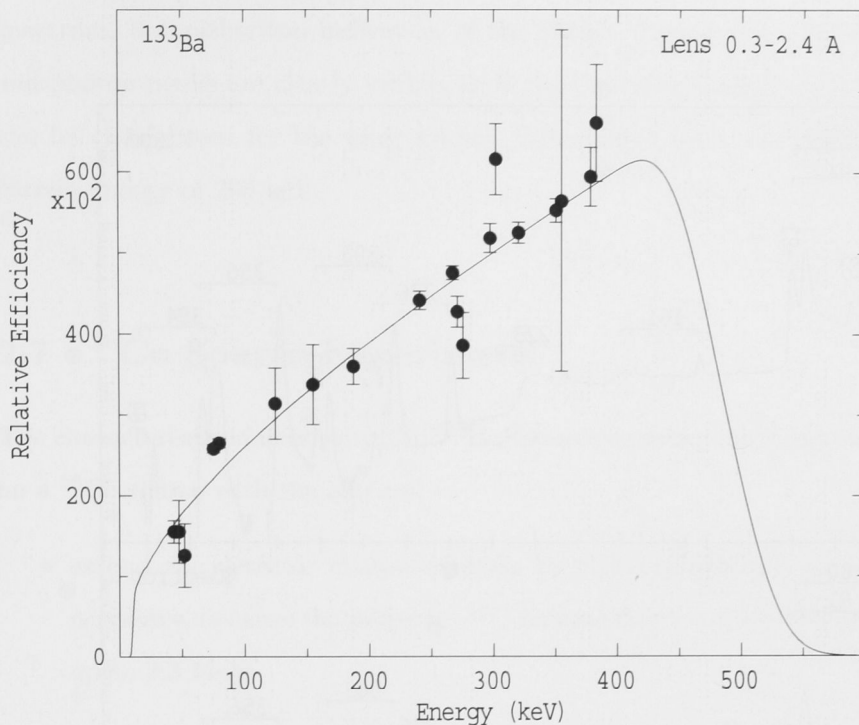


**Figure 2.8:** The efficiency of the magnetic spectrometer and SEPH-530 detector. Points: experimental efficiencies from the  $^{133}\text{Ba}$  source experiment; Solid curve: Transport efficiency, calculated by integrating the momentum window over the current range and normalising to the experimental data.

experimental spectra, the peak positions were obtained accurately, and the SEPH-530 data were shifted in energy to line up with the Honey data. The data were then energy calibrated by comparing the electron peak positions in the Honey data to table 2.1 and applying a linear calibration. An ambient background spectrum was recorded in the Honey chamber (with no source present) for 25 hours, this was subtracted from both the Honey data and the Lens data (but not the difference spectrum). The efficiency corrected and energy calibrated experimental energy spectra of the  $^{133}\text{Ba}$  source are shown in figure 2.9. The top panel is the bare Si(Li), Honey detector data (a), the middle is the magnetic spectrometer, SEPH-530 detector data (b), and the bottom panel is the difference between the Honey and Lens ((a) - (b)).

The difference spectrum is dominated by photon events in the Honey detector. Some discontinuities around the peaks, and some negative values occurred. Some irregularities must be expected due to the differing detector geometries, amplifiers, angles of incidence and also statistical fluctuations. The difference spectrum then is not the exact photon

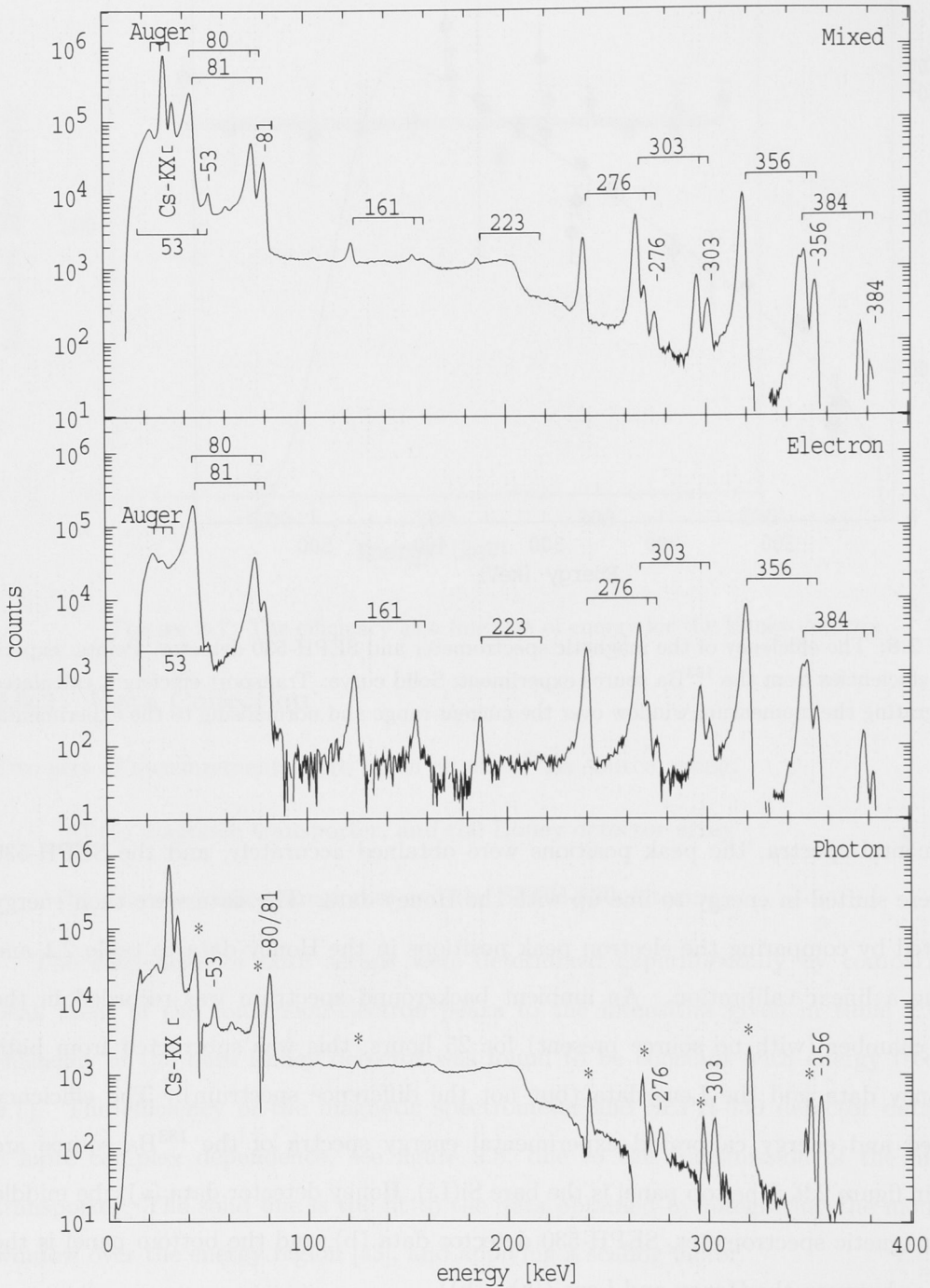


**Figure 2.9:**  $^{133}\text{Ba}$  energy spectra. Top panel: Mixed photon and electron spectrum, measured with Honey; Middle panel: Electron spectrum, measured with the SEPH-530, combined with the Lens spectrometer; Bottom panel: Pure photon spectrum deduced by subtracting the middle panel from the top panel; the features labeled \* are artifacts of the subtraction.



spectrum, but rather, an indication of the photon background. Nevertheless, the X-ray and photon peaks are clearly visible, as is the Compton background. The Compton edge can be clearly seen for the most intense high energy peak, the 356 keV, at exactly the correct energy of 203 keV.

## 2.7 $^{56}\text{Co}$ Source Experiment

The characterisation done with the  $^{133}\text{Ba}$  measurement was extended with a measurement on a  $^{56}\text{Co}$  source with the aim to:

- extend the detector characterisation to high energies (up to 3.4 MeV). This was necessary, because the proposed  $^{12}\text{C}$  measurement requires detector characterisation up to 3.3 MeV.
- demonstrate the ability of the spectrometer to detect high energy electron-positron pairs.

$^{56}\text{Co}$  was chosen because it is a high energy internal conversion-electron and electron-positron pair emitter exhibiting converted transitions up to 3.4 MeV (table 2.2). The experiment was conducted with the magnetic electron transporter and the SEPH-530 detector.

Table 2.2: Conversion-electrons, photons and pairs, emitted from  $^{56}\text{Fe}$  with an intensity exceeding  $1 \times 10^{-5}$  particles per 100 disintegrations of  $^{56}\text{Co}$ .

$E_{\gamma}^a$ [keV]	Multi- <sup>b</sup> polarity	Mixing <sup>b</sup> Ratio	Line	$E^{a,c}$ [keV]	$I^d$
733.5085(23)	M1+E2	-0.02(2)	$\gamma$	0.191(4)	
			K	726.40	5.08(14)E-5
787.7391(23)	M1+E2	0.85(35)	$\gamma$	0.310(4)	
			K	780.63	8.9(7)E-5
846.7638(19)	E2		$\gamma$	99.9399(23)	
			K	839.65	2.67(4)E-2
			L	845.99	2.55(4)E-3

Table 2.2: continued

$E_{\gamma}^a$ [keV]	Multi- <sup>b</sup> polarity	Mixing <sup>b</sup> Ratio	Line	$E^{a,c}$ [keV]	$I^d$
			M+	846.68	3.68(5)E-4
977.363(4)	M1+E2	0.07(3)	$\gamma$		1.422(7)
			K	970.25	2.10(3)E-4
			L	976.59	2.00(3)E-5
996.939(5)	M1+E2	1(Assumed)	$\gamma$		0.116(6)
			K	989.83	1.9(3)E-5
1037.8333(24)	M1+E2	0.00(5)	$\gamma$		14.03(5)
			K	1030.72	1.84(3)E-3
			L	1037.06	1.75(3)E-4
			M+	1037.75	2.52(3)E-5
1175.0878(22)	M1+E2	0.14(4)	$\gamma$		2.249(9)
			K	1167.97	2.32(6)E-4
			L	1174.32	2.21(3)E-5
1238.2736(22)	E2		$\gamma$		66.41(16)
			K	1231.16	7.16(10)E-3
			L	1237.50	6.8(1)E-4
			M+	1238.19	9.81(13)E-5
			Pair		1.027(24)E-3
1360.196(4)	M1+E2	-0.11(1)	$\gamma$		4.280(13)
			K	1353.08	3.34(5)E-4
			L	1359.43	3.168(5)E-5
			Pair		1.361(22)E-4
1771.327(3)	M1+E2	-0.004(2)	$\gamma$		15.45(4)
			K	1764.21	7.44(11)E-4
			L	1770.56	7.04(10)E-5
			M+	1771.24	1.015(14)E-5
			Pair		2.48(3)E-3
1810.726(4)	M1+E2	-0.17(3)	$\gamma$		0.639(3)
			K	1803.61	2.97(4)E-5
			Pair		1.131(20)E-4
1963.703(11)	M1+E2	-0.02(2)	$\gamma$		0.706(4)
			K	1956.59	2.84(4)E-5
			Pair		1.68(3)E-4
2015.176(5)	M1+E2	0.68(5)	$\gamma$		3.017(14)
			K	2008.06	1.181(18)E-4

Table 2.2: continued

$E_\gamma^a$ [keV]	Multi- <sup>b</sup> polarity	Mixing <sup>b</sup> Ratio	Line	$E^{a,c}$ [keV]	$I^d$
2034.752(5)	M1+E2	-0.073(5)	L	2014.41	1.117(17)E-5
			Pair		8.42(15)E-4
			$\gamma$		7.741(13)
2113.092(6)	M1+E2	0.27(3)	K	2027.64	2.93(4)E-4
			L	2033.98	2.77(4)E-5
			Pair		2.08(3)E-3
2212.898(3)	M1+E2	-3(1)	$\gamma$		0.376(3)
			K	2105.98	1.336(22)E-5
			Pair		1.154(21)E-4
2276.16(16)	E2		$\gamma$		0.385(5)
			K	2205.79	1.32(3)E-5
			Pair		1.58(4)E-4
2523.0(8)	E2		$\gamma$		0.118(4)
			Pair		5.29(20)E-5
			$\gamma$		0.063(8)
2598.438(4)	M1+E2	-0.28(2)	Pair		3.1(4)E-5
			$\gamma$		16.96(4)
			K	2591.43	4.264(11)E-4
2657.5(8)	E2		L	2597.67	4.03(6)E-5
			Pair		8.80(14)E-3
			$\gamma$		0.0195(20)
3009.559(4)	M1+E2	0.065(5)	Pair		1.23(13)E-5
			$\gamma$		1.038(19)
			K	3002.45	2.05(5)E-5
3201.930(11)	M1+E2	0.50(1)	Pair		7.10(16)E-4
			$\gamma$		3.203(13)
			K	3194.82	5.79(8)E-5
3253.402(5)	E2		Pair		2.50(4)E-3
			$\gamma$		7.87(3)
			K	3246.29	1.424(21)E-4
3272.978(6)	M1+E2	0.420(4)	L	3252.63	1.345(19)E-5
			Pair		7.00(11)E-4
			$\gamma$		1.855(9)
			K	3265.87	3.24(5)E-5
			Pair		1.493(23)E-5

Table 2.2: continued

$E_{\gamma}^a$ [keV]	Multi- <sup>b</sup> polarity	Mixing <sup>b</sup> Ratio	Line	$E^{a,c}$ [keV]	$I^d$
3369.7(3)	E2		$\gamma$		0.0103(8)
3451.119(4)	E2		$\gamma$		0.942(6)
			K	3444.01	1.56(2)E-5
			Pair		9.12(14)E-4
3547.93(6)	M1+E2	-0.30(2)	$\gamma$		0.1956(13)
3611.8(8)	E2		$\gamma$		0.0084(4)

<sup>a</sup> Taken from [44]

<sup>b</sup> Taken from [37]

<sup>c</sup> Energy of conversion-electron, Auger electron, or X-ray

<sup>d</sup> conversion-electron, Auger electron,  $\gamma$ -ray or X-ray intensity per 100 <sup>56</sup>Co decays

Table 2.2 shows the  $\gamma$ , pair and conversion-electron emissions from <sup>56</sup>Co. The intensities and energies of the  $\gamma$  emissions were again evaluated from DDEP [44] and the mixing ratios and multipolarities were taken from ENSDF [37]. These parameters were input to BrIcc [40] to obtain the internal conversion and pair coefficients and energies for each shell.

### 2.7.1 Source Preparation

The source was made in the ANU laboratories. The source was calibrated by comparison to a <sup>152</sup>Eu source of known activity. The <sup>152</sup>Eu source was counted in the same experimental setup, and the 344 keV  $\gamma$ -ray was chosen for comparison. The count-rate ( $\Pi_{344\gamma}$ ) is given by:

$$\Pi_{344\gamma} = J_{344\gamma} \times \eta_{344\gamma} \times A_{344\gamma} \quad (2.16)$$

where  $A_{344\gamma}$  is the source activity, in Becquerels,  $\eta_{344\gamma}$  is the absolute efficiency of the  $\gamma$ -detector and  $J_{344\gamma}$  is the intensity of the 344 keV line. Rearranging equation 2.16 yields

$$\begin{aligned} \eta_{344\gamma} &= \frac{\Pi_{344\gamma}}{J_{344\gamma} \times A_{344\gamma}} \\ \eta_{344\gamma} &= \frac{6.1 \text{ Bq}}{0.2765 \times (1.41 \times 10^5) \text{ Bq}} \\ \eta_{344\gamma} &= 1.56 \times 10^{-4}. \end{aligned} \quad (2.17)$$

In-house studies show that the  $\gamma$ -ray detector used has twice the absolute efficiency at

344 keV as at 840 keV, which means that the absolute efficiency at the 846  $\gamma$ -line of  $^{56}\text{Co}$  is

$$\eta_{846\gamma} = \frac{1.56 \times 10^{-4}}{2}$$

$$\eta_{846\gamma} = 7.82 \times 10^{-5}$$

Rearranging equation 2.16 gives

$$A_{846\gamma} = \frac{\Pi_{846\gamma}}{J_{846\gamma} \times \eta_{846\gamma}}$$

$$A_{846\gamma} = 4.70 \times 10^4 \text{ Bq}, \tag{2.18}$$

*i.e.* an activity of  $4.70 \times 10^4$  Bq, for the  $^{56}\text{Co}$  source.

### 2.7.2 Data Collection

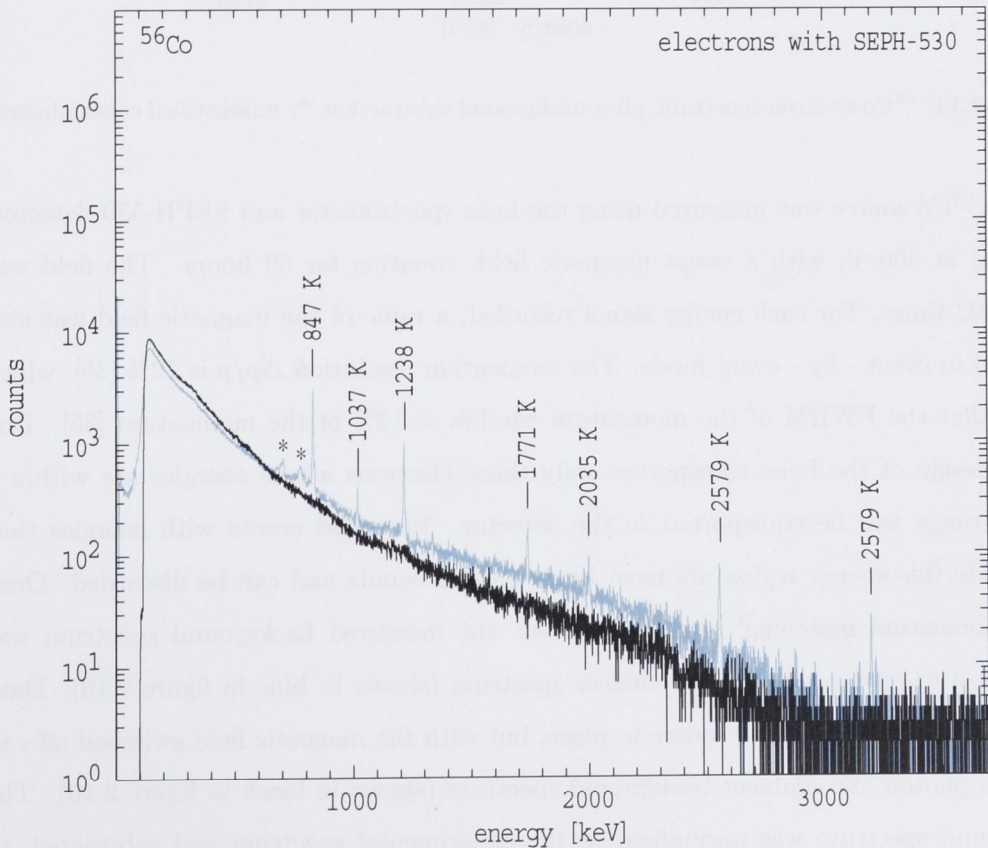


**Figure 2.10:** Blue:  $^{56}\text{Co}$  electron spectrum, black: background, \*: unidentified contaminants. The magnet current was swept between 2.7 A and 12.6 A.

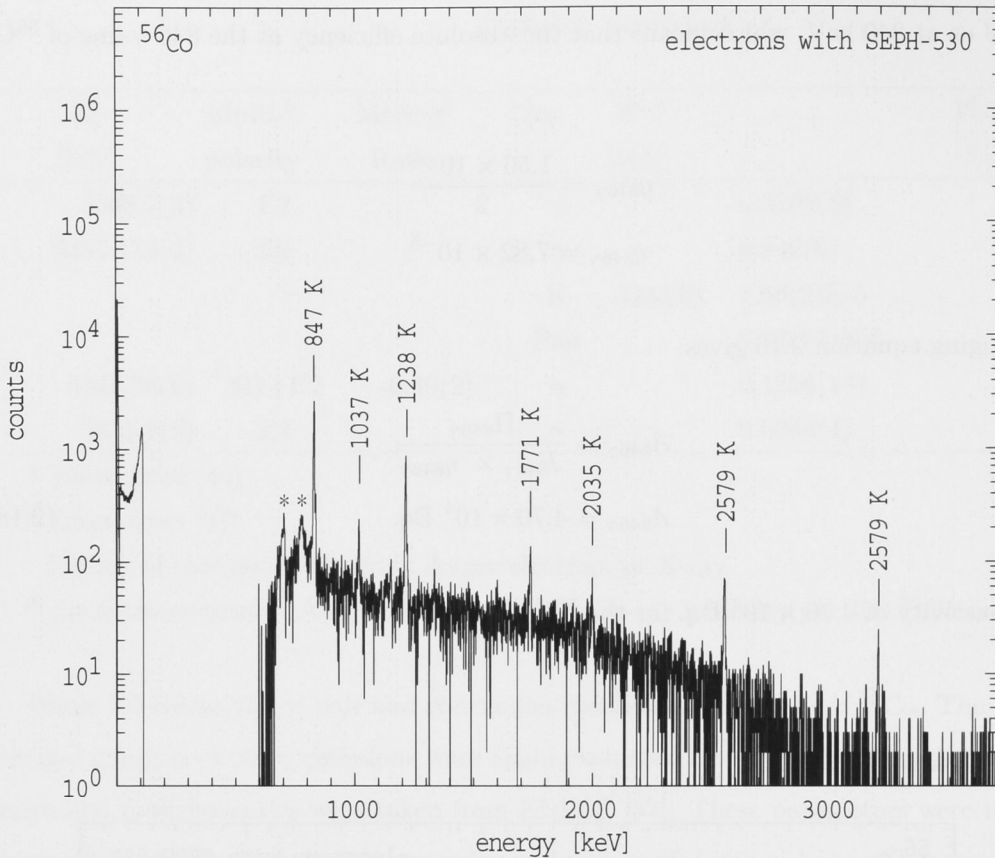


**Figure 2.11:**  $^{56}\text{Co}$  electron spectrum, after background subtraction, \*: unidentified contaminants.

The  $^{56}\text{Co}$  source was measured using the Lens spectrometer and SEPH-530 detector, operated at 400 V, with a swept magnetic field, counting for 69 hours. The field was swept 422 times. For each energy signal recorded, a value of the magnetic field was also recorded in event - by - event mode. The momentum resolution  $\Delta p/p$  is 12% [35], which means that the FWHM of the momentum window is 12% of the momentum [35]. Due to the design of the Lens transporter, only those electrons whose energies are within a narrow range will be transported to the detector. Recorded events with energies that lie outside this energy region are most likely photon counts and can be discarded. Once this “momentum matching” was carried out, the measured background spectrum was subtracted to give a considerably cleaner spectrum (shown in blue in figure 2.10). Data were then collected with the source in place, but with the magnetic field switched off - to obtain a photon and ambient background spectrum (shown in black in figure 2.10). The background spectrum was normalised to the experimental spectrum and subtracted, to give figure 2.11. The background subtraction is not perfect, the background run shows a higher count rate at low energy as compared to the spectrum with the lens energised.

---

This is due to the effect of the magnetic field of screening knock-on electrons that may be produced by energetic photons interacting with the chamber material.

The measurements described in this chapter provide valuable calibration ahead of the measurement of the Hoyle state in  $^{12}\text{C}$ . However, the statistics at high energy (above 3 MeV) in the  $^{56}\text{Co}$  measurement were quite low. Simulations were used to reinforce the measurements, and “fill in the blanks” in energy. With a view to designing the new detector for the  $^{12}\text{C}$  measurement, the aim was to investigate the properties of silicon detectors in general and more specifically, the dependence of efficiency on energy and angle. Simulations can also provide further insight, *e.g.* the required thickness, and can be used to investigate the causes of efficiency loss. Such information would have relevance beyond the  $^{12}\text{C}$  measurement, to silicon detector design and characterisation in general. Of course, a simulation system can only be as accurate as the physical models it uses, discussed in the next chapter.

The main topic of the present work is the study of the effect of the magnetic field on the rate of the reaction...

The measurements described in this paper provide valuable information about the measurement of the rate constant in  $^{13}\text{C}$ . However, the statistics at high energy values of the  $^{13}\text{C}$  measurement were quite low. Therefore, some care must be taken in the measurement, and it is the purpose of this paper to describe the method...

It is shown that the rate constant is independent of the magnetic field in the range of the present study...

The  $^{13}\text{C}$  measurement was carried out with the use of a magnetic field of 100 G. The rate constant was found to be independent of the magnetic field in the range of the present study. This result is in agreement with the theoretical prediction...



---

# Simulation with PENELOPE

---

The following is a summary of the treatment by PENELOPE of the fundamental interactions with matter, drawing heavily on the PENELOPE manual [8], with reference to previous research that the PENELOPE models have been based on. Some depth of understanding of the atomic physics involved is necessary for the developments based on this work. Examples of the energy and angular dependences of the relevant cross sections in silicon are provided to relate the models to the experimental measurements presented in section 2. In this chapter, I will present:

1. Penelope physics
  - (a) Electrons and positron interactions
  - (b) Photon interactions
2. Review of relevant Monte Carlo methods used by PENELOPE
3. PENELOPE implementation - the input files required to run PENELOPE

## 3.1 Electrons and Positrons

The fundamental interactions of electrons and positrons with matter are (see figure 3.1):

- a) Elastic scattering of an electron by an atom, which results in the electron being deflected through an angle  $\theta$ . Elastic scattering is responsible for most (but not all) of the angular deflections suffered by electrons in a bulk material.
- b) Inelastic scattering from atoms, resulting in excitation or ionisation. The primary electron or positron loses an energy  $W$ , having a final energy  $E' = E - W$ . In the case of ionisation, the ionised electron will have an energy  $E_s = E - E' - U_i$ , where  $U_i$  is the binding energy of the shell  $i$ . At low energy inelastic scattering is the dominant form of energy loss for electrons and positrons interacting with matter.

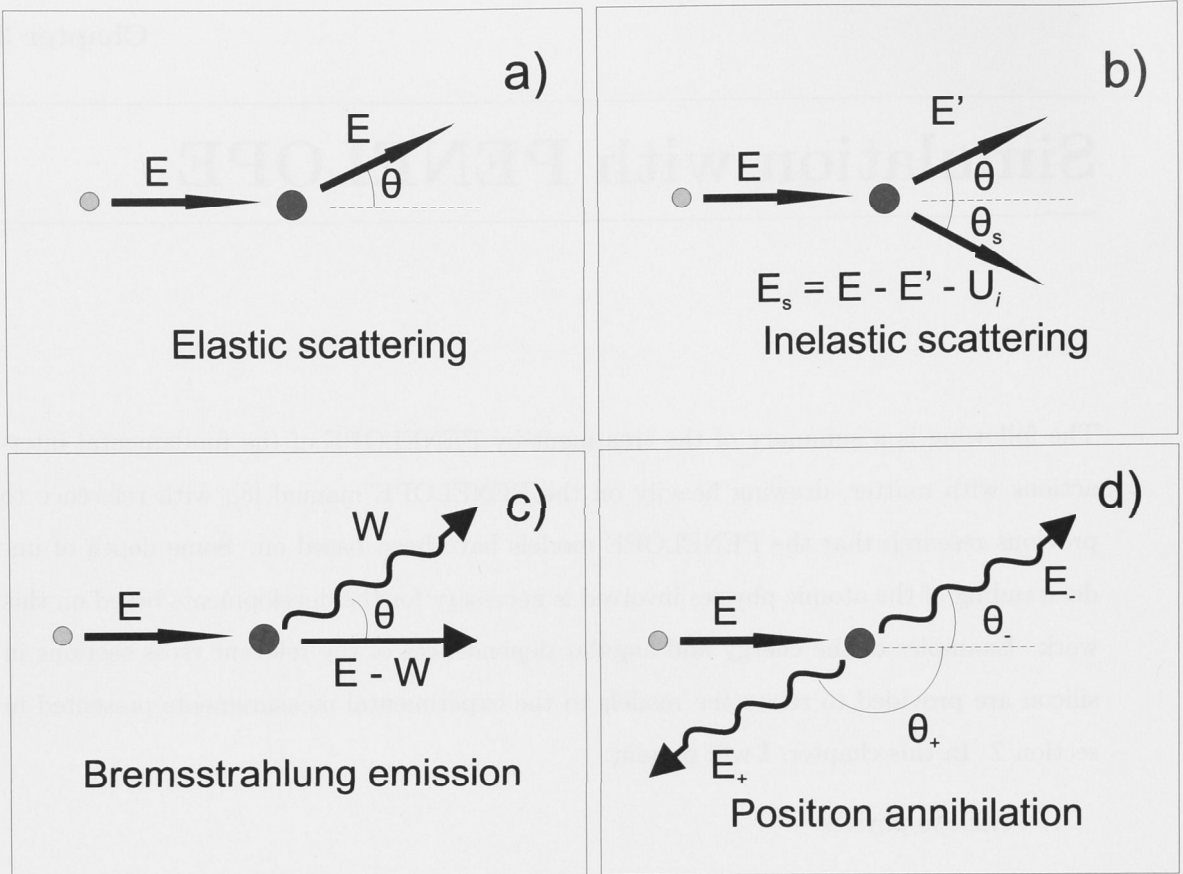


Figure 3.1: Basic types of interaction of electrons with matter.

c) Bremsstrahlung emission, where an electron or positron interacts with the atom and produces a photon of energy  $W$ . At high energy, bremsstrahlung emission is the dominant form of energy loss for electrons and positrons.

d) Positron annihilation - unlike the other three interaction mechanisms mentioned above, positron annihilation is unique to positrons interacting with atoms. The positron will disappear, creating two "annihilation" photons, one at an energy  $E_+$  and angle  $\theta_+$ , the other at energy  $E_-$  and an angle  $\theta_-$ .

### 3.1.1 The Treatment of Elastic Scattering in PENELOPE

For the case of bombarding electrons, elastic scattering is an important process, as the angular deflections can be relatively large. Elastic collisions are defined as those collisions that do not change the state of the target atom, normally the ground state. In an elastic collision, the movement of the electron through the Coulomb field of the atom causes a deflection. The angular deflections of electron trajectories are

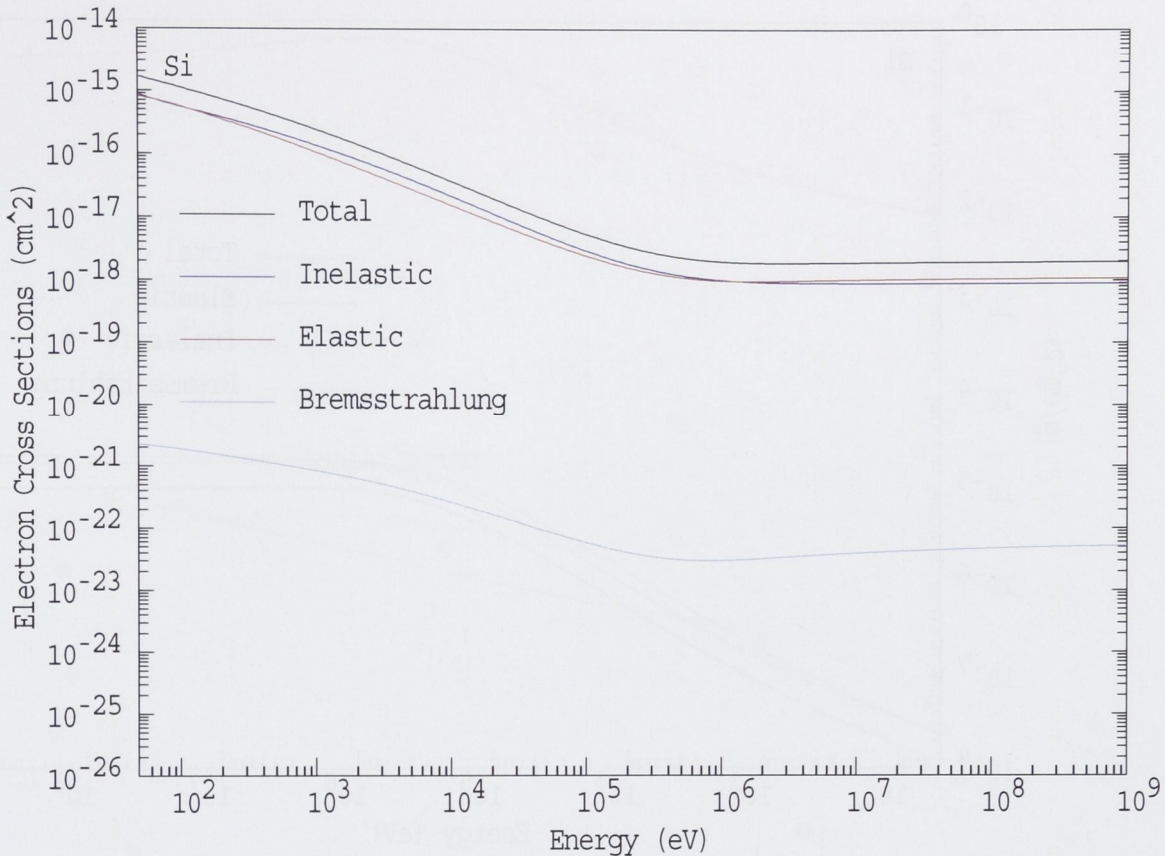


**Figure 3.2:** Electron interaction cross sections for silicon.

mostly (but not completely) due to elastic scattering. There is, of course, a transfer of energy from projectile to target, which causes the target to recoil. However, for the case of electron scattering, the mass of the target is large enough ( $\approx 3600Zm_e$ ) that the average energy imparted is a very small fraction of the bombarding energy (a few meV for scattering of 30 keV electrons by aluminium atoms). It is usually neglected, which is equivalent to assuming the target has an infinite mass and does not recoil.

We will restrict ourselves to discussing elastic collisions within the energy range of the relevant experiments, that is, from a few keV to 3.5 MeV. Elastic collisions within this energy region can be described as scattering of the projectile by the electrostatic field of the target atom [45]. The charge distribution of the target atom consists of the nucleus and the electron cloud. PENELOPE calculates the density distribution of atomic electrons using a self-consistent Hartree-Fock code [46]. PENELOPE assumes a spherical charge distribution for closed shell atomic configurations, and for open shell configurations,

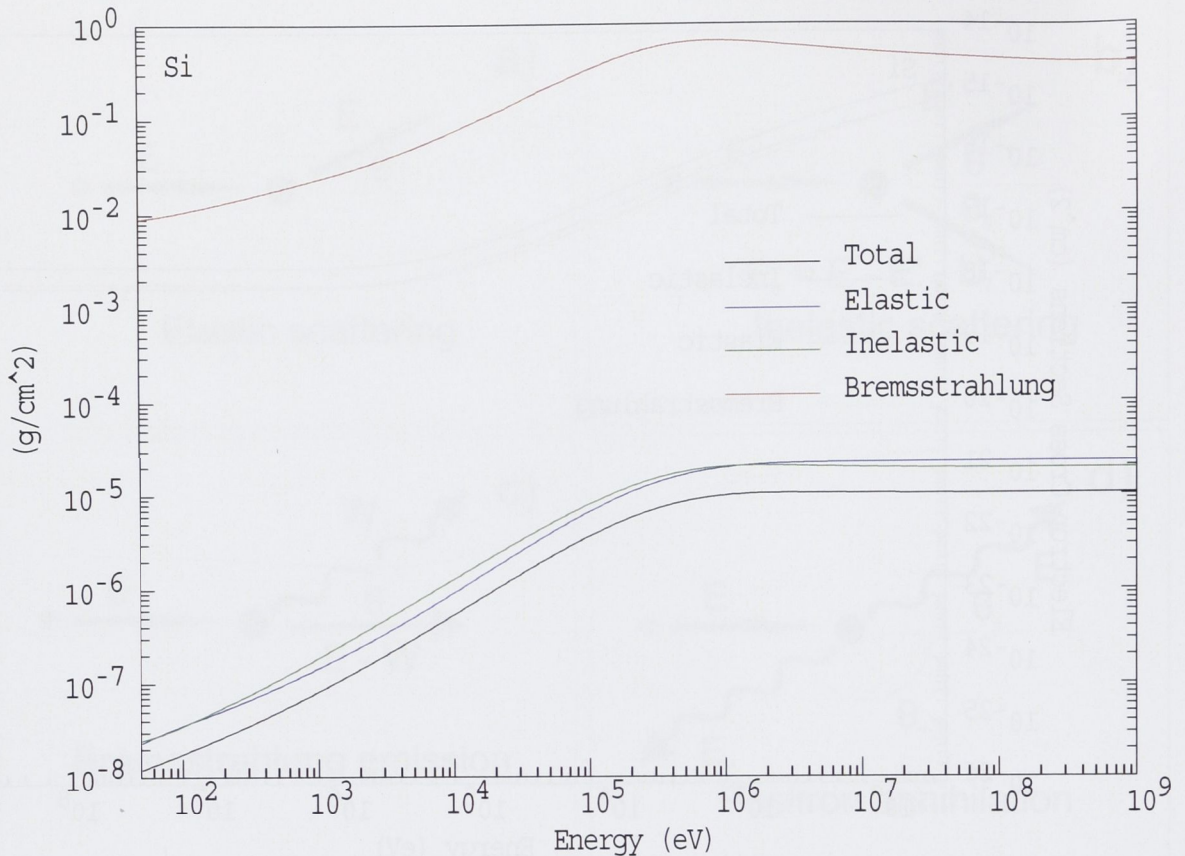


**Figure 3.3:** Electron interaction mean free paths for silicon.

performs an average over all directions to give an average spherical density  $\rho_e(r)$ . The finite size of the nucleus only becomes of marked importance for projectile energies above 10 MeV [47]. At the highest energies sampled in the Monte Carlo experiments presented here, namely of 3.5 MeV, the finite size of the nucleus has only a very slight effect on the cross sections for elastic scattering [8] (but is taken into account anyway). PENELOPE uses a Fermi distribution [47] to describe the charge distribution of the nucleus

$$\rho_n(r) = \frac{\rho_0}{\exp[(r - R_n)4 \ln(3/t)] + 1}, \quad (3.1)$$

where  $R_n$  is the mean radius (or half density radius) and  $t$  is the surface or “skin thickness” (defined as the distance over which  $\rho_n$  drops from  $\approx 0.9$  to  $\approx 0.1$  of its central value). These two parameters are given by

$$\begin{aligned} R_n &= 1.07 \times 10^{-15} A_m^{1/3} \text{ m}, \\ t &= 2.4 \times 10^{-15} \text{ m}, \end{aligned} \quad (3.2)$$

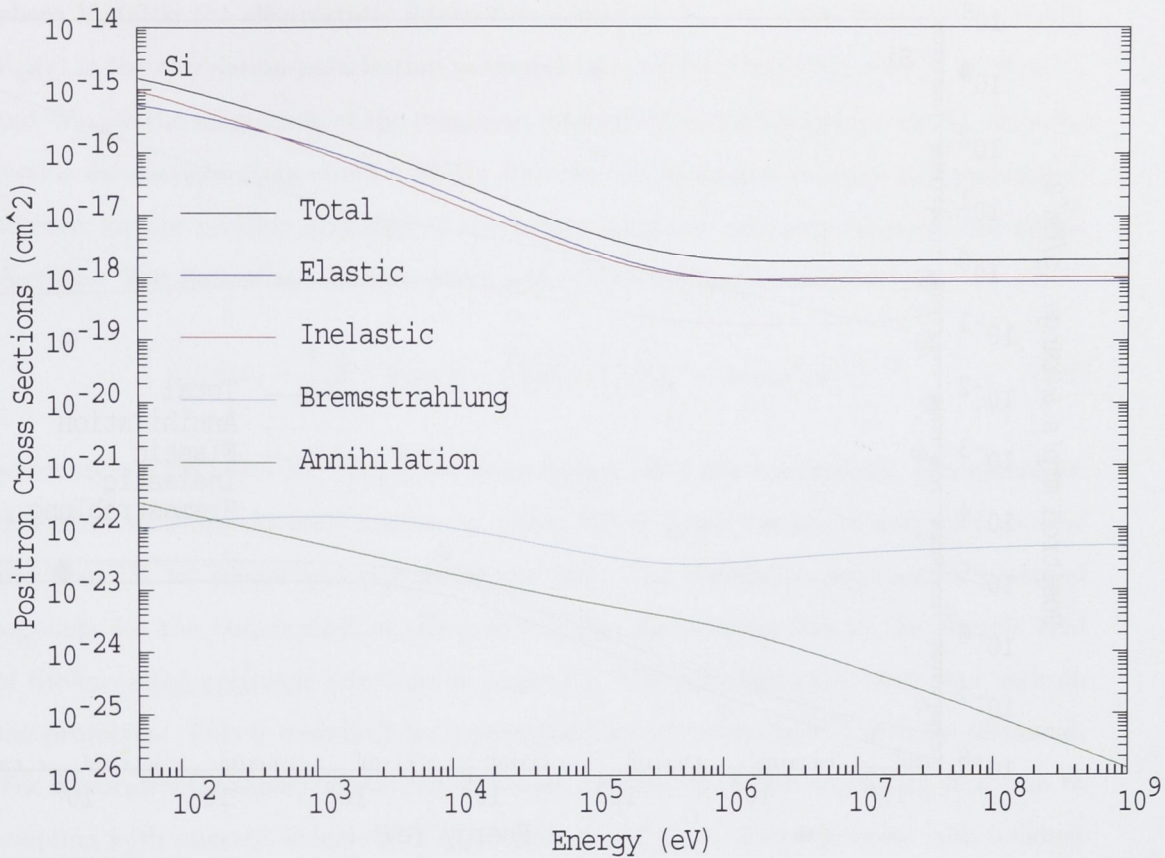


**Figure 3.4:** Positron interaction cross sections for silicon.

where  $A_m$  is the atomic mass of the element. The constant  $\rho_0$ , which equals twice the proton density at  $r = R_n$ , is determined by normalisation,

$$Z = 4\pi \int_0^\infty \rho_n(r)r^2 dr. \quad (3.3)$$

The electrostatic potential of the target atom is [8]

$$\frac{\varphi(r)}{4\pi e} = \left[ \frac{1}{r} \int_0^r \rho_n(r')r'^2 dr' + \int_r^\infty \rho_n(r')r' dr' \right] - \left[ \frac{1}{r} \int_0^r \rho_e(r')r'^2 dr' + \int_r^\infty \rho_e(r')r' dr' \right], \quad (3.4)$$

where the first two terms are the contribution from the nucleus, and the last two terms are the contribution from the electron cloud.

To calculate elastic scattering cross sections, PENELOPE uses the program ELSEPA (ELastic Scattering of Electrons and Positrons by Atoms) [48, 49]. From energies of a few eV up to a few hundred keV, ELSEPA uses a semi-empirical optical-model potential,

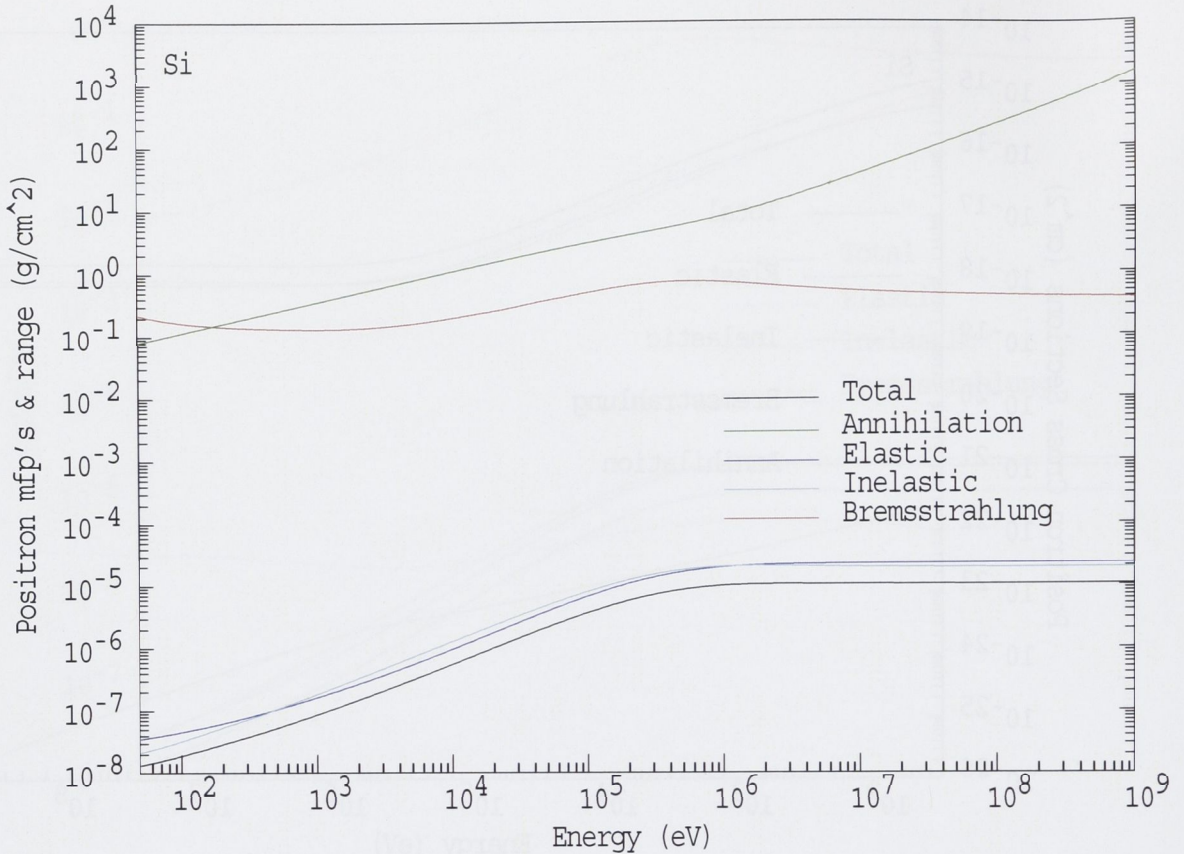


**Figure 3.5:** Positron interaction mean free paths for silicon.

with an imaginary absorptive part, that yields results in close agreement with available experimental data for electron elastic scattering in gases [48]. For larger energies, ELSEPA uses a static-field approximation, where the target atom is assumed to be a frozen charge distribution, and the interaction with the projectile is assumed to reduce the electrostatic interaction [45].

At energies below 10 keV, the accuracy of the static-field approximation worsen dramatically due to the combined effects of loss of flux due to inelastic absorption, and atomic-charge polarisability. These effects are accounted for by introducing an absorption and polarisation potential into the atomic cross section. The optical-model potential describes the effective interaction between a projectile at  $\mathbf{r}$  and the target is described by means of the potential:

$$V(r) = V_{st}(r) + V_{ex}(r) + V_{cp}(r) - iW_{abs}(r) \quad (3.5)$$

where  $V_{st}(r)$  is the electrostatic interaction potential,  $V_{ex}(r)$  is the exchange potential,  $V_{cp}(r)$  is the correlation-polarisation potential (needed for projectiles with  $E < 10$  keV), and  $W_{abs}$  is the magnitude of the imaginary absorption potential (which affects the cross section for energies up to about 1 MeV). The electron-exchange interaction is included to account for the possible exchange of the indistinguishable projectile electron and target electrons. The default is a Furness MacCarthy (FM) exchange potential [48]:

$$V_{ex}^{(-)}(r) = \frac{1}{2}[E - V_{st}(r)] - \frac{1}{2}\{[E - V_{st}(r)]^2 + 4\pi a_0 e^4 \rho(r)\}^{1/2}, \quad (3.6)$$

where  $a_0 = 5.291772 \times 10^{-9}$  cm is the Bohr radius. At a few hundred eV, accounting for this effect modifies the cross section by about 3% at 5 keV for silicon and gold, and by less than 1% for silicon and gold at 30 keV [49]. The correlation-polarisation potential accounts for the polarisation of the target charge distribution due to the electric field of the incoming projectile (electron or positron). The polarised atom then acts back on the projectile. This is described by a potential that decreases as  $r^{-4}$  at large distances. The absorptive imaginary potential accounts for loss of elastic scattering flux due to coupling with inelastic channels. The magnitudes of these effects decrease with incident energy. The effect of polarisation becomes negligible for  $E \approx 10$  keV; absorption effects remain appreciable up to relatively high energies, of the order of 1 MeV or higher, depending on the atomic number of the target [48]. Polarisation and absorption effects have about a 5% effect in silicon at 5 keV and about a 10% effect in gold at the same energy [49].

The PENELOPE code defines the elastic scattering in terms of the polar and azimuthal angles,  $\theta$  and  $\phi$  respectively, and uses the quantity called polar deflection

$$\mu = (1 - \cos \theta)/2 \quad (3.7)$$

instead of the scattering angle  $\theta$ . Note that  $\mu$  varies from 0 (forward scattering) to 1 (backward scattering). The cross section per unit angular deflection is

$$\frac{d\sigma_{el}}{d\mu} = 4\pi \frac{d\sigma_{el}}{d\Omega}. \quad (3.8)$$

Figure 3.6 shows the cross sections calculated by ELSEPA for elastic scattering of electrons and positrons on silicon for various energies. As the interaction  $V(r)$  is attractive for electrons and repulsive for positrons, the scattering is more intense for electrons than

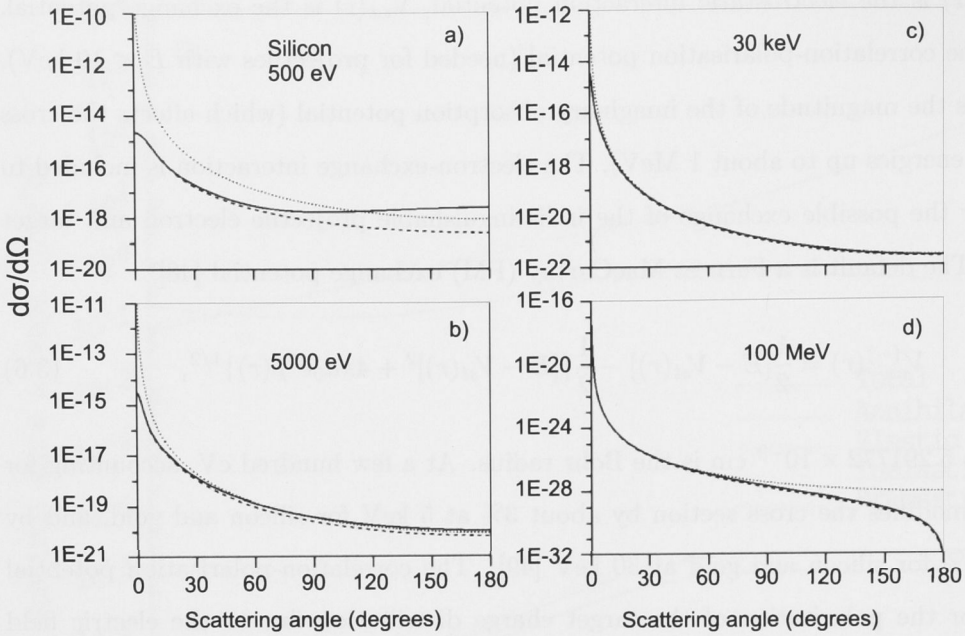


**Figure 3.6:** Calculated differential cross sections for elastic scattering of electrons (solid lines) and positrons (dashed lines) calculated by ELSEPA for silicon assuming the Dirac-Fock electron-density function and the point nucleus model [49]. The dotted line shows the relativistic Rutherford cross section. Energy of: (a) 500 eV; (b) 5000 eV; (c) 30 keV; and (d) 100 MeV.

positrons - the electrons can fall deeper into the potential well - whereas the positrons are repelled and cannot “feel” the inner region of the atom. The relativistic Rutherford cross section is shown for comparative purposes, but is not used by PENELOPE.

PENELOPE calculates the cross sections for compounds and mixtures by taking the incoherent sum of scattered intensities. This is equivalent to neglecting chemical binding effects. Comparison with more rigorous methods has shown that this is a reasonable approximation [8]. As the scattering events are axially symmetric about the angle of incidence, PENELOPE uniformly samples the azimuthal angle  $\phi$  in the interval  $(0, 2\pi)$  using the sampling formula  $\phi = 2\pi\eta$  where  $\eta$  is a random number from 0 to 1. On start-up of the program, PENELOPE will produce a new table of cross sections with 200 logarithmically spaced points in energy, spanning the energy range used in the simulation. This table is determined from the input table by cubic spline interpolation. For each grid energy, the program determines the probability density function (PDF) for the angular deflection  $\mu$ ,

$$p_{el}(E_i; \mu) = \frac{1}{\sigma_{el}} \frac{d\sigma_{el}}{d\mu} = \frac{4\pi}{\sigma_{el}} \frac{d\sigma_{el}}{d\Omega}, \quad (3.9)$$



which is tabulated for the 606 angular deflections in the ELSEPA database. These are transformed into continuous functions in  $\mu$  from which random values are generated. To save on computation time, PENELOPE uses linear interpolation for those events in which the energy of the incident particle  $E$  does not fall on the grid.

### 3.1.2 Inelastic Scattering in PENELOPE

Inelastic collisions are the dominant mechanisms for energy loss by electrons and positrons with low and intermediate energies. They produce electronic excitations and ionisations in the medium. They may also produce secondary knock-on electrons (delta rays) and secondary de-excitation photons, both of which carry away part of the primary energy, and must be stopped fully in order for a complete energy signal.

Bohr established a semi-classical theory of inelastic collisions, where collisions were characterised by an impact parameter  $b$ , which is roughly the distance of closest approach to the centre of the atom. Bethe then formulated a quantum-mechanical treatment, where collisions are characterised by their momentum transfer  $q$  - an observable quantity, as opposed to  $b$ . The vector  $q$  is a function of the energy transfer  $E_n$  and the angular deflection  $\theta$  experienced by the projectile. The loss of energy per unit path length due to inelastic events is given by

$$-\frac{dE}{ds} = \sum_i N_i \sum_n E_{ni} \sigma_{ni}, \quad (3.10)$$

where  $\sigma_{ni}$  is the cross section for inelastic collision that raises an atom of type  $i$  to an energy level  $E_{ni}$  above its ground state, and where  $N_i$  is the density of atoms (or molecules).

The effect of individual inelastic collisions on the *projectile* is completely specified by the energy transfer  $W$  and the polar and azimuthal scattering angles  $\theta$  and  $\phi$ , respectively. It is customary to refer to the recoil energy  $Q$ , first with relativistic correction, then in the non-relativistic case

$$Q(Q + 2m_e c^2) = (cq)^2 \quad (3.11)$$

$$Q \approx q^2/2m \quad (\text{nonrelativistic}), \quad (3.12)$$

PENELOPE uses the relativistic formula. The parameter  $q$  is the magnitude of the momentum transfer  $\mathbf{q} \equiv \mathbf{p} - \mathbf{p}'$ , where  $\mathbf{p}$  and  $\mathbf{p}'$  are the linear momenta of the projectile

before and after the collision.  $Q$  is the kinetic energy of an electron that moves with a linear momentum equal to  $q$ . In the limit of large  $q$ ,  $Q$  coincides with the energy transfer  $E_n$ . The cross section for collisions with energy loss  $W$  and recoil energy  $Q$ , obtained from the first Born approximation can be written [51].

$$\frac{d^2\sigma}{dQdW} = \frac{\pi e^4}{E_n} \frac{1}{WQ} \frac{df(W, Q)}{dW} \quad (3.13)$$

The factor  $df(Q, W)/dW$  is the atomic generalised oscillator strength within the Born approximation. PENELOPE uses a form of the above Bethe atomic cross section equation that is corrected for relativistic effects. The result was obtained in the Coulomb gauge [53]. By applying the Born approximation, and assuming a Coulombic interaction, Bethe obtained the following expression for the differential cross section for elastic scattering of a particle by a stationary atom [51]:

$$d\sigma_n = 2\pi z^2 e^4 (mv^2)^{-1} Q^{-1} |\epsilon_n(q)|^2 d(\ln Q), \quad (3.14)$$

where  $m$  and  $v$  are the mass and velocity of the colliding particle, and  $q$  is the magnitude of the momentum transfer. Equation 3.14 may be viewed as the product of two factors, relating to different physics. The factor  $2\pi z^2 e^4 (mv^2)^{-1} \times Q^{-1} d(\ln Q)$  is evaluated from observable quantities *i.e.*, the momentum transfer and the scattering angle, and relate to the incident particle only. It is in fact, the Rutherford cross section [54] for the scattering of a particle with charge  $ze$  by a *free and initially stationary electron*, which upon the collision receives a recoil energy ranging from  $Q$  to  $Q + dQ$ . In this simplified situation, a given momentum transfer  $\hbar q$  results in a unique value  $Q$  of energy transfer. In reality, the energy is shared between a certain kinetic energy imparted to the atom as a whole, and the internal excitation of the atom. This results in multiple possibilities for the degree of internal excitation, due to the fact that the atomic electrons responsible for excitation are initially bound rather than free. This situation is described by the remaining factor in equation 3.14,  $|\epsilon_n(q)|^2$ , which gives the probability that the atom makes the transition to the excited state  $n$  upon receiving a momentum transfer  $\hbar q$  [56].

The generalised oscillator strength is difficult to evaluate theoretically, due to the lack of sufficiently accurate eigenfunctions of atomic or molecular systems in the ground state, and especially in excited states. In fact, the generalised oscillator strength is only

characterised analytically for two simple systems: hydrogen ions and the free-electron gas. Even in these cases, the generalised oscillator strengths are too complex (*i.e.*, too computationally intensive) for use in the simulations. The generalised oscillator strength though, has been studied extensively for atomic hydrogen [57, 58] and some of its features are valid for any atom or molecule. The generalised oscillator strength can be represented comprehensively by a three dimensional plot of  $df(Q, W)/dW$  as a function of  $\ln(Qa_0)^2$  and  $E$ , called the *Bethe surface*. The Bethe surface embodies all information about the inelastic scattering of electrons and positrons within the first Born approximation (except secondary electrons). PENELOPE's method for the simulation of inelastic collisions is basically a topographical study of this surface. Inelastic collisions can be characterised by a few global features of the Bethe surface [8].

PENELOPE divides the Bethe surface into two distinct regions, following the method first proposed by Bohr in 1948. The first being a region of low momentum transfer, that results in resonance-like interactions with bound electrons, and another characterised by high momentum transfer, where due to large momentum transfer, the atomic electrons may be regarded as free. These correspond to different parts of the Bethe surface [51]. The resonant interactions correspond to excitation of the target; the interactions where the electron is considered as free correspond to ionisations. In the free electron region (or large momentum transfer), the Bethe surface reduces to a ridge peaked at  $Q = W$ , *i.e.*, on average, the relation  $Q = W$  holds apart from a fluctuation (a broadening due to the motion of the atomic electrons). PENELOPE disregards this broadening, as the effect is deemed to be negligibly small in the case of electrons and positrons. The transition from resonance to free interactions is estimated to occur when the momentum transfer energy  $Q$  exceeds the typical resonance energy transfer [59]. In fact, PENELOPE draws the line between these two regions at the ionisation energy  $U_k$ . For soft collisions (low energy transfer) the generalised oscillator strength is nearly constant with  $Q$  and decreases rapidly with  $W$ .

PENELOPE's generalised oscillator strength model for inelastic scattering is designed for fast sampling of  $W$  and  $Q$ . Following the model outlined by Liljequist [60], the assumption that the generalised oscillator strength is comprised of contributions from the different atomic shells is made. Each atomic shell  $k$  is characterised by the number  $Z_k$  of electrons in the shell, and the ionisation energy  $U_k$ . In the Liljequist model adopted

by PENELOPE, the generalised oscillator strength of each atomic shell is modeled as a “ $\delta$ -oscillator”, which is an entity with a simple generalised oscillator strength given by

$$F(W_k; Q, W) = \delta(W - W_k)\Theta(W_k - Q) + \delta(W - Q)\Theta(Q - W_k), \quad (3.15)$$

where  $\delta(x)$  is the Dirac delta function and  $\Theta(x)$  is the step function. The first term represents the low- $Q$  interactions, which are described as a single resonance at the energy  $W_k$ ; the second term corresponds to large- $Q$  interactions in which the target electrons react as if they were free and at rest ( $W = Q$ ). Notice that the oscillator generalised oscillator strength satisfies the sum rule

$$\int_0^\infty F(W_k; Q, W)dW = 1 \text{ for any } Q \quad (3.16)$$

and, as the corresponding integral over the whole atom has to equal  $Z$ , the number of electrons, a  $\delta$  oscillator corresponds to one electron in the target. The Liljequist generalised oscillator strength model for the whole atom is given by

$$\frac{df(Q, W)}{dW} = \sum_k f_k [\delta(W - W_k)\Theta(W_k - Q) + \delta(W - Q)\Theta(Q - W_k)], \quad (3.17)$$

where the summation in  $k$  extends over all bound electron shells (and the conduction band, in the case of conductors). Note that the Bethe sum rule

$$\sum_k f_k = Z, \quad (3.18)$$

is satisfied. Another constraint is that the excitation energies must be defined in such a way that the generalised oscillator strength model leads to the accepted value of the mean excitation energy  $I$ ,

$$\sum_k f_k \ln W_k = Z \ln I. \quad (3.19)$$

Low momentum transfer (soft excitations) contribute the most to the total cross section. The contribution made by resonance excitations to the generalised oscillator strength can be called the optical oscillator strength. The optical oscillator strength of weakly bound electrons mostly determines the cross section [8]. The outermost shells in conductors and semiconductors form the conduction band (cb). These electrons move quite freely throughout the medium, so their binding energy is set to 0. Electrons in the conduction

band are described by a single oscillator  $f_{cb}$  and resonance energy  $W_{cb}$ . These parameters should agree with the effective number of electrons per atom or molecule, that participate in plasmon excitations and the plasmon energy. They can be estimated from empirical data *e.g.*, from electron energy-loss spectra or from measured optical data. When this data is not available PENELOPE will fix the value of  $f_{cb}$  as the number of electrons with ionisation energies less than 15 eV and set the resonance energy  $W_{cb}$  equal to the plasmon energy of a free-electron gas with the same density as that of conduction electrons,

$$W_{cb} = \sqrt{4\pi N f_{cb} \hbar^2 e^2 / m_e} = \sqrt{\frac{f_{cb}}{Z}} \Omega_p, \quad (3.20)$$

where  $\Omega_p$  is the plasma energy of a free-electron gas with the electron density of the medium given by:

$$\Omega_p^2 = 4\pi N Z \hbar^2 e^2 / m_e, \quad (3.21)$$

where  $N$  is the number of atoms per unit volume. This approximation is more realistic for those materials that more closely resemble free-electron states (such as aluminium).

In PENELOPE, the target atoms are assumed to be in their ground state configuration. The ionisation energy  $U_i$ , number of electrons  $Z_i$  of each electron shell, and the empirical value of the mean excitation energy  $I$  must be specified. The adopted  $I$ -values are those proposed by Berger and Seltzer [61], which were also used to generate the ICRU (1984) tables of stopping powers for electrons and positrons. As mentioned earlier, the model assumes a zero-width Bethe ridge - deemed only to be a problem for heavy ion projectiles. It also disregards the fact that for low- $Q$  transitions, there is a transfer of oscillator strength from inner to outer shells [62]. This makes the shell ionisation cross section only approximate, however due to the low-probability of inner shell ionisation, they only have a very small effect on the global transport properties.

The user specifies a cutoff value  $W_{cc}$ . Collisions that involve energy transfers below this cutoff are simulated collectively, by means of multiple-scattering approximations. Collisions involving energy transfers above  $W_{cc}$ , are called hard collisions and are simulated by a detailed calculation. The PENELOPE code uses the generalised oscillator strength model only to simulate the effect of inelastic collisions on the projectile and the secondary knock-on electrons. The relaxation of atoms from excited states by X-ray

or Auger electron emission is simulated by means of more accurate ionisation cross sections.

The model is readily applied to compounds and mixtures - the oscillators may pertain to either atoms or molecules. If the value of the mean excitation energy of the compound is unknown, it is estimated from Bragg's additivity rule. In the case of a compound  $X_xY_y$ , in which the molecules consist of  $x$  atoms of the element  $X$  and  $y$  atoms of the element  $Y$ , the number of electrons per molecule is  $Z_M = xZ_X + yZ_Y$ , where  $Z_X$  stands for the atomic number of element  $X$ . According to the additivity rule, the generalised oscillator strength of the compound is approximated as the sum of the atomic generalised oscillator strengths of the atoms so that

$$Z_M \ln I = xZ_X \ln I_X + yZ_Y \ln I_Y, \quad (3.22)$$

where  $I_X$  denotes the mean excitation energy of element  $X$ .

In the case of compounds and mixtures with several elements, the number of electron shells may be too large to permit simulation of each electron shell with the same detail. In these situations, PENELOPE groups together outer shells with similar resonance energies, and replaces them by a single oscillator of strength equal to the sum of strengths of the original oscillators. The resonance energy of the group oscillator is set by requiring that its contribution to the mean excitation energy  $I$  equals the sum of contributions of the grouped oscillators, ensuring that grouping will alter the stopping power in the right way.

## Cross Sections

PENELOPE splits the cross sections for inelastic collisions into contributions from distant longitudinal, distant transverse and close interactions,

$$\frac{d^2\sigma_{in}}{dWdQ} = \frac{d^2\sigma_{dis,l}}{dWdQ} + \frac{d^2\sigma_{dis,t}}{dWdQ} + \frac{d^2\sigma_{clo}}{dWdQ}. \quad (3.23)$$

The cross sections are obtained from the generalised oscillator strength method outlined earlier. As was the case with elastic collisions, the cross section for close collisions of electrons must be adjusted to take into account the indistinguishability of projectile and target electrons. This is a small effect for distant collisions, and is neglected in

these cases. In the case of close collisions, the cross section is adjusted according to Möller.

The energy-loss cross section is defined as

$$\frac{d\sigma_{in}}{dW} \equiv \int_{Q_-}^{Q_+} \frac{d^2\sigma_{in}}{dW dQ} dQ = \frac{d\sigma_{dis,l}}{dW} + \frac{d\sigma_{dis,t}}{dW} + \frac{d\sigma_{clo}}{dW}, \quad (3.24)$$

where  $Q_-$  and  $Q_+$  are the minimum and maximum kinetically allowed recoil energies, given by  $\cos\theta = +1$  and  $-1$  respectively in the definition of  $Q$

$$Q(Q + 2m_e c^2) = (cq)^2 = c^2(p^2 + p'^2 - 2pp' \cos\theta), \quad (3.25)$$

which reduces, in the non-relativistic limit, to

$$Q_{\pm} = [E^{1/2} \pm (E - W)^{1/2}]^2. \quad (3.26)$$

Note that the continuous spectrum associated with single-distant excitations of a given atomic electron shell is approximated by  $\delta$  distributions. This gives rise to unphysical, narrow peaks at multiples of the resonance energies. However, these peaks are smoothed in the cumulative total of many inelastic scattering events. The generalised oscillator strength model then, gives a good *average* description of inelastic scattering, not of *single* scattering events.

The probability distribution function of the energy loss in a single inelastic collision ( $p_{in}$ ) is given by

$$p_{in}(W) = \frac{1}{\sigma_{in}} \frac{d\sigma_{in}}{dW}, \quad (3.27)$$

where

$$\sigma_{in} = \int_0^{W_{max}} \frac{d\sigma_{in}}{dW} dW \quad (3.28)$$

is the total cross section for inelastic collisions.

The mean free path  $\lambda_{in}^{-1} = N\sigma_{in}$ , where  $N$  is the number of scattering centres (atoms or molecules) per unit volume. The stopping power is defined by

$$S_{in} = N\sigma_{in}^{(1)} = \frac{\langle W \rangle}{\lambda_{in}}. \quad (3.29)$$

The integrated cross section  $\sigma_{in}^{(n)}$  can be expressed as the sum of contributions from distant, transverse interactions  $\sigma_{dis,t}^{(n)}$ , distant longitudinal interactions  $\sigma_{dis,l}$ , and close interactions  $\sigma_{clo}^{(n)}$ .

$$\sigma_{in}^{(n)} = \sigma_{dis,l}^{(n)} + \sigma_{dis,t}^{(n)} + \sigma_{clo}^{(n)}. \quad (3.30)$$

### Simulation of Hard Inelastic Collisions

The generalised oscillator strength model permits the random sampling of the energy loss  $W$  and the angular deflection  $\theta$  using purely analytical methods. In general, however, only hard collisions, those with an energy loss larger than a specified cutoff value  $W_{cc}$ , are simulated. The cutoff energy  $W_{cc}$  is specified by the user.

To simulate a hard collision, PENELOPE first must choose the type of collision, *i.e.*, which oscillator to use.

$$\sigma(W_{cc}) \equiv \int_{W_{cc}}^{W_{max}} \frac{d\sigma_{in}}{dW} dW = \sigma_{dis,l}(W_{cc}) + \sigma_{dis,t}(W_{cc}) + \sigma_{clo}(W_{cc}) \quad (3.31)$$

$$= \sum_k \sigma_k(W_{cc}), \quad (3.32)$$

as well as the contribution from each oscillator,  $\sigma_k(W_{cc})$ . The active oscillator is sampled from the point probabilities  $p_k = \sigma_k(W_{cc})/\sigma(W_{cc})$ . PENELOPE calculates these probabilities at initialisation time, and stores them in the memory. A larger value of  $W_{cc}$  will speed up the simulation - potentially at the cost of accuracy.

### Secondary Electron Emission

After a hard collision with a bound electron, the primary electron/positron has kinetic energy  $E - W$ , the “secondary” electron (delta-ray) is ejected with kinetic energy  $E_s = W - U_i$ , and the residual ion is left in a state with excitation energy equal to  $U_i$  in shell  $i$ . The atom will release the energy in the form of an X-ray or Auger electron, however the above-described model does not accurately describe the emission of Auger electrons or X-rays; they are simulated by a separate system, see 3.1.2.

The direction of the delta-ray, however, is chosen by collision kinematics. With the assumption that the target electron is initially at rest, the delta-ray is emitted in the direction of the momentum transfer  $\mathbf{q}$ , and the polar emission angle  $\theta_s$  coincides with the



recoil angle  $\theta_r$

$$\cos^2 \theta_s = \frac{W^2/\beta^2}{Q(Q + 2m_e c^2)} \left( 1 + \frac{Q(Q + 2m_e c^2) - W^2}{2W(E + m_e c^2)} \right)^2. \quad (3.33)$$

In the case of close collisions ( $Q = W$ ), this expression simplifies to

$$\cos \theta_s(Q = W) = \left( \frac{W}{E} \frac{E + 2m_e c^2}{W + 2m_e c^2} \right)^{1/2}. \quad (3.34)$$

The momentum transfer lies on the scattering plane - the plane formed by the initial and final momenta of the projectile, so the azimuthal emission angle is  $\phi_s = \pi + \phi$ . The assumption that the target electrons are initially at rest disregards ‘‘Doppler broadening’’ of the angular distribution. However, the energies of the emitted electrons are typically much smaller than those of the incident particle, so their directions will become quickly randomised by elastic and inelastic events (much shorter than the transport mean free path of the projectile [8]).

### Ionisation of Inner Shells

The generalised oscillator strength model does not adequately describe the ionisation of inner shell electrons. The correlation between energy loss/scattering of the projectile and ionisation events is of minor importance, and is neglected [8]. Hence, inner-shell ionisation is treated as an independent process.

PENELOPE uses a total ionisation cross section obtained from an optical-data model of the generalised oscillator strength [63] to simulate the ionisation of inner shells. This model assumes the following relationship between the optical oscillator strength of the  $i$ -th inner shell,  $df_i(W)/dW$ , and the photoelectric cross section  $\sigma_{ph,i}(Z, W)$  for absorption of a photon with energy  $W$ ,

$$\frac{df_i(W)}{dW} = \frac{m_e c}{2\pi^2 e^2 \hbar} \sigma_{ph,i}(Z, W). \quad (3.35)$$

The photoelectric cross sections used are taken from the Evaluated Photon Data Library [64]. The generalised oscillator strength is modeled as a continuous superposition of  $\delta$ -

oscillators weighted by the optical oscillator strength,

$$\frac{df_i(Q, W)}{dW} = \int_{U_i}^{\infty} \frac{df_i(W')}{dW'} F(W'; Q, W) dW' + Z_r \delta(W - Q) \Theta(W - U_i) \quad (3.36)$$

with

$$Z_r = Z_i - \int_{U_i}^{\infty} \frac{df_i(Q, W)}{dW} = Z_i \text{ if } Q > U_i. \quad (3.37)$$

The Born approximation is known to overestimate the ionisation cross sections for incident electrons with kinetic energies near the ionisation threshold. This is mainly due to the effect of the electrostatic field of the target atom to increase the kinetic energy of the projectile. To offset this effect, PENELOPE assumes that the incident electron gains a kinetic energy  $2U_i$  before it interacts with a target electron, which is bound with binding energy  $U_i$ . With this ‘‘Coulomb’’ correction, the ionisation cross section for electrons is

$$\sigma_{\text{si},i}^{(-)}(E) = \int_{U_i}^{(E+U_i)/2} \frac{d\sigma_{\text{si},i}^{(-)}(E + 2U_i)}{dW} dW. \quad (3.38)$$

The correction reduces the ionisation cross section near the threshold, and yields values in close agreement with experimental data [8]. For positrons the effect of the Coulomb distortion is introduced empirically by multiplying the ionisation cross section by a global factor  $(1 + U_i/E)^{-3}$ . That is,

$$\sigma_{\text{si},i}^{(+)}(E) = \left( \frac{E}{E + U_i} \right)^3 \int_{U_i}^E \frac{d\sigma_{\text{si},i}^{(+)}(E)}{dW} dW, \quad (3.39)$$

giving positron ionisation cross sections that are smaller than those of electrons near the ionisation threshold, in qualitative agreement with experimental data [65, 66]. The molecular cross section for ionisation of inner shells is evaluated using the additivity approximation as requiring

$$\sigma_{\text{si},\text{mol}}^{(\pm)}(E) = \sum_i \sigma_{\text{si},i}^{(\pm)}(E), \quad (3.40)$$

where the summation extends over all inner shells of the atoms in the molecule.

### 3.1.3 Bremsstrahlung

Bremsstrahlung or ‘‘breaking-radiation’’ is the radiation emitted due to accelerations caused by the electrostatic field of the atoms. The continuous X-ray spectrum or bremsstrahlung, was first reported by Röntgen in 1895. The quantum mechanical theory

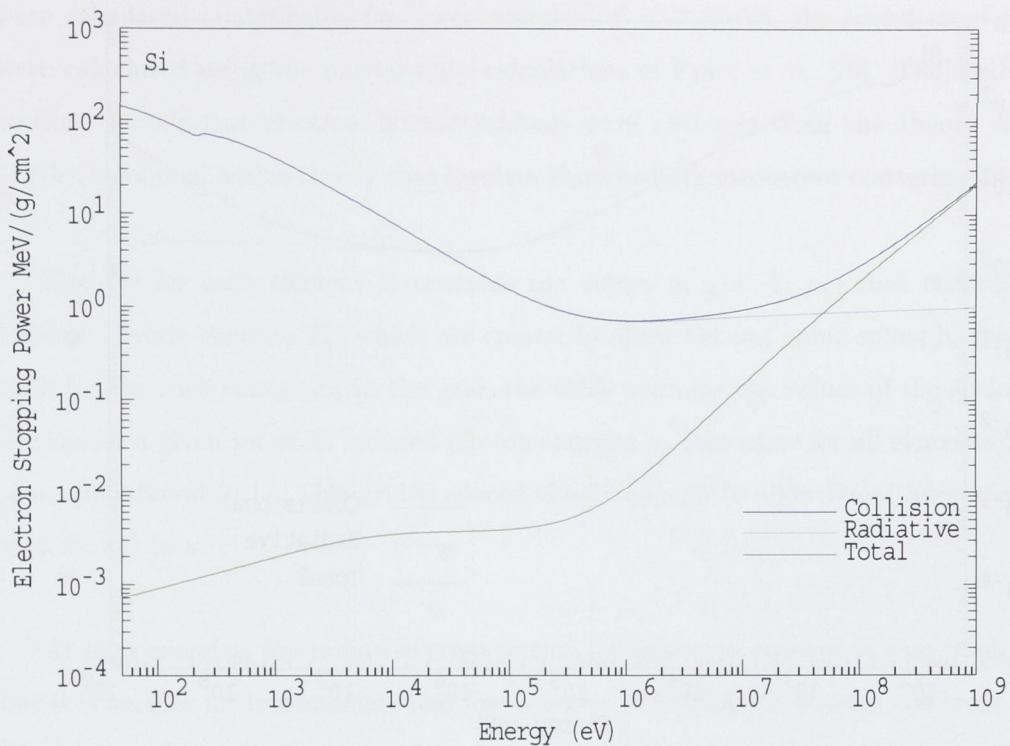


**Figure 3.7:** Radiative and collisional stopping powers of silicon for electrons [8]. The radiative or bremsstrahlung stopping power becomes dominant for high energy.

was developed by Bethe and Heitler [67], using Dirac's relativistic theory of the electron and Born's first approximation. The classical theory states that whenever a particle experiences an acceleration, it should radiate. In the quantum-mechanical theory, a plane wave representing the electron enters the nuclear field, is scattered, and has a small but finite chance of emitting a photon. The electron is acted on by both the atomic field and the emitted radiation field. Part or all of the electron (or positron) energy  $E$  is lost to the emission of the bremsstrahlung photon, which can take any fraction of the electron energy ( $0 < W < E$ ), where  $W$  is the energy of the bremsstrahlung photon. PENELOPE's cross section for bremsstrahlung is differential in terms of the energy loss  $W$ , and is derived from that of Bethe and Heitler [67, 68], which was based on the Born approximation, which takes the initial and final electronic wave functions as plane-waves, and the actions of the atomic field and emitted radiation field as a perturbation. This holds only when the electron energy before and after the collision is much larger than  $m_e c^2$ , the electronic rest mass.

The Bethe-Heitler cross section indicates that, for a given value of  $Z$ , the quantity  $W d\sigma_{br}/dW$  varies smoothly with  $E$  and  $W$ . PENELOPE follows the convention of ex-

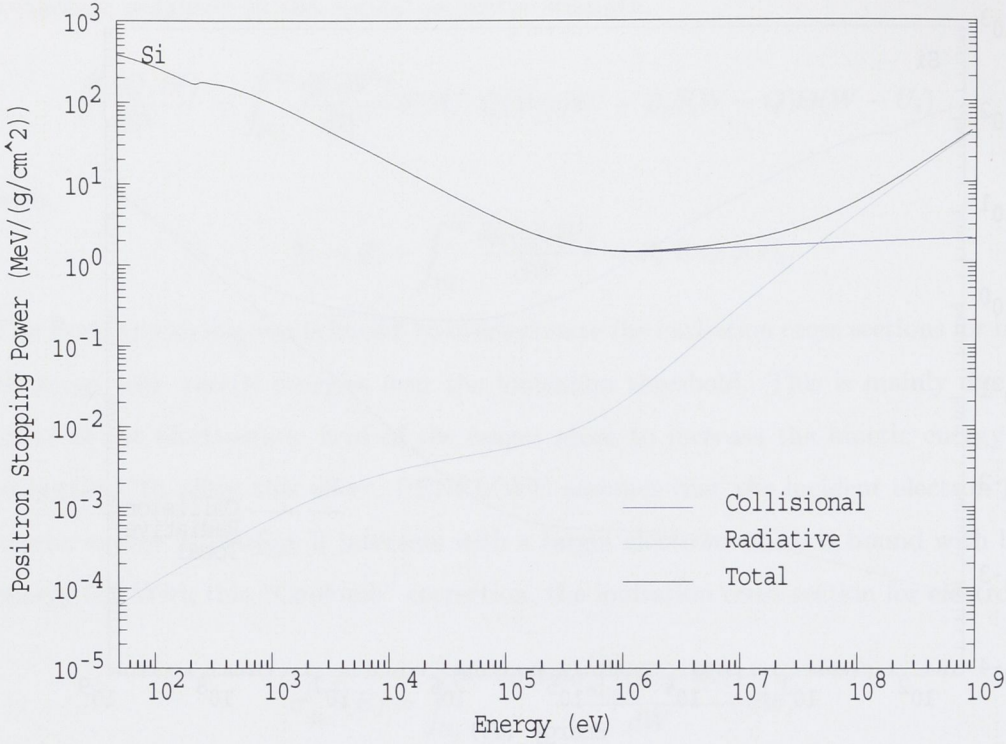


**Figure 3.8:** Radiative and collisional stopping powers of silicon for positrons [8]. The radiative or bremsstrahlung stopping power becomes dominant for high energy.

pressing the cross section for bremsstrahlung in the form:

$$\frac{d\sigma_{br}}{dW} = \frac{Z^2}{\beta^2} \frac{1}{W} \chi(Z, E, \kappa), \quad (3.41)$$

where  $W$  is the energy of the emitted photon and  $\kappa$  is the reduced photon energy, defined as

$$\kappa \equiv W/E, \quad (3.42)$$

which takes values between 0 and 1. The quantity

$$\chi(Z, E, \kappa) = (\beta^2/Z^2) W \frac{d\sigma_{br}}{dW} \quad (3.43)$$

is known as the “scaled bremsstrahlung cross section” which, for a given element  $Z$ , varies smoothly with  $E$  and  $\kappa$ . PENELOPE uses a database of scaled cross sections obtained from those of Seltzer and Berger [69]. They separately calculated the bremsstrahlung cross sections due the screened field of the nucleus, and the sum of the two, the total scaled cross section. For high energies ( $E > 2$  MeV) the nucleus-electron cross sections

were calculated analytically, for lower energies ( $E < 2$  MeV), the scaled cross sections were calculated using the partial-wave calculations of Pratt *et al.* [70]. The scaled cross sections for electron-electron bremsstrahlung were obtained from the theory of Haug (1975), combined with a theory that involves Hartree-Fock incoherent scattering functions.

The file for each element  $Z$  contains the values of  $\chi(Z, E_i, \kappa_j)$  that correspond to electron kinetic energies  $E_i$ , which are spaced to allow natural cubic spline interpolation in  $\ln E$ . For each energy  $E_i$  in the grid, the table contains the values of the scaled cross section for a given set of 32 reduced photon energies  $\kappa_j$  (the same for all elements), which span the interval (0,1). This grid is spaced closely enough to allow linear interpolation of  $\chi(Z, E_i, \kappa_j)$  in  $\kappa$ .

At high energies, the radiative cross section for positrons reduces to that of electrons, but it is smaller for intermediate and low energies. PENELOPE obtains the cross section for positrons by multiplying the electron cross section by a  $\kappa$ -independent factor *i.e.*,

$$\frac{d\sigma_{br}^{(+)}}{dW} = F_p(Z, E) \frac{d\sigma_{br}^{(-)}}{dW} \quad (3.44)$$

The factor  $F_p(Z, E)$  is set equal to the ratio of the radiative stopping powers for positrons and electrons, as calculated by Kim *et al.* [71]. PENELOPE uses an analytical approximation for  $F_p$  in terms of the electron energy  $E$  and the atomic number  $Z$ .

The mean free path for emission of a photon of larger energy than a user defined cutoff  $W_{cr}$  is

$$\lambda_{br}^{-1}(E; W_{cr}) \equiv N \int_{W_{cr}}^E \frac{d\sigma_{br}}{dW} dW = N \frac{Z^2}{\beta^2} \int_{\kappa_{cr}}^1 \frac{1}{\kappa} \chi(Z, E, \kappa) d\kappa, \quad (3.45)$$

where  $\kappa_{cr} = W_{cr}/E$ . The radiative stopping power is

$$S_{br}(E) \equiv N \int_0^E W \frac{d\sigma_{br}}{dW} dW = N \frac{Z^2}{\beta^2} E \int_0^1 \chi(Z, E, \kappa) d\kappa. \quad (3.46)$$

The stopping powers are normalised to coincide with those of the ICRU Report 37 [8].

### Angular Distribution of Emitted Photons

The direction of the emitted bremsstrahlung photon is defined by the polar angle  $\theta$  and the azimuthal angle  $\phi$ . For isotropic media, the random orientation of the atoms and

molecules renders the bremsstrahlung cross section independent of  $\phi$

$$\frac{d^2\sigma_{br}}{dWd(\cos\theta)} = \frac{d\sigma_{br}}{dW} p_{br}(Z, E, \kappa; \cos\theta) = \frac{Z^2}{\beta^2} \frac{1}{W} \chi(Z, E, \kappa) p_{br}(Z, E, \kappa; \cos\theta), \quad (3.47)$$

where  $p_{br}(Z, E, \kappa; \cos\theta)$  is the probability distribution function of  $\cos\theta$ .

Numerical values of the “shape function”  $p_{br}(Z, E, \kappa; \cos\theta)$ , calculated by partial wave methods, have been published by Kissel *et al.* [72] for the cases:  $Z = 2, 8, 13, 47, 79, 92$ ;  $E = 1, 5, 10, 50, 100, 500$  keV and  $\kappa = 0, 0.6, 0.8, 0.95$ . PENELOPE samples the shape function from a semi empirical formula derived by Kirkpatrick and Wiedmann [73] Statham [74], modified to agree with the values given by Kissel *et al.* [72].

### 3.1.4 Positron Annihilation

All previously discussed collision mechanisms apply to the interactions of both positrons and electrons with matter. However, a positron traversing through matter, has the unique possibility to combine with an atomic electron and annihilate, giving up its kinetic energy and the rest mass of the positron and electron to two photons, called “annihilation radiation”. If both the positron and electron are at rest (in the laboratory system), the two photons will both have an energy of 511 keV. However, if the positron annihilates in flight *i.e.*, the kinetic energy  $E$  of the positron is larger than the “absorption” energy, the two photons may have different energies, say,  $E_-$  and  $E_+$ , which add to  $E + 2m_e c^2$ , where  $E_-$  refers to the photon of lower energy. Each annihilation event is then completely characterised by the quantity

$$\zeta \equiv \frac{E_-}{E + 2m_e c^2}. \quad (3.48)$$

Assuming that the positron moves initially in the direction of the  $z$ -axis, from conservation of energy and momentum it follows that the two photons are emitted in directions with polar angles [8]

$$\cos\theta_- = (\gamma^2 - 1)^{-1/2}(\gamma + 1 - 1/\zeta) \quad (3.49)$$

and

$$\cos\theta_+ = (\gamma^2 - 1)^{-1/2}[\gamma + 1 - 1/(1 - \zeta)], \quad (3.50)$$

and azimuthal angles  $\phi_-$  and  $\phi_+ = \phi_- + \pi$ . The quantity  $\gamma = 1 + E/(m_e c^2)$  is the total energy of the positron in units of its rest energy.

PENELOPE's treatment of positron annihilation is derived from that of Heitler [75], subsequently transformed by Nelson *et al.* [76] in to the laboratory system (where the electron is at rest), given by

$$\frac{d\sigma_{an}}{d\zeta} = \frac{\pi r_e^2}{(\gamma + 1)(\gamma^2 - 1)} [S(\zeta) + S(1 - \zeta)], \quad (3.51)$$

where

$$S(\zeta) = -(\gamma + 1)^2 + (\gamma^2 + 4\gamma + 1) \frac{1}{\zeta} - \frac{1}{\zeta^2}. \quad (3.52)$$

Again, axial symmetry of the target atom distribution makes the cross section independent of the azimuthal angle  $\phi_-$ , which is uniformly distributed on the interval  $(0, 2\pi)$ . For fast positrons, annihilation photons are emitted preferentially at forward directions. The angular distribution becomes more isotropical as the energy of the positron decreases.

### 3.1.5 Cross Sections

As figures 3.2-3.5 suggest, inelastic and elastic scattering are responsible for most of the energy loss and angular deflection suffered by low energy electrons and positrons interacting with matter. However figures 3.7 and 3.8 show that this is not the case above 1 MeV, where the radiative stopping power (due to bremsstrahlung events) begins to increase dramatically. This is due to an increase in the average energy per bremsstrahlung photon, rather than any increase in the cross section. As higher energy photons are more likely to escape from the detector crystal, this is likely to be important for electron detection.

## 3.2 PENELOPE Physics: Photons

As photons are the main source of background, PENELOPE's treatment of their interactions should be discussed. The fundamental interactions of photons with matter are (see figure 3.9):

- (a) Coherent (Rayleigh) scattering, where there is angular deflection, but no excitation

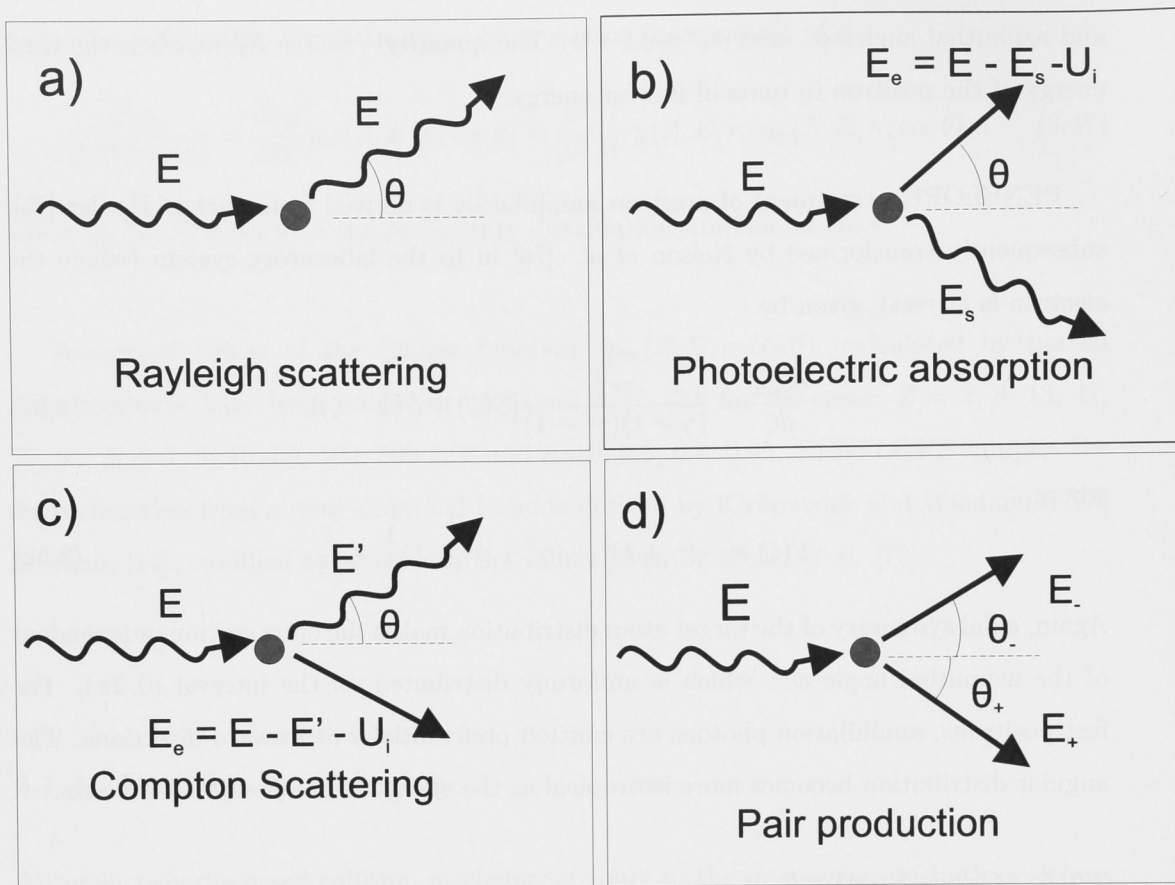


Figure 3.9: Interactions of photons with matter.

of the target atom or transfer of energy

- (b) Photoelectric absorption - dominant at low energy, below ( $\approx 0.1$  MeV) - describes the complete absorption of an incident photon and the emission of a bound electron
- (c) Compton scattering - dominant at high energies, above ( $\approx 0.1$  MeV) - and describes the absorption of the incident photon together with a scattered atomic electron
- (d) Pair production - only available for photons of  $E > 1.022$  MeV, a higher order process that describes the production of an electron-positron pair in the atomic field

### 3.2.1 Coherent (Rayleigh) Scattering

Rayleigh or coherent scattering is the scattering by bound atomic electrons without excitation of the target atom; necessarily then, the energies of the incident and scattered photon are the same. The term coherent is applied because the scattering arises from the interference between secondary electromagnetic waves, coming from different parts of the



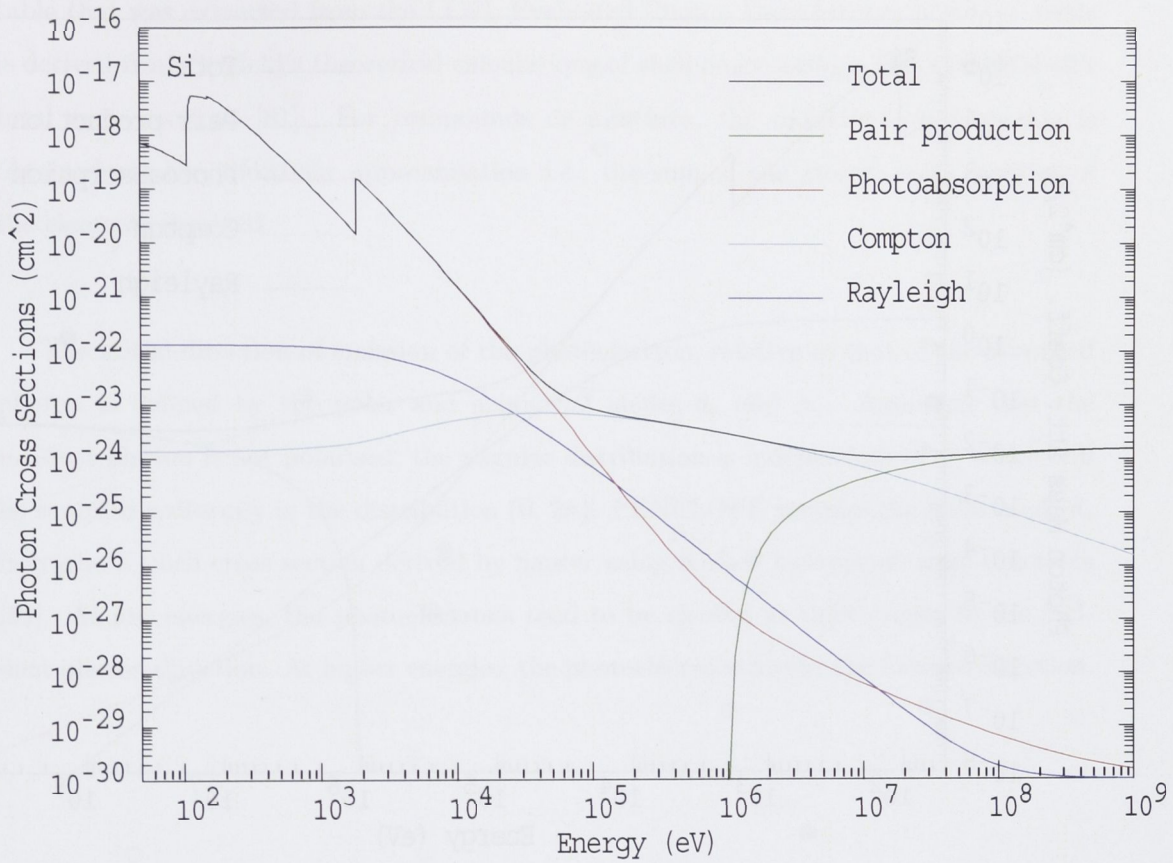


Figure 3.10: Photon interaction cross sections for silicon.

atomic charge distribution [8]. PENELOPE uses an atomic cross section per unit solid angle for coherent scattering based upon Born [77]

$$\frac{d\sigma_{Ra}}{d\Omega} = \frac{d\sigma_T}{d\Omega} [F(q, Z)]^2, \quad (3.53)$$

where

$$\frac{d\sigma_T(\theta)}{d\Omega} = r_e^2 \frac{1 + \cos^2 \theta}{2} \quad (3.54)$$

is the classical Thomson cross section for scattering by a free electron at rest,  $\theta$  is the polar scattering angle and  $F(q, Z)$  is the atomic form factor. The quantity  $r_e$  is the classical electron radius and  $q$  is the magnitude of the momentum transfer. The atomic form factor can be expressed as the Fourier transform of the atomic electron density  $\rho(r)$ . PENELOPE uses the analytical approximation of Baró *et al.* [78].

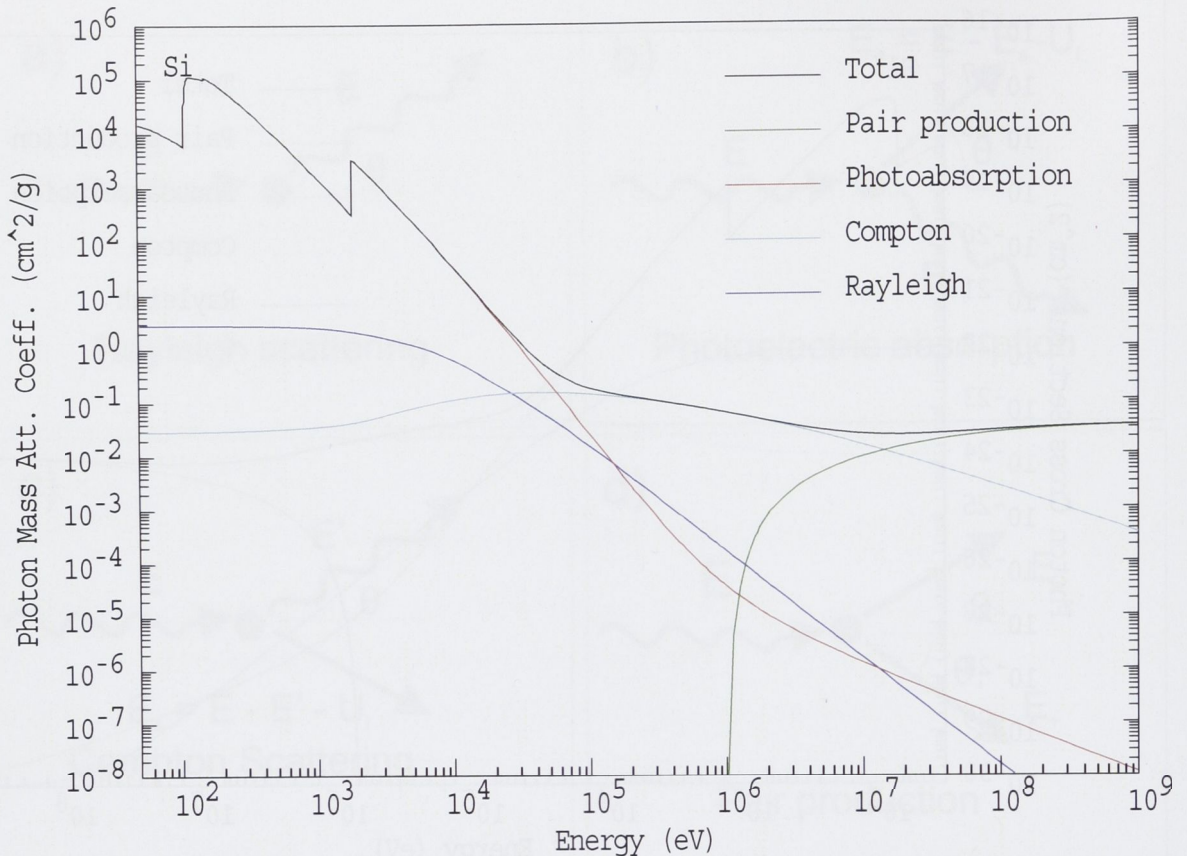


Figure 3.11: Photon mass attenuation coefficients for silicon.

### 3.2.2 Photoelectric Absorption

Photoelectric absorption is the dominant interaction mechanism for photon energies less than around 0.1 MeV. A photon, of energy  $E$  is entirely absorbed by an atom, which then ejects an atomic electron (photoelectron). Momentum is conserved by the recoil of the entire atom. The electron is emitted with an energy  $E_e = E - U_i$  where  $U_i$  is the binding energy of the state  $i$ . The remainder of the energy will appear as characteristic X-rays or Auger electrons, filling the vacancy in the inner shell. The transition is only allowed if the photon has an energy higher than that of the binding energy of the state, giving rise to the characteristic absorption edges seen on the photoelectric cross sections. To represent the atomic states, an independent electron model, such as the Dirac-Hartree-Fock-Slater self-consistent model, may be used. The ionisation energies used in PENELOPE are the empirical values given by Lederer and Shirley [79].

PENELOPE uses photoelectric cross sections obtained by interpolation in a numerical

table that was extracted from the LLNL Evaluated Photon Data Library [64]. The table is derived from Scofield's theoretical calculations of shell cross sections [80] and Hubbell's total cross sections [81]. For compounds or mixtures, the molecular cross section is obtained via the additivity approximation *i.e.*, the sum of the atomic cross sections of the elements involved.

The initial direction of emission of the photoelectron, relative to that of the absorbed photon is defined by the polar and azimuthal angles  $\theta_e$  and  $\phi_e$ . Assuming that the incident photon is not polarised, the angular distribution is independent of  $\phi$ , which will be sampled uniformly in the distribution  $(0, 2\pi)$ . PENELOPE samples the polar angle  $\theta_e$  from the K-shell cross section derived by Sauter using K-shell hydrogenic wave functions [59]. At low energies, the photoelectrons tend to be ejected at right angles to the incident photon direction. At higher energies, the photoelectrons favour the forward direction.

### 3.2.3 Incoherent (Compton) Scattering

The scattering of very low energy photons ( $h\nu \ll m_0c^2$ ) by free electrons is described adequately by the non-relativistic classical theory of J.J. Thomson [82]. This breaks down as  $h\nu$  approaches  $m_0c^2$ , and the photon momentum cannot be discounted. Compton scattering arises in this regime, and becomes dominant for medium - high energies  $E > 0.1$  MeV. For this reason, a relatively detailed summary of the physics is included here. Compton scattering is the process where, an incident photon of energy  $E$  is absorbed by an atom, and then re-emitted with a reduced energy  $E'$ , in the direction  $\Omega = (\theta, \phi)$  relative to the direction of the incident photon, and an atomic electron is emitted with energy  $E_e = E - E' - U_i > 0$ . The quantity  $U_i$  is the binding energy of the considered shell, and the residual atom is left with a vacancy in the  $i$ -th shell.

PENELOPE simulates Compton scattering via a cross section adapted from the Klein-Nishina formula,

$$\frac{d\sigma_{Co}^{KN}}{d\Omega} = \frac{r_e^2}{2} \left( \frac{E_C}{E} \right)^2 \left( \frac{E_C}{E} + \frac{E}{E_C} - \sin^2 \theta \right), \quad (3.55)$$

where

$$E' \equiv \frac{E}{1 + \kappa(1 - \cos \theta)} \equiv E_C, \quad (3.56)$$

$$\kappa = E/m_e c^2. \quad (3.57)$$

This simple cross section, as it is, assumes that the bound electrons are initially at rest - thereby neglecting Doppler broadening of the scattered quanta. Moreover, it neglects the fact that the transition is only allowed if the energy transfer  $E - E'$  is larger than the ionisation energy  $U_i$  of the active shell. The impulse approximation favoured by PENELOPE essentially applies a Lorentz transformation with velocity  $\mathbf{v}$  equal to that of the moving target atom, and averaging over the momentum distribution  $\rho_i(\mathbf{p}) \equiv |\psi_i(\mathbf{p})|^2$ , where  $\psi_i(\mathbf{p})$  is the wave function in the momentum representation.

For the present purpose, though, most of the important results can be obtained simply by conserving energy and momentum:

### 1. The Compton shift

$$\frac{c}{\nu'} - \frac{c}{\nu} = \lambda' - \lambda = \frac{\hbar}{m_0 c} (1 - \cos \theta) \quad (3.58)$$

where  $\nu'$  and  $\nu$  are the frequencies of the scattered and incident photons respectively;  $\lambda'$  and  $\lambda$  are the wavelengths of the scattered and incident photons.

### 2. Energy of the scattered quantum

$$h\nu' = \frac{m_0 c^2}{1 - \cos \theta + (1/\kappa)}, \quad (3.59)$$

$$\frac{\nu'}{\nu} = \frac{1}{a + \kappa(1 - \cos \theta)}. \quad (3.60)$$

Note that for very large incident photon energy,  $\kappa \gg 1$ , the energy of the backscattered photon approaches  $m_e c^2/2 = 0.25$  MeV at  $\theta = 180^\circ$ , while the energy of photons scattered at  $\theta = 90^\circ$  approaches  $m_e c^2 = 0.51$  MeV.

### 3. Energy of the emitted electron

$$E_e = \hbar\nu \frac{\kappa(1 - \cos \theta)}{1 + \kappa(1 - \cos \theta)} \quad (3.61)$$

4. The maximum energy transfer  $E_e^{(max)}$

$$E_e^{(max)} = \frac{\hbar\nu}{1 + (1/2\kappa)}, \quad (3.62)$$

$$E = 1/2E_e^{(max)} \left( 1 + \sqrt{1 + \frac{2m_e c^2}{E_e^{(max)}}} \right). \quad (3.63)$$

Equation 3.62 can often be seen in conversion-electron spectra as the familiar “Compton edge” seen in CE spectra as a sharp drop in the background.

### 3.2.4 Electron - Positron Pair Production

Photons with energies,  $E$ , above  $2m_e c^2$  may interact with matter via a fourth mechanism, whereby the photon is completely absorbed, and in its place an electron positron pair is created with *total* energy equal to  $E$ :

$$E = (E_{e^-} + m_e c^2) + (E_{e^+} + m_e c^2) \quad (3.64)$$

where  $E_{e^-}$  and  $E_{e^+}$  are the kinetic energies of the electron and positron respectively. The process can only take place in the electromagnetic field of the nucleus or an electron, with the target particle absorbing momentum and energy so as to conserve both quantities. The threshold energy for pair production in the field of the nucleus is  $2m_e c^2 = 1.022$  MeV. The threshold for pair production in the field of an electron is, if the electron is at rest,  $4m_e c^2 = 2.044$  MeV.

### 3.2.5 Attenuation Coefficients

In terms of energy loss per unit thickness, the photoelectric effect is dominant below about 0.1 MeV. Above around 10 MeV pair production becomes dominant, and in the interim region, Compton absorption is dominant.

## 3.3 Monte Carlo Simulations

The following discussion, based heavily on the PENELOPE manual, reviews the relevant aspects of the Monte Carlo techniques as implemented in PENELOPE.

Monte Carlo simulations originated in the Los Alamos National Laboratory in the 1940s. It has become accepted as reliable for the simulation of radiation transport

[83, 84]. Monte Carlo delivers the same information as the Boltzmann transport equation, with the same interaction model, but is easier to implement [85]. In fact, the Boltzmann equation is difficult to solve for even the simplest geometries *e.g.*, thin foils, however complex geometries *e.g.*, detector geometries, are dealt with easily by Monte Carlo simulations. The main drawback is that the results are subject to statistical fluctuation and uncertainties. However, these can be estimated and reduced by increasing simulation time.

Detailed Monte Carlo simulation follows an incident particle (primary particle) until it stops. The entire chain of events is labeled a “history”. This, together with the histories of all the daughter secondary radiations created is labeled a “shower”. The initial energy is shared among the primary and secondary radiations, thus the initial energy of the primary particle is completely contained within its shower. A history consists of a set of free flights, separated by a series of events, where the particle may lose energy, change direction, or create secondary radiation. The “time” and place of each event, along with the type of interaction at each event, is determined by random sampling of the set of cross sections for each interaction.

To visualise the cross section, take the example of a single interaction mechanism, where both a change in direction and energy loss occur, *e.g.*, inelastic scattering of electrons. Consider a monoenergetic beam of electrons with energy  $E$  and direction of movement  $\hat{d}$  impinges on a target atom or molecule  $T$ , which is located at the origin of the reference frame. Assume that the beam is laterally homogeneous, and that its lateral extension is much larger than that of the target atom. The beam is characterised by its current density  $\mathbf{J}_{inc}^3$ . In an interaction, the particle loses energy  $W$ , and is deflected. Suppose a detector, placed some distance from the origin in the direction  $(\theta, \phi)$ , and covering a small solid angle  $d\Omega$  detects and counts all particles that enter its sensitive volume with energy in the interval  $(E - W - dW, E - W)$  (*i.e.*, particles that have lost an energy between  $W$  and  $W + dW$ ). Let  $N_{count}$  denote the number of counts per unit time. The double-differential cross section (per unit solid angle and unit energy loss) is defined by

$$\frac{d^2\sigma}{d\Omega dW} \equiv \frac{N_{count}}{|\mathbf{J}_{inc}| d\Omega dW}. \quad (3.65)$$

The cross section has the dimensions of area/(solid angle  $\times$  energy); the product  $[d^2\sigma(d\Omega dW)] \times d\Omega dW$  represents the area of a plane surface that, placed perpendicularly

to the incident beam, is hit by as many projectiles as are scattered into directions  $\mathbf{d}'$  within  $d\Omega$  with energy loss between  $W$  and  $W + dW$ .

The energy-loss cross section, differential in only the energy loss is obtained by integrating the double-differential cross section over directions,

$$\frac{d\sigma}{dW} \equiv \int \frac{d^2\sigma}{d\Omega dW} d\Omega. \quad (3.66)$$

The total cross section  $\sigma$  is defined as the integral of the energy-loss cross section over the energy loss,

$$\sigma \equiv \int_0^E \frac{d\sigma}{dW} dW = \int_0^e \left( \int \frac{d^2\sigma}{d\Omega dW} d\Omega \right) dW. \quad (3.67)$$

A molecule or atom may be replaced by a sphere of radius  $r_s$  such that the cross sectional area  $\pi r_s^2$  equals the total cross section  $\sigma_T$ . Consider a foil of small thickness  $ds$ . If there are  $N$  molecules over unit volume, and the current density  $J$ , then the number of incident particles that will interact per unit time and unit volume is  $dJ = JN\sigma ds$ . Therefore, the probability of interaction per unit path length is

$$\frac{dJ}{J} \frac{1}{ds} = N\sigma. \quad (3.68)$$

The probability of interaction as a function of path length  $s$  is

$$p(s) = N\sigma \exp[-s(N\sigma)]. \quad (3.69)$$

The mean free path  $\lambda$  is defined as the average path length between collisions:

$$\lambda \equiv \langle s \rangle = \int_0^\infty sp(s)ds = \frac{1}{N\sigma}. \quad (3.70)$$

Its inverse,

$$\lambda^{-1} = N\sigma \quad (3.71)$$

is the interaction probability per unit path length.

Consider now that there are two independent collision mechanisms, "A" and "B", which could represent, for example, inelastic and elastic scattering. The mechanisms are

completely specified by their corresponding cross sections

$$\frac{d^2\sigma_A(E; \theta, W)}{d\Omega dW} \text{ and } \frac{d^2\sigma_B(E; \theta, W)}{d\Omega dW}, \quad (3.72)$$

where  $d\Omega$  is a solid angle element in the direction  $(\theta, \phi)$ . Assuming that the molecules/atoms that make up the target material are oriented at random, the cross sections are independent of the azimuthal angle. The total cross sections (per molecule) for mechanisms A and B are

$$\sigma_{A,B}(E) = \int_0^E dW \int_0^\pi 2\pi \frac{d^2\sigma_{A,B}(E; \theta, W)}{d\Omega dW} \sin \theta d\theta. \quad (3.73)$$

The total interaction cross section is

$$\sigma_T(E) = \sigma_A(E) + \sigma_B(E). \quad (3.74)$$

The interaction probability per unit path length is

$$\lambda_T^{-1} = N\sigma_T. \quad (3.75)$$

Notice that the total inverse mean free path is the sum of the inverse mean free paths of the different interaction mechanisms,

$$\lambda_T^{-1} = \lambda_A^{-1} + \lambda_B^{-1}. \quad (3.76)$$

The probability distribution function of the path length  $s$  of a particle from its current position to the site of the next collision is

$$p(s) = \lambda_T^{-1} \exp(-s/\lambda_T). \quad (3.77)$$

The probabilities that the interaction will be of type "A" or "B" are:

$$p_A = \sigma_A/\sigma_T \text{ and } p_B = \sigma_B/\sigma_T. \quad (3.78)$$

The probability distribution functions of the polar scattering angle and the energy loss in



individual scattering events are

$$p_{A,B}(E; \theta, W) = \frac{2\pi \sin \theta}{\sigma_{A,B}(E)} \frac{d^2 \sigma_{A,B}(E; \theta, W)}{d\Omega dW}. \quad (3.79)$$

Here  $p_A(E; \theta, W)d\theta dW$  gives the normalised probability that, in a scattering event of type A, the particle loses energy in the interval  $(W, W + dW)$  and is deflected into directions with polar angle in the interval  $(\theta, \theta + d\theta)$ . The azimuthal scattering angle is uniformly sampled in the interval  $(0, 2\pi)$ , *i.e.*,

$$p(\phi) = \frac{1}{2\pi}. \quad (3.80)$$

PENELOPE advances the particle to the next interaction by sampling the total mean free path  $\lambda_T$ . It will then randomly sample the interaction mechanisms based upon the total cross sections  $\sigma_A$ ,  $\sigma_B$ , which give the point-probabilities,  $p_A$  and  $p_B$ . The energy loss  $W$  and/or angular deflection is/are sampled from the energy loss cross section and/or the angular deflection cross section respectively. The process is then repeated until the particle is stopped (has energy below the energy cutoff) or exits the entire detector geometry.

### 3.3.1 Mixed Simulation

Up until now, the process described is the detailed simulation of events. The user specifies six angular and energy cutoffs for various interaction mechanisms. If the angular deflection *and* energy loss are below the user specified cut-off values, the interaction is called a *soft* event, and is simulated by collective simulation, using a continuous slowing down approximation, and an average energy loss. Interactions with a higher energy or angular change are simulated by detailed simulation, as outlined above. As the changes in energy and angle caused by the soft events in between hard events affects the hard interaction, a linear dependence on energy is assumed for those events. This approach is called mixed simulation (or class II simulation). It is necessary due to the increasingly large numbers of small energy loss collisions that occur toward the end of a particle's flight, when it has low energy. The approach is validated by the Markovian nature of particle transport [8].

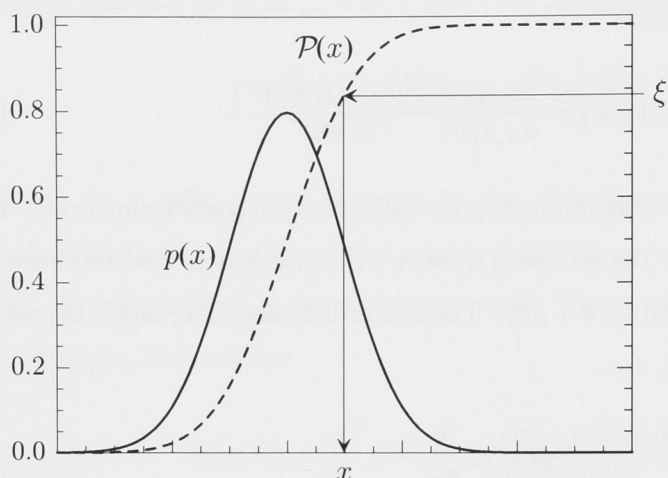


**Figure 3.12:** Random sampling from a distribution  $p(x)$  using the inverse-transform method.

### 3.3.2 Sampling Methods

Monte Carlo methods generate random variables by numerical transformations of random numbers. This allows random variables with probability distribution functions to be sampled. Random numbers  $\xi$  are generated uniformly over the interval  $(0,1)$ , which then must be transformed to the required probability distribution function. The randomness of the Monte Carlo method suits nuclear disintegration, as no two experiments will produce exactly the same results.

### 3.3.3 Inverse-Transform Method

PENELOPE uses the inverse transform method for random sampling of discrete variables, see figure 3.12 [8]. PENELOPE also uses the inverse-transform method for sampling continuous distributions  $p(x)$ . This is done by evaluating the function  $P(x)$  at the points  $x_i$  of a certain grid. The sampling equation  $P(x) = \xi$  can then be solved by inverse interpolation *i.e.*, by interpolating in the table  $(\xi_i, x_i)$ , where  $\xi_i \equiv P(x_i)$ .

### Rejection Methods

Another sampling method used by PENELOPE consists of sampling a distribution different to  $p(x)$  and subjecting it to a random test to determine whether it will be accepted or rejected. This method is applicable to any probability distribution function.

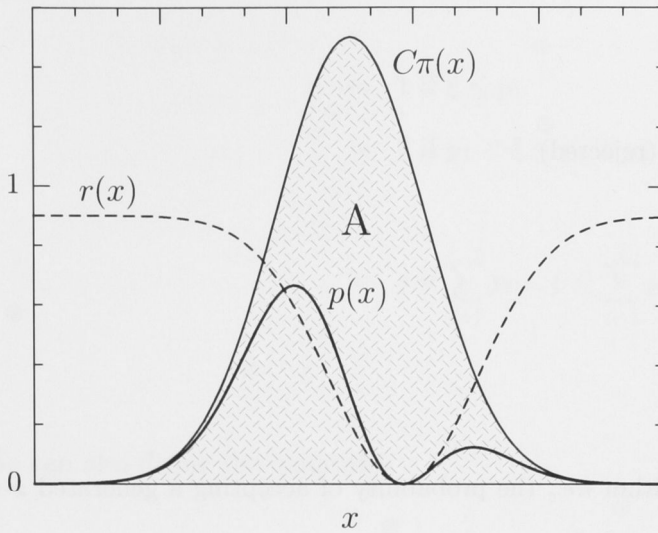


**Figure 3.13:** Random sampling from a distribution  $p(x)$  using rejection methods.

These methods can be understood using simple graphical arguments, see figure 3.13. Consider that, by means of the inverse transform method, random values of  $x$  are generated from a probability distribution function  $\pi(x)$ . For each sampled value of  $x$  we sample a random value  $y$  uniformly distributed in the interval  $(0, C\pi(x))$ , where  $C$  is a positive constant. The function  $C\pi(x)$  must be greater than  $p(x)$  for some value  $C > 0$ . The points  $(x, y)$  are randomly generated to be uniformly distributed over the region  $A$  of the plane limited by the  $x$ -axis and the curve  $y = C\pi(x)$ . The points with  $y > p(x)$  are rejected and the accepted ones (with  $y \leq p(x)$ ) are uniformly distributed in the region between the  $x$ -axis and the curve  $y = p(x)$  and hence, their  $x$ -coordinate is distributed according to  $p(x)$ .

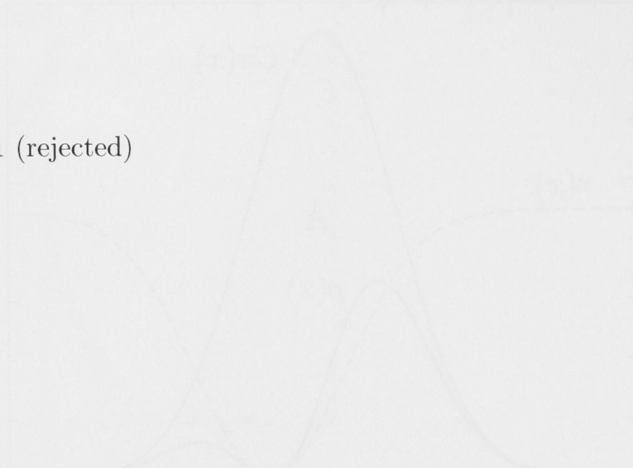
This method can be summarised by representing the probability distribution function  $p(x)$  as

$$p(x) = C\pi(x)r(x) \quad (3.81)$$

where  $\pi(x)$  is a probability distribution function that is sampled using the inverse transform method,  $C$  is a positive constant and the function  $r(x)$  satisfies the conditions  $0 \leq r(x) \leq 1$ . The rejection algorithm can be summarised as follows

1. Generate a random value  $x$  from  $\pi(x)$

2. Generate a random number  $\xi$
3. If  $\xi > r(x)$ , go to step 1 (rejected)
4. Deliver  $x$  (accepted)



The efficiency of the algorithm *i.e.*, the probability of accepting a generated  $x$ -value, is

$$\epsilon = \int_a^b r(x)\pi(x)dx = \frac{1}{C} \quad (3.82)$$

Graphically, the efficiency is the ratio of the areas under the curves  $y = p(x)$  and  $y = C\pi(x)$ , which are 1 and  $C$ , respectively. For a given  $\pi(x)$ , since  $r(x) \leq 1$ , the constant  $C$  must satisfy the condition  $C\pi(x) \geq p(x)$  for all  $x$ . The minimum value of  $C$ , with the requirement that  $C\pi(x) = p(x)$  for some  $x$ , gives the optimum efficiency.

The generation of the energy values is non-trivial. In PENELOPE, a given photon or electron line must be chosen from the lines specified in the input file, with a probability that corresponds to the relative intensities of the lines. If the random variable  $x$  can take the values  $x = 1, \dots, N$  with point probabilities  $p_1, \dots, p_N$ , respectively, the corresponding probability distribution function can be expressed as

$$p(x) = \sum_{i=1}^N p_i \delta(x - i), \quad (3.83)$$

where  $\delta(x)$  is the Dirac distribution. Here  $p(x)$  is assumed to be defined for  $x$  in an interval  $(x_{min}, x_{max})$  with  $x_{min} < 1$  and  $x_{max} > N$ . The corresponding cumulative distribution function is

$$P(x) = \begin{cases} 0 & \text{if } x < 1, \\ \sum_{i=1}^{[x]} p_i & \text{if } 1 \leq x \leq N, \\ 1 & \text{if } x > N, \end{cases} \quad (3.84)$$

where  $[x]$  stands for the integer part of  $x$ . Then, equation 3.84 leads to the sampling

formula

$$\begin{aligned}
 x &= 1 \text{ if } \xi \leq p_1 \\
 &= 2 \text{ if } p_1 < \xi \leq p_1 + p_2 \\
 &\vdots \\
 &= j \text{ if } \sum_{i=1}^{j-1} p_i < \xi \leq \sum_{i=1}^j p_i \\
 &\vdots
 \end{aligned} \tag{3.85}$$

We can also define the quantities

$$P_1 = 0, \quad P_2 = p_1, \quad P_3 = p_1 + p_2, \dots, \quad P_{N+1} = \sum_{i=1}^N p_i = 1 \tag{3.86}$$

To sample the function  $x$  randomly, a random number  $\xi$  is generated and set  $x$  equal to the index  $i$  such that

$$P_i < \xi \leq P_{i+1}. \tag{3.87}$$

### 3.4 The Input Files for PENELOPE

The user must provide three files for a PENELOPE simulation: a geometry file, an input file, and a material data file. The user can trivially generate the material data file by specifying the materials involved in the simulation in a subroutine. PENELOPE will then produce detailed cross sections, mean free paths, *etc.*, generally using cubic-spline interpolation, in energy and angle, on the values in its database. The geometry and input files are non-trivial to generate, and are summarised below.

#### 3.4.1 Geometry

The strength of the Monte Carlo method is its ability to handle complex geometries. Each simulation requires a user-specified geometry file, which is non-trivial to generate. PENELOPE uses a “constructive quadric geometry” system, which allows for the reproduction of very complex geometries. PENELOPE defines a geometry in terms of three entities (see appendix A):

- **Quadric surfaces** These surfaces define the intersection between materials. Each

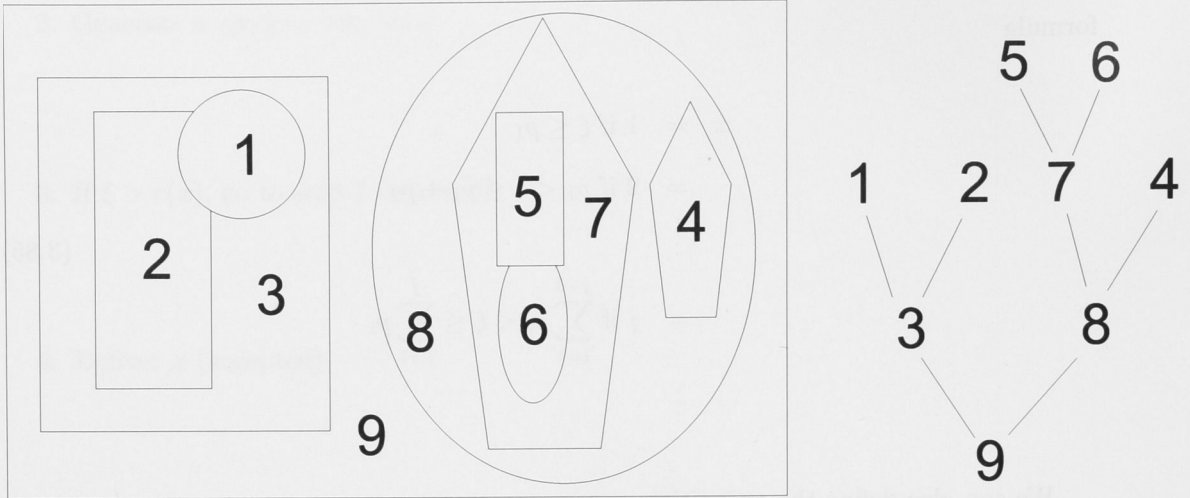


**Figure 3.14:** A possible cross section of a PENELOPE geometry and module, with geometry family tree.

surface is defined by the implicit equation

$$F(x, y, z) = A_{xx}x^2 + A_{xy}xy + A_{xz}xz + A_{yy}y^2 + A_{yz}yz + A_{zz}z^2 + A_x x + A_y y + A_z z + A_0 = 0, \quad (3.88)$$

which allows for the formation of planes, pairs of planes, spheres, cylinders, cones, ellipsoids paraboloids, hyperboloids, etc. Intersections of surfaces can be found simply by solving a quadratic. In practice, the surface is defined by an equivalent system, based on a reduced quadric of the form:

$$F_r(x, y, z) = I_1 x^2 + I_2 y^2 + I_3 z^2 + I_4 z + I_5 = 0, \quad (3.89)$$

where the indices  $I_1$  to  $I_5$ , which can take the values -1, 0 or 1, determine the “shape” of the surface - plane, sphere, etc. Three transformations are then applied to the basic reduced quadric equation of equation 3.89:

1. A *scaling* along the  $x$ ,  $y$ , and  $z$  axes. The reduced quadric of equation 3.89 can be re-written as

$$F_s(x, y, z) = I_1 \left(\frac{x}{a}\right)^2 + I_2 \left(\frac{y}{b}\right)^2 + I_3 \left(\frac{z}{c}\right)^2 + I_4 \frac{z}{c} + I_5 = 0, \quad (3.90)$$

where the coefficients  $a$ ,  $b$ , and  $c$  can be defined arbitrarily. The coefficients  $a$ ,  $b$  and  $c$ , scale the shape in the  $x$ ,  $y$ , and  $z$  planes, respectively.

2. A *rotation*  $R(\omega, \theta, \phi)$  defined by the Euler angles,  $\omega$ ,  $\theta$  and  $\phi$ , which define

right-handed rotations about the  $z$ -axis,  $y$ -axis and  $x$ -axis, respectively. The  $\omega$  rotation is applied first, followed by  $\theta$ , then the  $\phi$  rotation.

3. A *translation*, defined by components  $t_x$ ,  $t_y$  and  $t_z$  which define shifts in the  $x$ ,  $y$  and  $z$  directions, respectively.
- **Bodies** define a connected volume filled with a homogeneous material. They are specified by their limiting surfaces (which must be defined earlier), and their composition - a number that refers to a material in the material data file. Each limiting surface specifying a boundary of the body must be followed by a *side pointer*, which can take values of either -1 or +1, to specify on which side of the surface the body lies. A side pointer of -1 specifies that a point with coordinates  $(x_0, y_0, z_0)$  is said to be inside the surface if  $F(x_0, y_0, z_0) \leq 0$ ; whereas a side pointer of +1, specifies that a point with coordinates  $(x_0, y_0, z_0)$  is said to be inside the surface if  $F(x_0, y_0, z_0) \geq 0$ .
  - A **Module** is a connected volume, defined by limiting surfaces that contains one or more bodies. Essentially, it is a body that contains other bodies. Modules may also contain other modules, called *submodules*. The purpose of the extra structure is to speed up the process of checking whether the particle has crossed an interface between bodies. Part of the geometry routine is a subroutine called LOCATE, that “locates” a point  $\mathbf{r}$ , *i.e.*, determines the body that contains it, if any. The brute-force method would be to compute the side pointers for *all* surfaces and then check each body one by one, until one that fits all the side pointers is found. Another method may be to disregard those bodies that cannot be reached in a single step, but this was deemed undesirable from a computational point of view, as it requires extra information to be supplied to the routine. Figure 3.14 illustrates a possible structure of modules, submodules and bodies. Consider a particle at a point  $\mathbf{r}$  in module 9. After stepping the particle through to the next interaction, the subroutine LOCATE must determine whether it has crossed into another body. Instead of checking all bodies, the program will check whether it has strayed into modules 3 or 8. If it has crossed an interface, say into module 3, the program will then only check the bodies 1, 2 and 3 for the location of the particle.

### 3.4.2 Input File

A user generated input file specifies the source position and emissions, the energy detectors, and the simulation parameters, see appendix B. Each radiation is specified by

its energy in eV and its intensity (relative to the other radiations). The coordinates and throwing angle of the source is specified. Each detector must be specified by its body number in the geometry file. The energy window *i.e.* the minimum and maximum energies and the number of energy bins must be specified for each detector. The length of the simulation can be set by either the simulation time, or the number of desired particle histories.

### Simulation Parameters

The electron tracking is controlled by 6 user specified parameters.  $E_{abs}$  gives the absorption energy below which the particle is considered to have stopped.  $E_{abs}$  should be smaller than the width of the energy bins used.  $C1$  and  $C2$  refer to elastic collisions, and have a very weak influence on the results [8].  $C1$  gives the average angular deflection due to a hard collision and to the soft collisions previous to it.  $C2$  represents the maximum value permitted for the average fractional energy loss in a step. On the other hand,  $W_{cc}$  and  $W_{cr}$  are energy cutoffs to distinguish hard and soft events.  $W_{cc}$  and  $W_{cr}$  should be chosen so that they are smaller than the energy bins used. The maximum step size can be controlled with the parameter  $s_{max}$ . The maximum step length is important for thin bodies, and the PENELOPE manual specifies that it should be set to less than one-tenth of the body thickness. For thick bodies, such as the detector casing,  $s_{max}$  is unimportant and can be left unspecified, where the program will take the default value of  $1 \times 10^{11}$  cm.



---

# Results

---

For electrons in the energy range of interest, there is little literature that compares PENELOPE simulations to experiment. Presented in this chapter are several simulations using the Monte Carlo program PENELOPE, designed for direct and comprehensive comparison to the experimental results, presented in chapter 2. It will be shown that the simulations provide additional information to the experiments, and that the two together effectively chart the response of the Si(Li) detector from 10 keV to 3.5 MeV in energy, and from  $0^\circ$  to  $60^\circ$  in angle of incidence.

## 4.1 Experimental Setup for the $^{133}\text{Ba}$ Monte Carlo Measurement, with the Honey Detector as Specified by the Manufacturer

The experimental details and experimental photon and electron spectra of a  $^{133}\text{Ba}$  source were presented in chapter 2. The experimental setup was recreated in PENELOPE, and the setup and simulated spectra are presented here. The aim was to reproduce the entire energy spectrum in PENELOPE, including detector efficiencies, background and lineshape, as verification of the code's accuracy and suitability for electron-spectroscopy calibration.

The most crucial aspects of the  $^{133}\text{Ba}$  experiment were reproduced in the simulation inputs, these being:

- (i) The detector geometry, see figures 4.1 and 4.2, of appendix A, including casing, gold front window, and the position and thickness of the source (the pixelation of the figures is a result of the graphics program used, and is not present in the simulation)



**Figure 4.1:** Honey - front view, produced in PENELOPE, see appendix A.



**Figure 4.2:** Honey - cross sectional view, produced in PENELOPE, see appendix A.

- 
- (ii) The spatial distribution of the source - the source distribution was sampled uniformly from a cylindrical distribution with diameter and thickness matching those of the radioactive source used in the experiment
  - (iii) Radiation intensities and energies were sampled according to the relative intensities and energies specified in table 2.1
  - (iv) The effect of charge collection and electronic noise (see section 2.3.1)

While the physics in the PENELOPE source code was left unchanged, some modifications to the program were necessary to reproduce the experimental conditions, notably (ii) and (iv), the source distribution and the effects of statistical charge collection:

- The PENELOPE source code only allows a point source distribution. This is problematic, as electrons that are ejected from some depth in the source may lose part of their energy to the bulk material of the source, causing an energy straggling tail, see section 2.3.2. Leaving this out of the simulations would give an incorrect lineshape. A routine to uniformly sample a cylindrical source distribution was incorporated into the PENELOPE code. The radius and thickness of the source must be specified in the PENELOPE input file.
- As there is no provision in PENELOPE for electronic noise, and peak broadening due to charge collection effects, a modification was made to “mimic” the effects that these have on the spectrum. Once PENELOPE has determined the energy a particle leaves in the detector, the program randomly samples a Gaussian distribution centred around that energy. The width of the Gaussian is specified in the input file and was fixed at a constant value of 2 keV, chosen to match those found by fitting the experimental spectrum.
- A modification was made that allows the user to set the desired number of energy channels to their choosing - originally there was a 400 channel maximum, which was too coarse to see the fine details of the spectrum. The modification allowed the user to set the number of channels to a maximum of 4000, which is appropriate for the experiments performed here.
- It was noticed that the program defaults to using the same seed for the random number generator every time, meaning that running twice with identical setups will produce identical results. For this reason, a program that generates the seed based

on the time and date was implemented [86]. This is called once at the start of the run, and then the PENELOPE random number generator is used from then on.

#### 4.1.1 Geometry

The Honey detector array, including crystal and casing dimensions, as well as gaps and electrodes, were constructed from elementary quadratic surfaces, as described in section 3.4.1. The electrical connections on the back were left out, as well as the cold finger, as they are unlikely to affect the energy signal. The detector chamber was also omitted - there is the possibility that electrons will backscatter off the detector chamber and hit the detector, however, incorporating this would slow simulation speed considerably, and most likely not affect the simulation results in a significant way.

#### 4.1.2 Simulation Parameters

Material	$E_{abs,\gamma}$ (keV)	$E_{abs,e^-}$ (keV)	C1	C2	$W_{cc}$ (keV)	$W_{cr}$ (keV)	$s_{max}$ (cm)
Active Silicon	1	0.1	0.1	0.1	0.1	0.1	$1 \times 10^{-3}$
Gold Window	1	0.1	0.1	0.1	0.1	0.1	$1 \times 10^{-8}$
Copper Casing	10	1	0.1	0.1	1	1	$1 \times 10^{11}$

**Table 4.1:** Simulation parameters.

The simulation parameters, described in section 3.4.2 are set separately for each material. Simulation parameters were chosen so as to provide precision for the detector materials (silicon and gold) and were left quite coarse for the detector casing, see table 4.1. The radiations were emitted in a cone of half angle  $18.2^\circ$ , sufficient to irradiate the entire area of the detector, with 45 bins for the polar angle and 18 bins for the azimuthal angle.

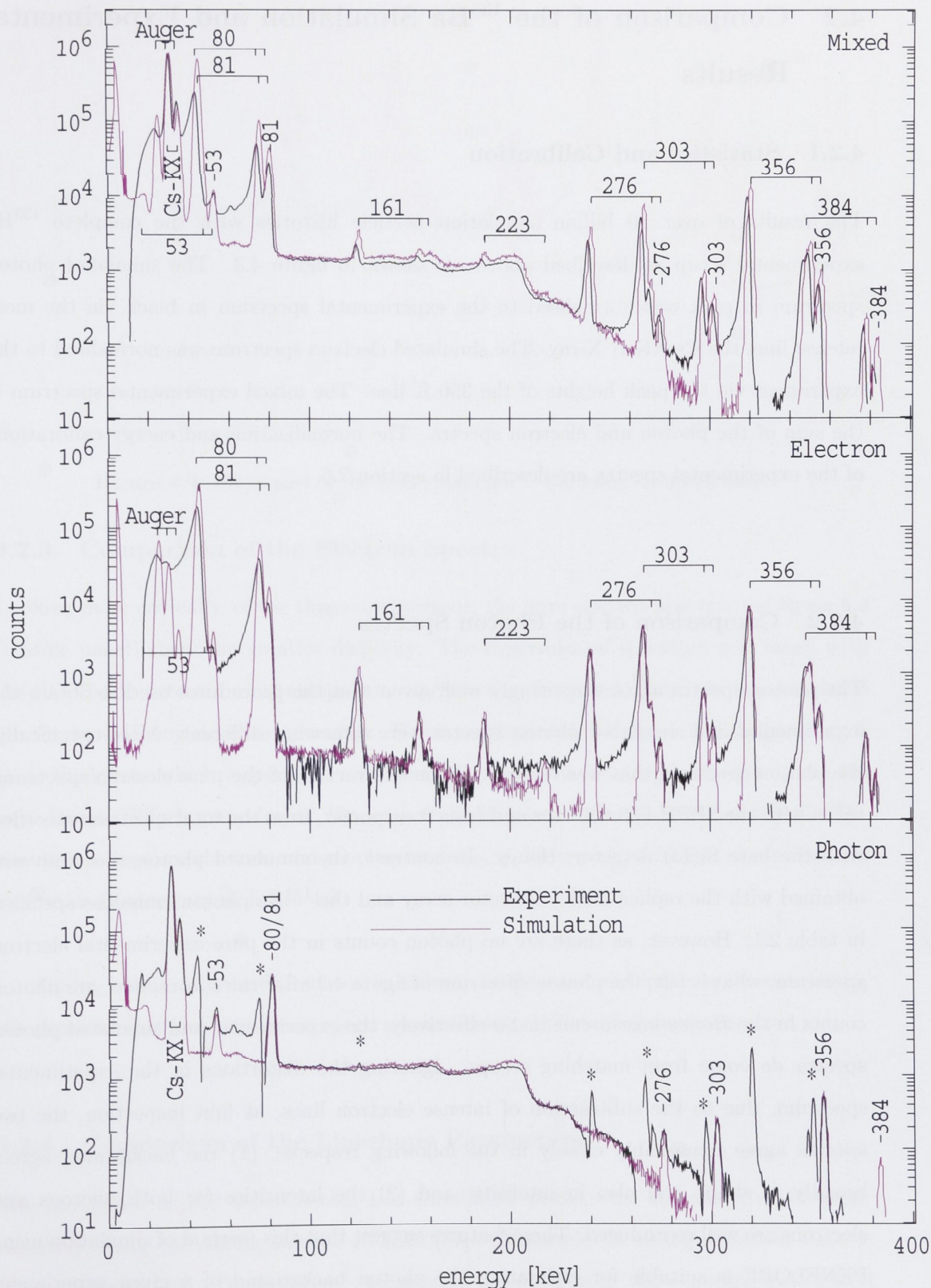


**Figure 4.3:** Comparison of experimental (see section 2) and simulated spectra. In all cases, the simulation data were obtained by using the energies and intensities of radiations, taken from table 2.1, incident on the bare Honey detector. Mixed: bare Honey detector; Electron: SEPH-530 detector and Lens transporter; Photon: the difference: Mixed - Electron spectra. Artifacts of the subtraction process are marked with \*.

---

## 4.2 Comparison of the $^{133}\text{Ba}$ Simulation and Experimental Results

### 4.2.1 Statistics and Calibration

The results of over 10 billion simulation particle histories with the complete  $^{133}\text{Ba}$  experimental setup as described above are shown in figure 4.3. The simulated photon spectrum in pink was normalised to the experimental spectrum in black via the most intense line, the Cs-XK $\alpha_1$  X-ray. The simulated electron spectrum was normalised to the experiment via the peak heights of the 356 K line. The mixed experimental spectrum is the sum of the photon and electron spectra. The normalisation and energy calibrations of the experimental spectra are described in section 2.6.

### 4.2.2 Comparison of the Photon Spectra

The photon spectra agree surprisingly well, given that the procedures used to obtain the experimental and simulated photon spectra were somewhat different. More specifically, the photon spectrum that was recorded is the subtraction of the pure electron spectrum, taken with the SEPH-530 detector and Lens transporter, from the total spectrum recorded with the bare Si(Li) detector, Honey. In contrast, the simulated photon spectrum was obtained with the replica Honey detector array and the  $^{133}\text{Ba}$  photon emissions specified in table 2.1. However, as there are no photon counts in the pure experimental electron spectrum, what is left, the photon spectrum of figure 4.3 after the subtraction, are photon counts in the *Honey measurement*. So effectively, the experimental and simulated photon spectra *do* come from matching setups. Ignoring the distortions in the experimental spectrum, due to the subtraction of intense electron lines, at first inspection, the two spectra agree remarkably closely in the following respects: (1) the background agrees broadly in shape and also in intensity, and (2) the intensities for both photons and electrons are well reproduced. These features suggest that this method of simulation using PENELOPE is suitable for estimating the photon background of a given experiment, as well as estimating the heights of photon peaks. The photon background, prevalent between 100 keV and 200 keV, is reproduced particularly well.

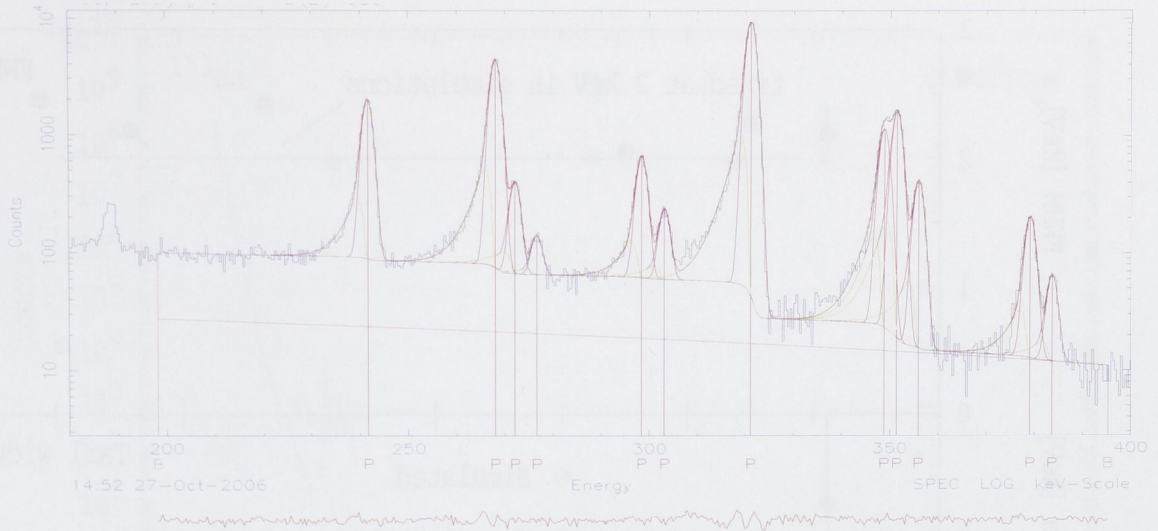


Figure 4.4: Fit to part of the Honey data for  $^{133}\text{Ba}$ , using the Fitek code.

### 4.2.3 Comparison of the Electron Spectra

Looking more critically, of the three comparisons, the pure electron spectrum of figure 4.3 (middle panel) show the greatest disparity. The experimental spectrum was taken with the SEPH-530 detector and transporter, whereas the simulated spectrum was calculated for the bare Honey detector geometry. However, the main difference in the detectors is their thickness, which is perhaps not overly important in the energy range up to 400 keV. Due to differing lineshapes, the peak to background ratios do not match well. The simulation lines are sharper, and more symmetric, a discrepancy which is also present in the “mixed” spectrum of figure 4.3.

Aiming to quantify the differences, in order to understand and improve the simulation, the experimental and simulation spectra were fitted and the lineshapes compared.

### 4.2.4 Comparison of the Lineshape Parameters

The lineshapes of the experimental and simulation peaks were compared more quantitatively using the fitting routine FITEK [87]. A sample fit to experimental data is shown in figure 4.4. The lineshape parameters obtained from the experimental (closed symbols) and simulation (open symbols) data are shown in figure 4.5. The full width at half maximum (FWHM) was fixed in the simulations. The magnitudes of the energy straggling tail heights are underestimated. It is unclear whether this is the result of poor

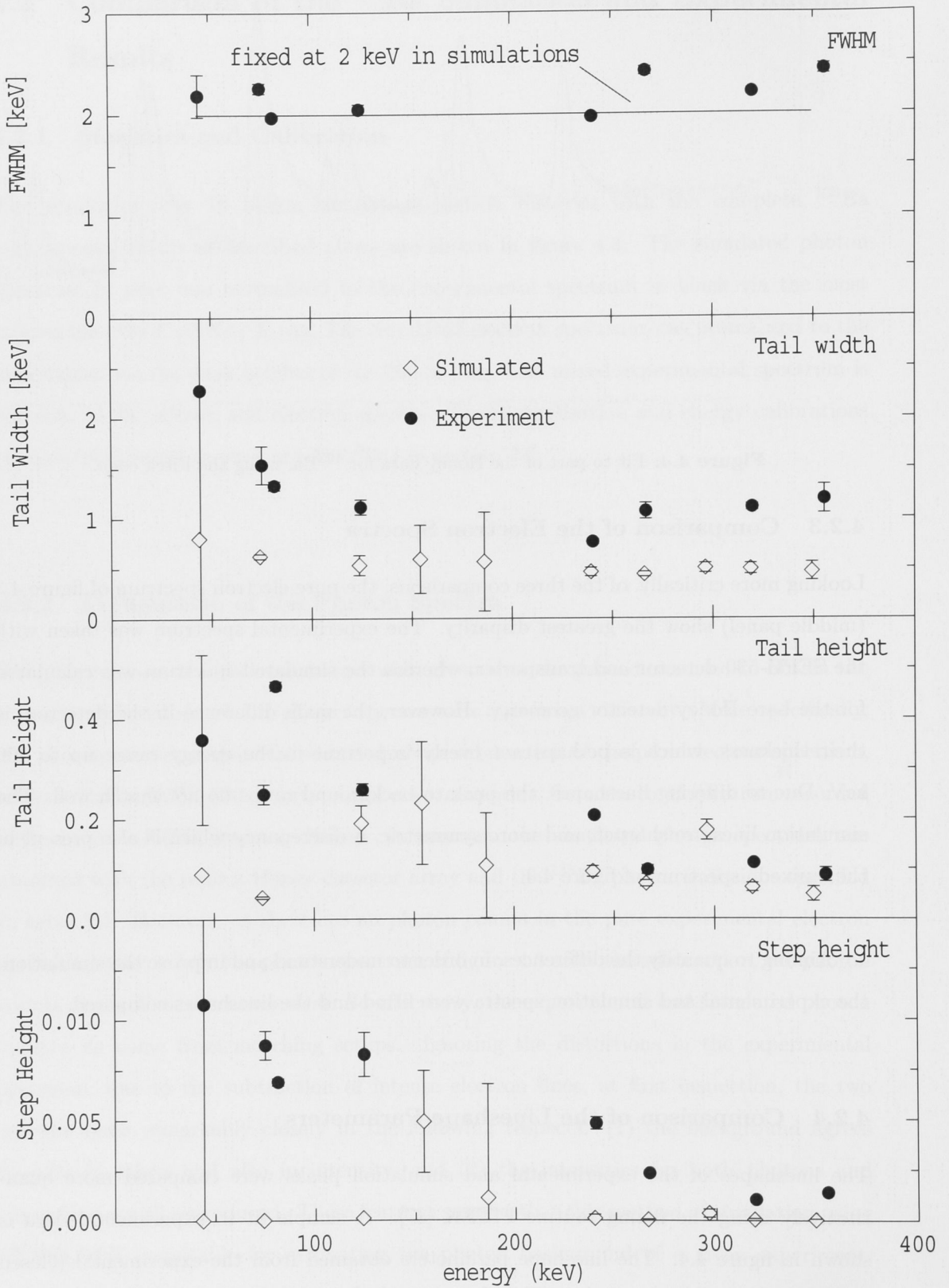


**Figure 4.5:** Fitting parameters, obtained by fitting the simulated (open symbols) and experimental (filled symbols) electron spectra of figure 4.3.



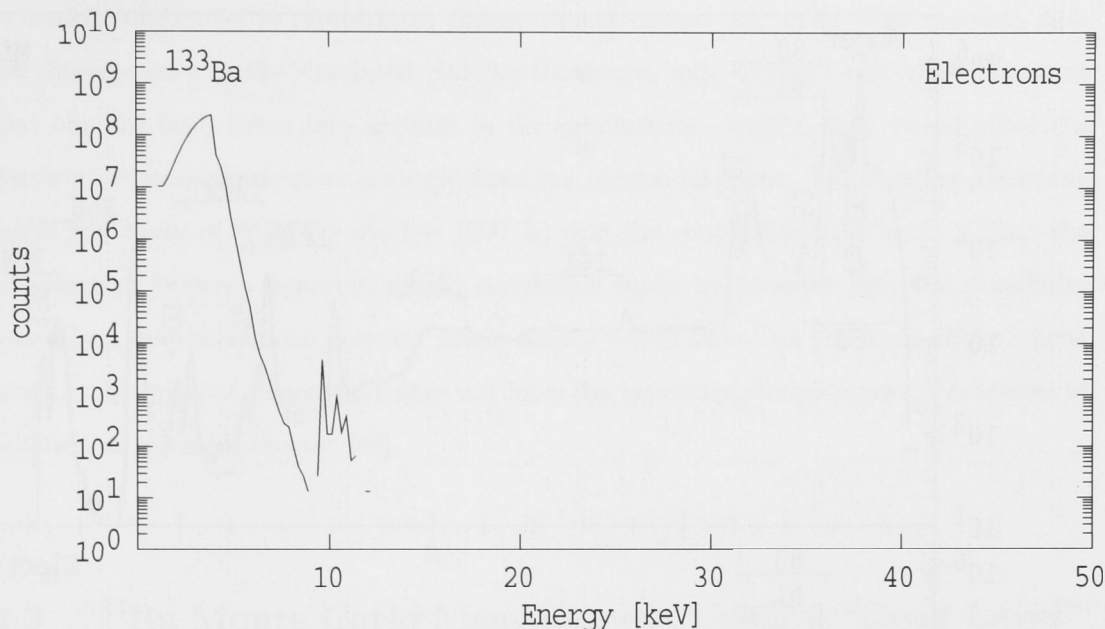


**Figure 4.6:** The energy absorption of the source, according to the simulation.

statistics, or the physical models of PENELOPE, or perhaps the geometries used in the simulations do not match closely enough with the experimental geometries. Also, we were unable to fit a step function to the simulated peaks. This could either be because approximating incomplete energy deposition in the detector by a step function is not valid, or could perhaps point to a more fundamental problem with the PENELOPE physical models.

The electron lineshapes were not reproduced accurately. The photon peak heights and backgrounds were reproduced well. Figure 4.6 shows that the energy absorption occurred in the source, which is expected to be important for the lineshape. The photon background in the Honey spectrum was reproduced well.

Although the results are promising, it is of concern that they do not reproduce the experimental conversion-electron lineshapes sufficiently well. Specifically, the simulated peaks are more symmetric, showing smaller energy straggling tails (see figures 4.5 and 4.5). The step height, which must be related to incomplete energy deposition, was also smaller in the simulations. This caused the peak to background ratio to be much higher in the simulations than was found experimentally. Out of the three plots of figure 4.3, the simulated photon spectrum agrees most closely with that of experiment; the peak

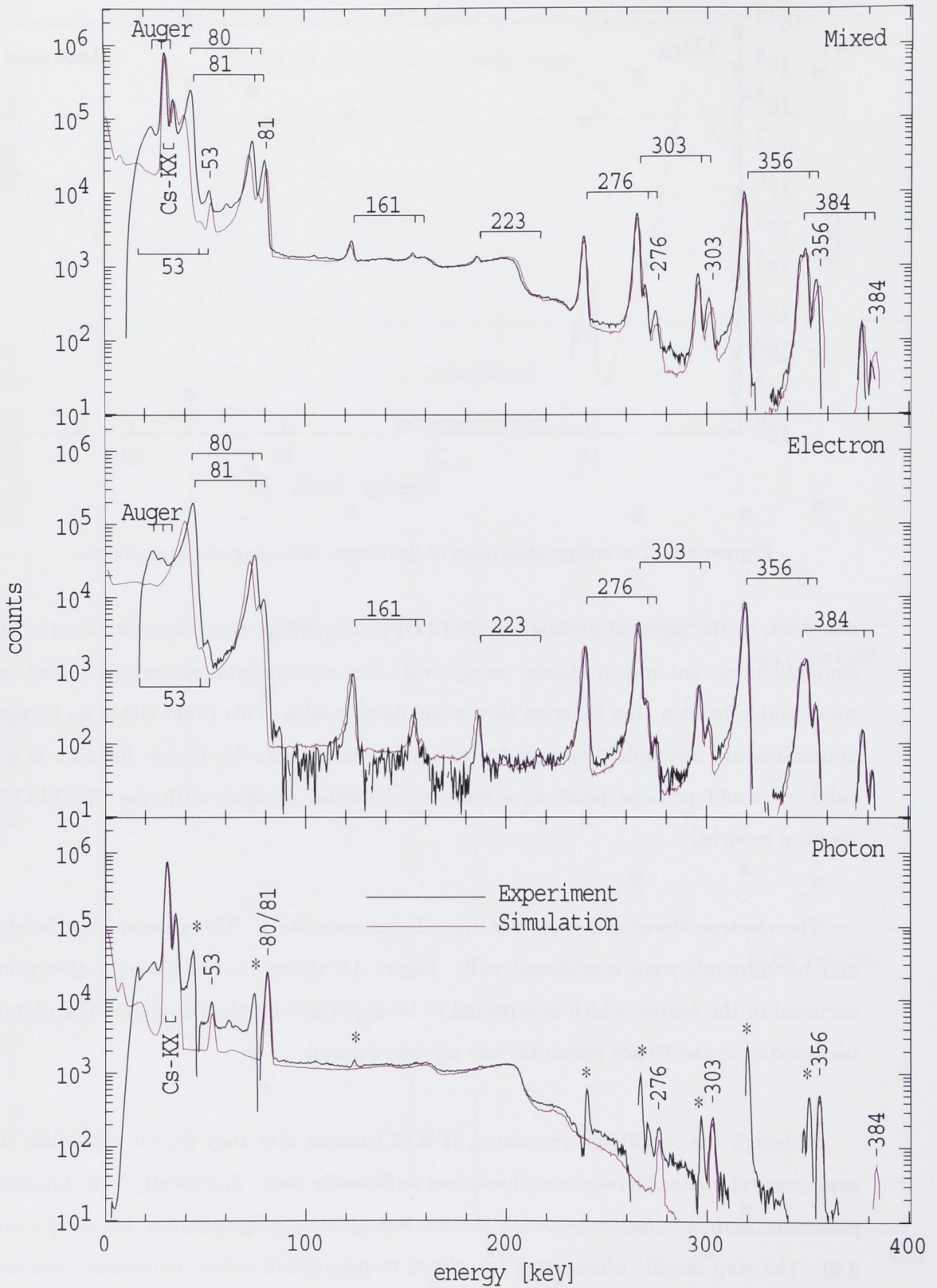


**Figure 4.7:** Experimental and Simulation results assuming a 4  $\mu\text{m}$  dead layer of silicon on the front face of the Honey detector crystal; Artifacts of the subtraction process are indicated by \*.

to background ratio is reproduced almost exactly above 100 keV. This suggests that the discrepancies in the simulated electron lineshapes may be due to an absorbing layer that has not been taken into account in the simulations - such a layer would affect the electron response much more strongly than the photon response. The existing absorbing layers are those of the gold window (200 Å) and the source itself (44 nm). Citing the comparisons between experiment and simulation made by Mesradi [88], the possibility was raised that the silicon detector might have a “dead layer” on the front of the silicon face *i.e.*, a region of silicon that does not have the necessary charge-carrier abundance to function as a semiconductor [89].

### 4.3 $^{133}\text{Ba}$ Monte Carlo Measurement Using a “Dead Layer” Honey Geometry

Simulations were run with Honey geometries with a dead layer of silicon of varying thicknesses. To speed up the process, only the 356 K line was simulated. A dead layer thickness of 4  $\mu\text{m}$  was chosen as the most accurate in reproducing the experimental lineshape, so the full list of  $^{133}\text{Ba}$  radiations was run for a Honey detector array with 4  $\mu\text{m}$  dead layer. The results shown in figure 4.7 overall show a much better agreement with experiment than the results of the previous Monte Carlo run, section 4.1. The comparison of the two spectra may be divided into the following points:

1. Inspection of the spectra shows a close agreement, except for an offset at low energy in the simulated spectrum
2. Low energy offset, and arguments for and against the dead layer
3. Comparison of the simulation and experimental lineshape parameters:
  - (a) Incomplete energy deposition
  - (b) Energy straggling
  - (c) Full width at half maximum,

which are discussed below.

### 4.3.1 Inspection of Figure 4.7

The results are shown in figure 4.7 and the results of fitting the simulation and experimental parameters are shown in figure 4.9. The excellent agreement between simulation and experiment supports the theory that the SEPH-530 and Honey detectors contain a Si dead layer on the front window. As in the previous simulations shown in figure 4.3, the photon spectrum was reproduced well, showing that the dead layer has little to no effect on the photon response. The electron and mixed spectra agree much more closely, however. The peak to background ratio is reproduced well in both the pure electron and the mixed spectra, some slight differences at higher energies are likely due to both low statistics in the experimental measurement - and imprecise ambient background subtraction in the experimental measurement. There is no ambient background in the simulations, so experimental ambient background subtraction is necessary to compare the experiment and simulations. Due to limited access to the facilities, the ambient background spectrum was recorded later, and an ambient background was only recorded for the Honey setup, not the Lens transporter - SEPH-530 setup. At high energies (above the 356 K line) the spectra background intensity drops to zero in both the experimental, and simulation, much larger statistics in both would be needed to see the peak to background ratio in this area.

### 4.3.2 Low Energy Offset and Arguments For and Against the Dead Layer

The most significant difference between experiment and simulation occurs in the electron peaks below 100 keV. The energies of the simulated peaks are offset from the experimental peaks by around 4 keV at the worst agreement, the 81 K line. Absorbing layers such as the silicon dead layer are known to shift the energy of the peak, and it is likely to be the treatment of this that is causing the energy shift. While at first, this may indicate that the assumption of a dead layer is inappropriate, the presence of a dead layer is supported by the generally excellent agreement in the lineshapes. Any reduction in the dead layer thickness is likely to worsen the agreement between lineshapes and peak to background ratios. The presence of a dead layer is also supported by comparing the photon and electron calibrations. By fitting the photon peaks from the mixed spectra, an energy calibration of  $E = 0.4010 \text{ (keV/CH)} \times CH - 0.72 \text{ keV}$ , where  $CH$  is the

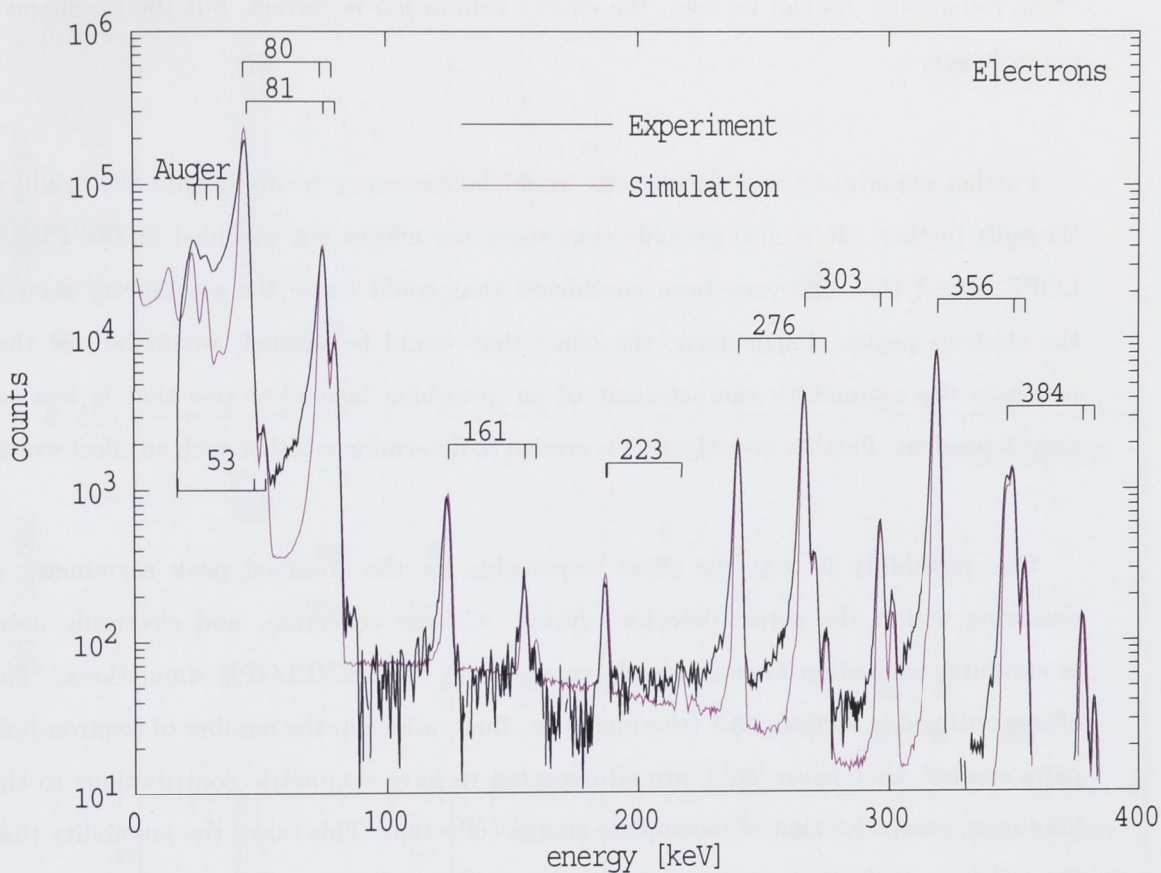


**Figure 4.8:** Simulation of the  $^{133}\text{Ba}$  measurement for a  $1\ \mu\text{m}$  silicon dead layer compared to the SEPH-530 experimental data.

channel, was obtained, whereas by fitting the electron peaks, an energy calibration of  $E = 0.3995\ (\text{keV}/\text{Channel}) \times CH + 0.55\ \text{keV}$  was obtained. This shows that there is an offset between photons and electrons of  $1.27\ \text{keV}$ , an offset that is likely to be caused by energy absorption. Furthermore, figure 4.3, would suggest that the experimental lineshapes cannot be reproduced without a dead layer. It is possible that PENELOPE does not reproduce the energy loss due to passing through a thin absorbing layer well at energies below  $100\ \text{keV}$ . Further experiments and accurate knowledge of the detector window structure would be necessary to confirm or discount this possibility. However, considering the  $^{12}\text{C}$  measurement, the higher energy region is of primary interest, where the agreement is excellent.

Investigations showed that in order to achieve an agreement between the simulated and experimental peak energies, the dead layer thickness must be reduced to  $1\ \mu\text{m}$ . Figure 4.8 shows the results of a  $1\ \mu\text{m}$  dead layer - Honey geometry, simulated for the

$^{133}\text{Ba}$  radiations. As can be seen, the energy calibration is correct, but the lineshape is not accurate.

Further experiment and simulations would be necessary to investigate the origin of the tails further. It is also possible that there are effects not included in the PENELOPE model that have not been considered that could cause the asymmetry seen in the electron peaks. Particularly, the effect that would be needed, would be one that produces the asymmetry characteristic of an absorbing layer, but one that is less energy dependent. Further investigation is needed to determine whether such an effect exists.

One possibility is that the effect responsible for the observed peak asymmetry is occurring within the active detector crystal. Charge collection, and electronic noise is currently treated as Gaussian and symmetric in the PENELOPE simulations. The effects outlined in section 2.3.1 (thermal noise, fluctuations in the number of electron-hole pairs created, shot noise, *etc.*) are all expected to have symmetric contributions to the lineshape, except for that of incomplete charge collection. This raises the possibility that the tail may, at least in part, come from incomplete collection of electron-hole pairs in the semiconductor. However, the absence of any tail from the photon peaks casts doubt on this hypothesis. Photons would however, deposit their energy with a different depth distribution, which could give rise to different charge collection properties.

### 4.3.3 Comparison of Experimental and Simulation Lineshape Parameters

Figure 4.9 shows the lineshape parameters obtained by fitting the simulated and experimental electron spectra using Fitek [87]. The fit parameters shown are: the step height - due to incomplete energy deposition; the tail height and tail width, due to energy straggling; and the full width at half maximum due to charge collection effects and electronic noise. The parameters agree very well, as there are not only uncertainties in the fitting process, but also in the experimental and simulation spectra being fitted.

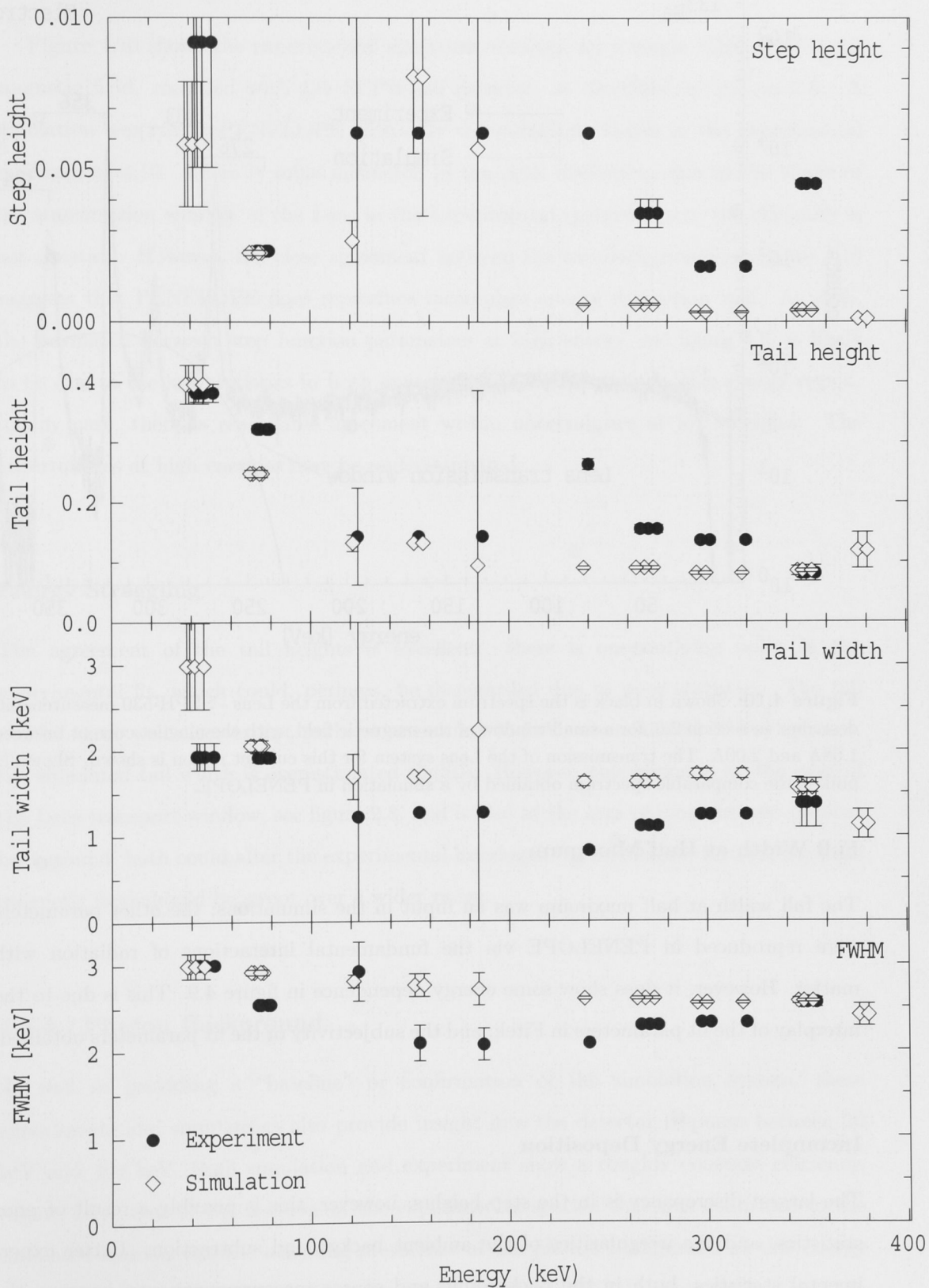


**Figure 4.9:** Fitting Parameters, obtained by fitting the simulated (open symbols) and experimental, (filled symbols) electron spectra of figure 4.7.

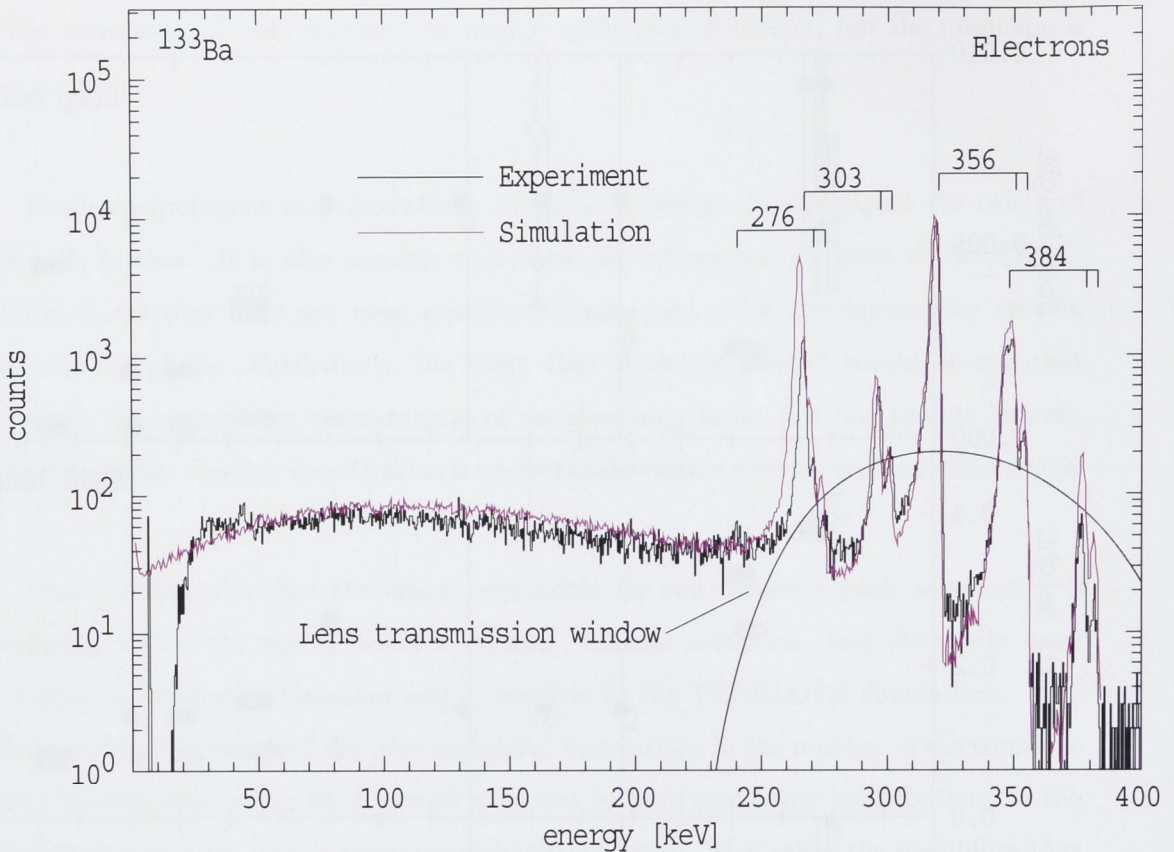


**Figure 4.10:** Shown in black is the spectrum extracted from the Lens - SEPH-530 measurement, described in section 2.6, for a small window of the magnetic field, with the magnet current between 1.68A and 2.00A. The transmission of the Lens system for this current region is shown. Shown in pink is the comparable spectrum obtained by a simulation in PENELOPE.

### Full Width at Half Maximum

The full width at half maximum was an input in the simulations; the other parameters were reproduced in PENELOPE via the fundamental interactions of radiation with matter. However, it does show some energy dependence in figure 4.9. This is due to the interplay of the fit parameters in Fitek, and the subjectivity of the fit parameters obtained.

### Incomplete Energy Deposition

The largest discrepancy is in the step heights, however, this is possibly a result of poor statistics, and the irregularities of the ambient background subtraction. Better experimental statistics, both in the background and source measurements may improve the agreement. It is possible that PENELOPE's treatment of incomplete energy deposition is inconsistent with the fitting of a step function.



Figure 4.10 shows the experimental spectrum obtained for a single value of the Lens magnetic field, recorded with the SEPH-530 detector, as described in section 2.6. A simulation was run in PENELOPE with only the radiations visible in the experimental spectrum of 4.10. There is some mismatch in the peak intensities, due to the shape of the transmission window of the Lens in the experimental spectrum, *i.e.*, the efficiency is not constant. However, the close agreement between the two backgrounds in figure 4.10 suggests that PENELOPE does reproduce incomplete energy deposition well. As such, the mismatch between step function parameters at high energy, see figure 4.9, is likely to be due to the low statistics in both experiment and simulation, in this energy region. In any case, there is reasonable agreement within uncertainties at low energies. The uncertainties at high energies may be underestimated.

### Energy Straggling

The agreement of the tail heights is excellent: there is one outlying point in the experimental fit, which could, perhaps, be disregarded due to poor statistics. The tail widths agree well also, except perhaps at around 45 keV, where the 81 K line appears, the simulated tail width is overestimated slightly. However, this region is on the edge of the Lens transport window, see figure 2.8, and is also at the area of most intense ambient background, both could alter the experimental lineshape. To investigate further, the Lens magnetic field should be swept over a wider range.

#### 4.3.4 Photon Background

As well as providing a “baseline” or confirmation of the simulation system, these experiments and simulations also provide insight into the detector response between 20 keV and 400 keV. Both simulation and experiment show a roughly constant efficiency, (figure 2.7). One of the features of the experimental spectra that was confirmed in the simulated spectra was the alarming prevalence of the photon background at this energy range. Below the 356 keV Compton edge, which occurs at 203 keV, the complex Compton spectrum at lower energies, as described by Compton theory can be seen. In the energy region of 100 - 200 keV, Compton electrons accounted for around 99.9% of all events

recorded by the detector. This explains the high background seen in this region of the experimental data, and the lack of visibility of the electron peaks expected there. The most intense electron peaks in this region were only visible as 10% “bumps” on the dominant Compton electron background. Full energy photon peaks were also visible; PENELOPE predicts that 0.4% of 356 keV photons incident on the Honey detector array will deposit their full energy in the detector. A corresponding experimental value of 1% was obtained from the 356 photon peak area in figure 2.9.

#### 4.4 Efficiency as Function of Energy

Further simulations were combined with the  $^{56}\text{Co}$  measurement to extend the detector characterisation up to 3.5 MeV. Using PENELOPE, the dependencies of the efficiency on angle and energy were investigated for electrons incident on a silicon crystal. A cylindrical geometry was used, with mono-energetic line-beams of electrons of  $0^\circ$ ,  $15^\circ$ ,  $30^\circ$ ,  $45^\circ$  and  $60^\circ$  angular incidence. The energy range sampled was 2 keV - 3.5 MeV. A simple cylinder of homogeneous silicon, of diameter 50 cm and thickness 1 cm, was used and a total of 1 million showers were simulated for each point.

Run	Efficiency (%)
1	78.19
2	78.57
3	78.25
4	78.42
5	78.63
6	78.45
7	78.69
8	78.49
9	78.67
10	78.59
Average	$78.50 \pm 0.17$

**Table 4.2:** A sample spread of results, obtained by running the same simulation 10 times.

Plotted in figure 4.11 is  $P = (1 - \eta_{det})$  as a percentage, where  $\eta_{det}$  is the efficiency of the crystal, defined by

$$\eta_{det} = \frac{A_{(peak)}}{A_{(spectrum)}}, \quad (4.1)$$

where  $A_{(peak)}$  is the number of counts in the full energy peak and  $A_{(spectrum)}$  is the total

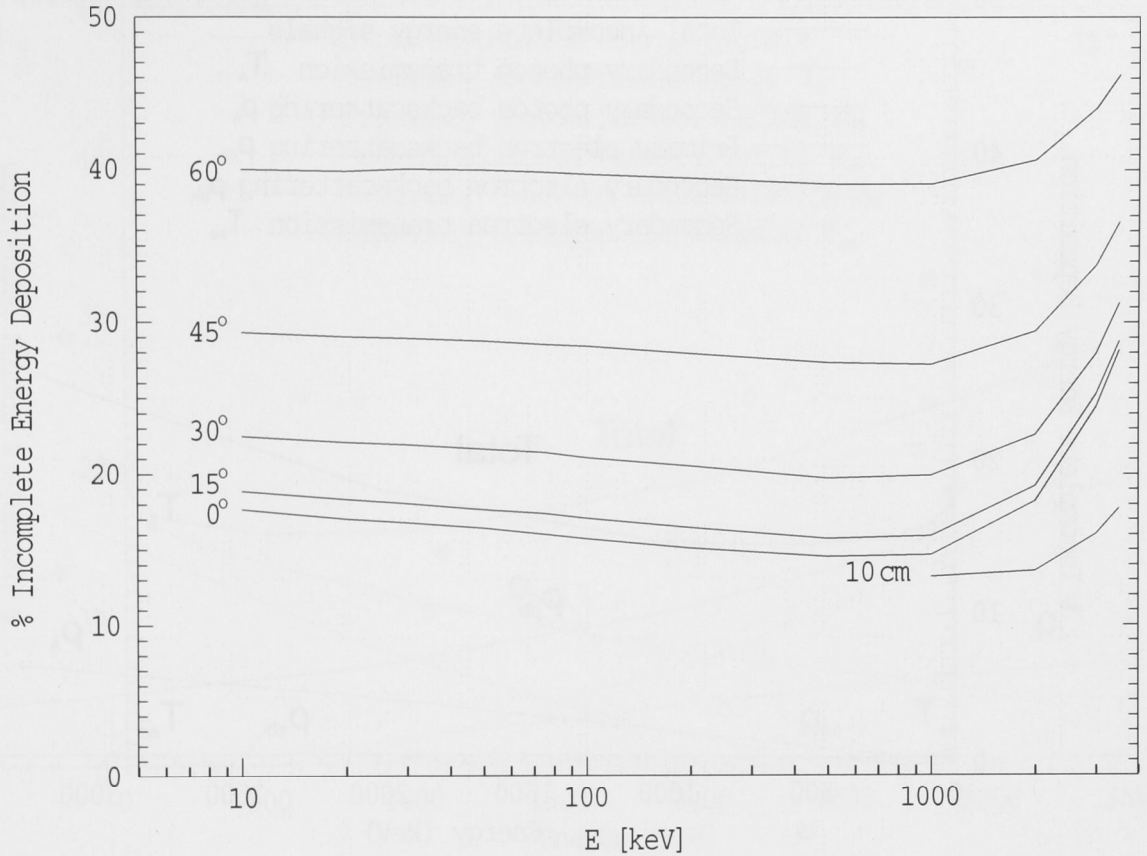


**Figure 4.11:** Probability of incomplete energy deposition for a 1 cm thick Si(Li) detector, 1 million particle histories per point. Also shown are four points (1 MeV, 2 MeV, 3 MeV and 3.5 MeV), calculated for  $0^\circ$  incidence on a 10 cm thick detector.

number of counts in the spectrum, equal to the total number of input primary radiations (1 million). This is equivalent to that of equation 2.3, as for a single input energy, the number of radiations that strike the detector with that energy is the total area of the spectrum. Plotted in figure 4.11, then, is the total efficiency *loss* as a function of angle and energy. A strong dependence on both angle and energy is shown. The magnitude of the statistical uncertainties was investigated, see table 4.2. Ten repetitions of the same Monte Carlo experiment were conducted for each point for a given angle ( $30^\circ$ ). Based on the standard deviation of the Monte Carlo runs, the statistical errors were found to be negligibly small, at least compared to the uncertainties inherent in the physical models used. For example, the data given in table 4.2, has a standard deviation of 0.17% due to Monte Carlo statistics.

Figure 4.11 shows a somewhat alarming rise in the probability of incomplete energy

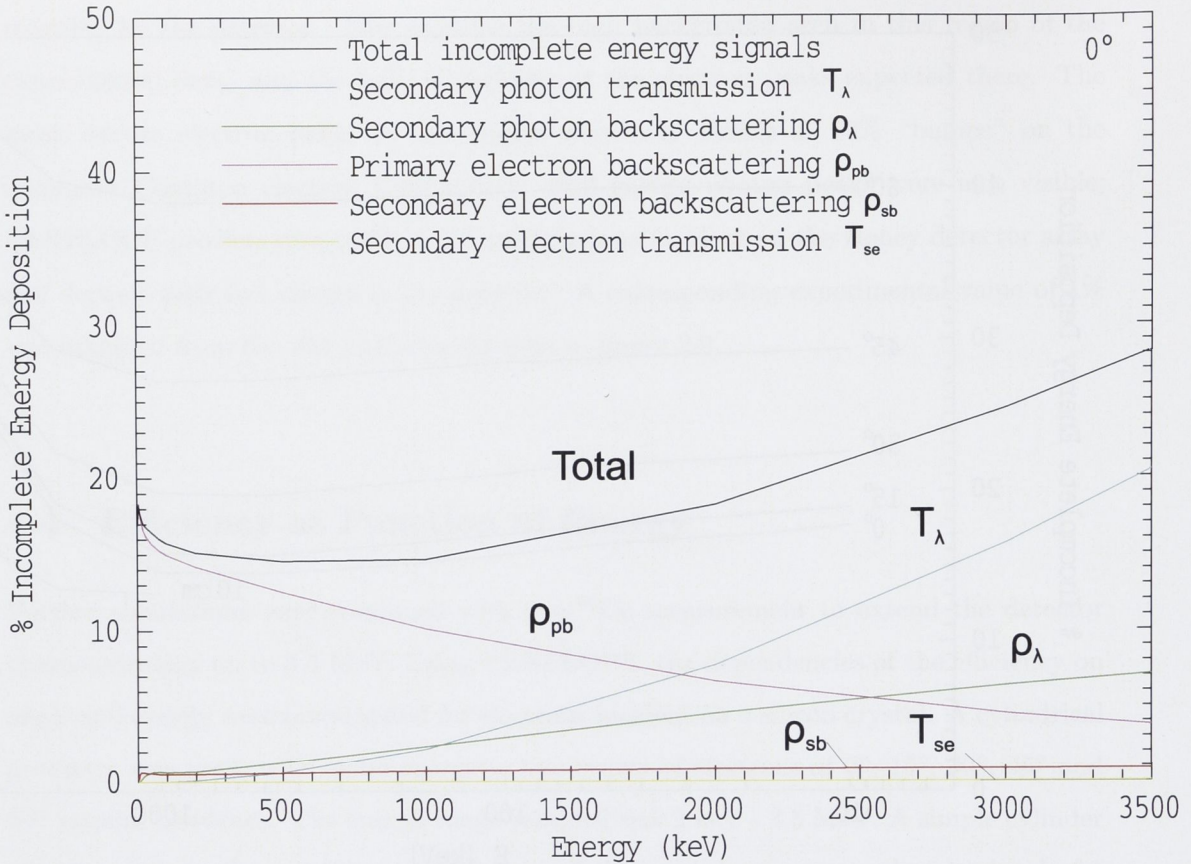


**Figure 4.12:** Sources of efficiency loss for the  $0^\circ$  curve in figure 4.11. The contributions of secondary photon emission, secondary photon backscattering, primary electron backscattering, secondary electron backscattering and secondary electron transmission are shown.

deposition above 1 MeV. This poses an experimental problem to which increasing the thickness of the detector is the obvious solution. Simulations were therefore run for a much thicker silicon detector of 10 cm thickness, see figure 4.11. These results still show an increase in the probability of incomplete energy deposition above 1 MeV, but the increase is not as steep. However, the benefit is not as dramatic as may be hoped, for such a thick semiconductor; and a Si(Li) with a thickness of 10 cm would be challenging to manufacture. In order to shed light on the energy dependence in figure 4.11, the sources of energy loss were investigated. PENELOPE provides the following quantities for each simulation:

- number of backscattered secondary photons
- number of transmitted secondary photons
- number of backscattered secondary electrons

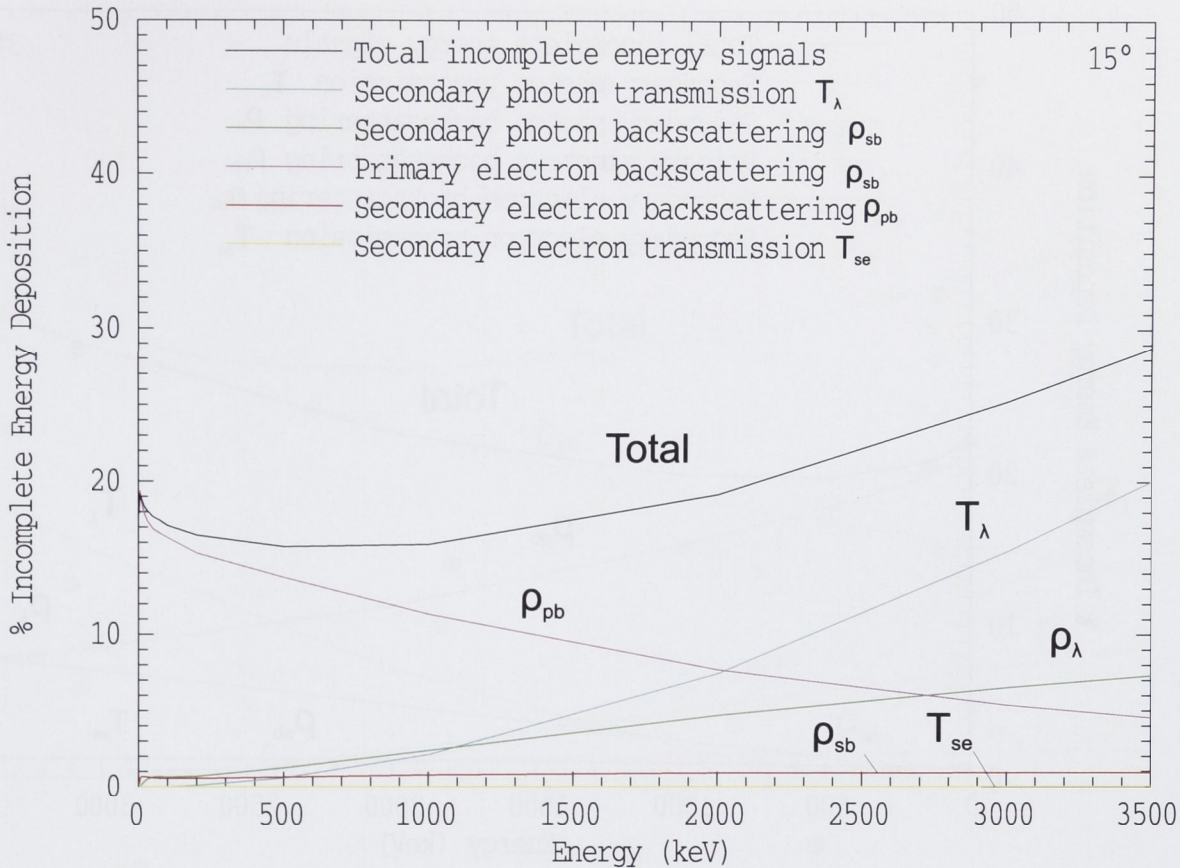


Figure 4.13: Same as figure 4.12, but for  $15^\circ$  incidence.

- number of backscattered primary electrons
- number of transmitted primary electrons

These quantities were plotted as a function of energy, for a fixed angle (see figures 4.12 4.13 4.14 4.15 4.16) and as a function of the angle of incidence  $\theta$ , for a sample energy (3.5 MeV), see figure 4.17. Figures 4.12 4.13 4.14 4.15 4.16 show that while the primary backscattering decreases as a function of energy, the transmitted photon probability rises dramatically for high energies. This feature is explained by the increasing radiative stopping power in that energy region. At around 500 keV - 1 MeV the radiative stopping power rises steeply as a function of energy, see figure 3.7. This is not caused by any increase in the radiative cross section, but by an increase in the average energy per bremsstrahlung photon. The higher energy photons are more likely to escape from the detector, which explains the loss of efficiency seen at high energy in figure 4.11. The first region of figure 4.11, where a small, linear decrease in incomplete energy deposition with energy is seen, is as expected, and is due to the well known decrease of primary

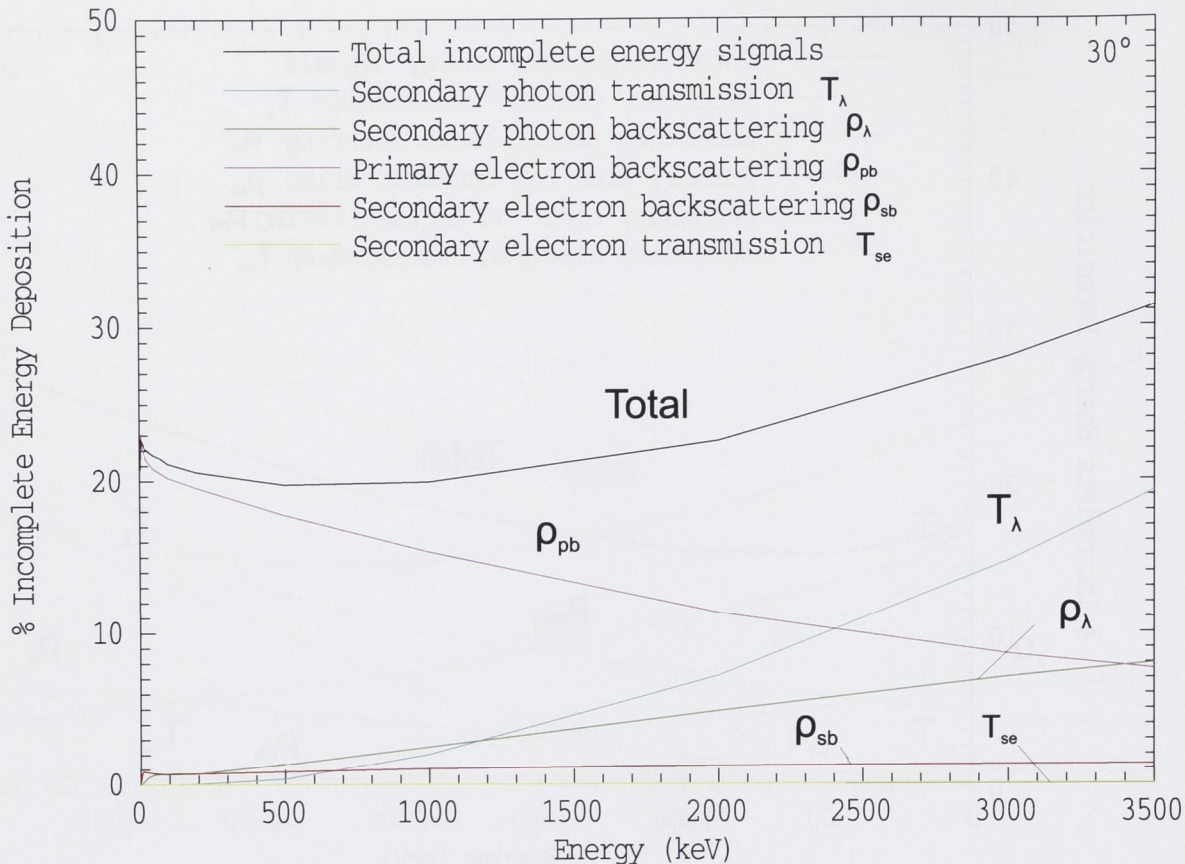


Figure 4.14: Same as figure 4.12, but for  $30^\circ$  incidence.

backscattering with energy. Figures 4.11, 4.12 - 4.17 both explain why the approach taken in the literature has been that primary backscattering is the only source of efficiency loss in a Si(Li) electron detector measurement, and also show that in general, it is inadequate. Below 100 keV, primary backscattering is indeed responsible for almost all the incomplete energy depositions. In fact, it is the dominant form of incomplete energy deposition below 1 MeV. Above that energy however, the dominant form of energy loss is the transmission of photons produced by bremsstrahlung events. The backscattering of bremsstrahlung photons becomes quite significant also. This misinterpretation will surely need to be corrected if high-energy pair spectroscopy is to be developed further.

Following on from the previous simulations, which were conducted for a 1 cm thick detector, like the SEPH-530 detector, a similar set of simulations were conducted with a 4.3 mm thick detector - the thickness of the Honey detector - as the  $^{12}\text{C}$  measurement proposes to use the Honey detector array, at least for pilot studies. The results are shown in figure 4.18. An identical set of measurements, but with incident positrons instead

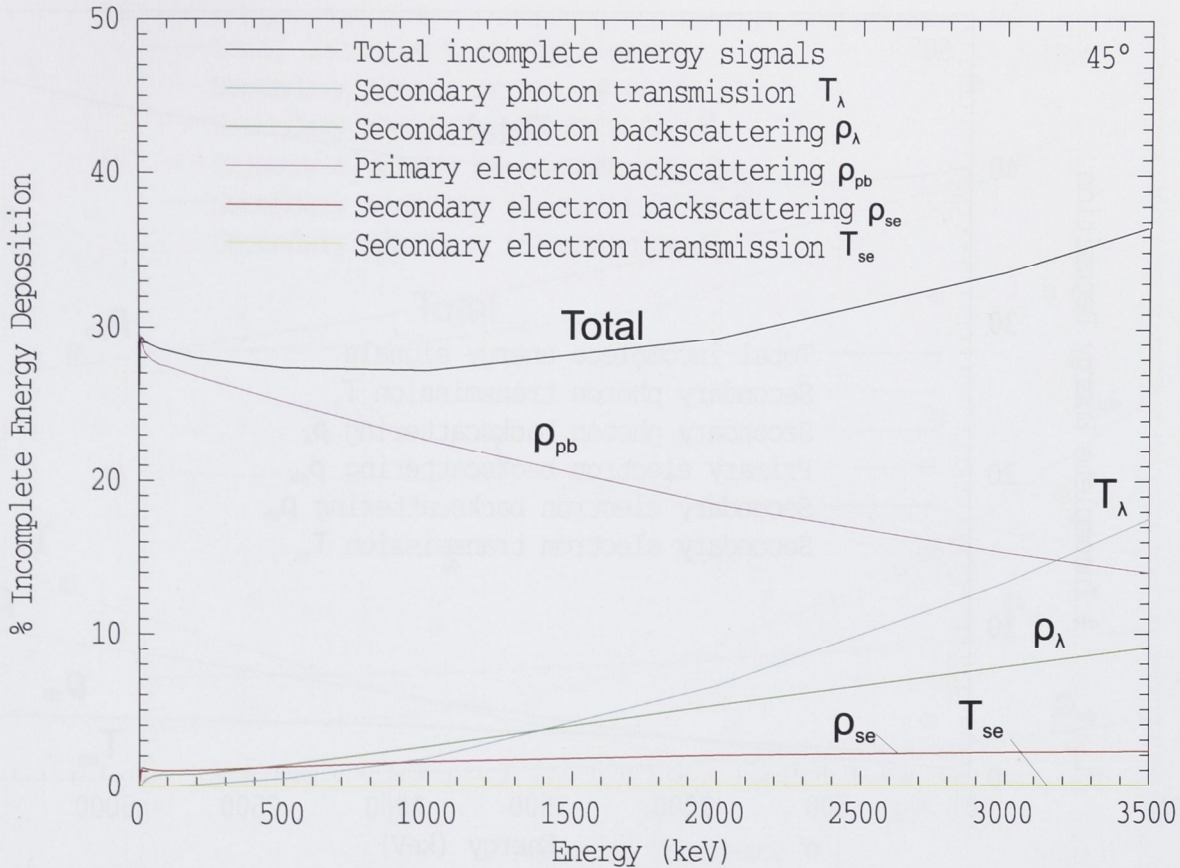


Figure 4.15: Same as figure 4.12, but for  $45^\circ$  incidence.

of electrons, were simulated, see figure 4.19. As would be expected from the previous results, the loss of efficiency above 1 MeV is marked for both electrons and positrons with the efficiency for electrons dropping below 30% at 3.5 MeV, and the efficiency for positrons dropping below 20% at 3.5 MeV. The lines cross each other, *i.e.*, the  $0^\circ$  case has the highest efficiency at low energy, but has the lowest efficiency at 3.5 MeV. This is most likely due to the tendency of bremsstrahlung photons to be emitted in the forward direction, see figure 3.7.

The results of 4.18 and 4.19 pose a major concern for the proposed measurement of the radiative width of the Hoyle state in  $^{12}\text{C}$ , if the Honey detector must be used to make quantitative measurements of electron - positron pairs at 3.3 MeV. Figures 4.18 and 4.19 would suggest an efficiency of around 30% for electrons and 20% for positrons, depending on the angle of incidence. The fact that the efficiency is changing so drastically with energy at 3.3 MeV, is also a concern, when one considers that the energy calibration may not be exact. In light of this, a 1 cm thick version of the Honey detector is proposed for

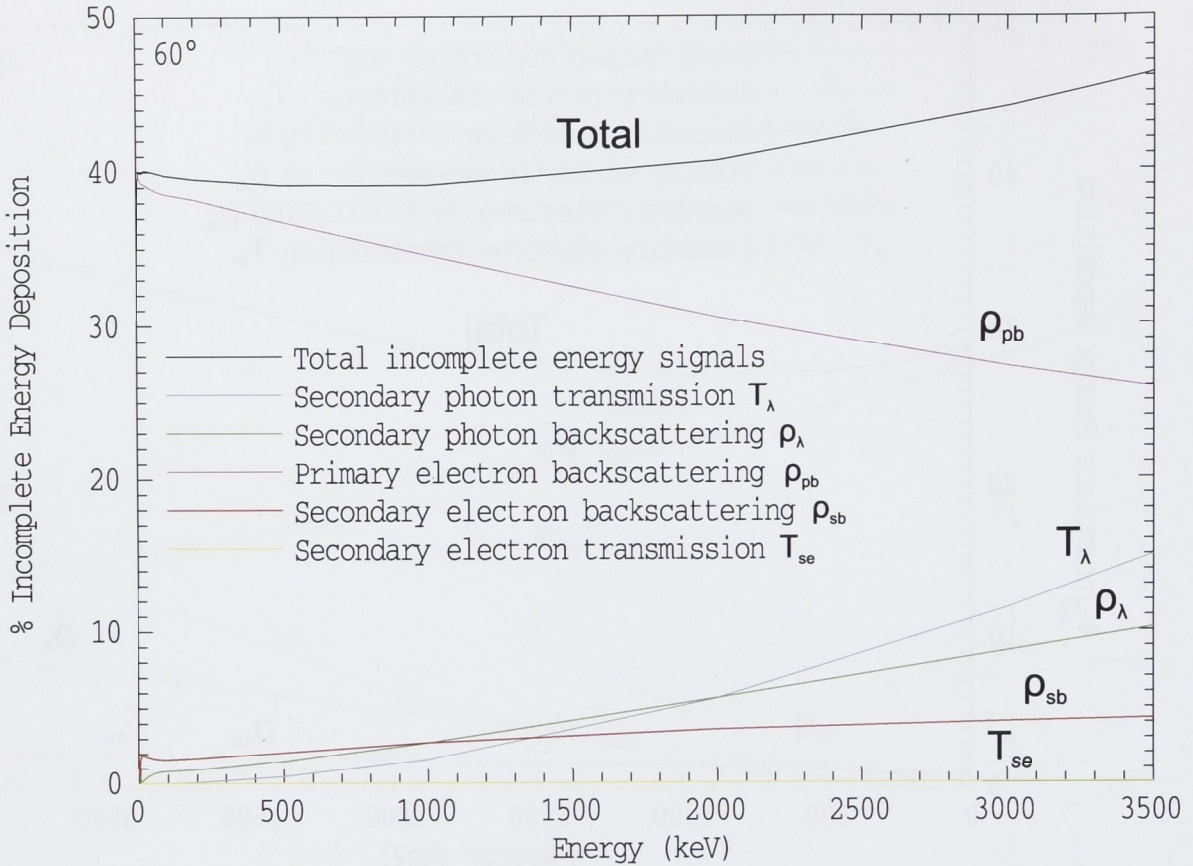


Figure 4.16: Same as figure 4.12, but for  $60^\circ$  incidence.

use in the Hoyle state measurement.

## 4.5 Empirical Formula for Efficiency as a Function of Energy and Angle

Figure 4.20 combines the simulated data on Si(Li) detector efficiency. It is the same data set as figure 4.11, but plotted as the efficiency, rather than percentage of incomplete energy deposition. These plots take several weeks of computer time to generate by the Monte Carlo method. With a view to cutting computer time, an empirical formula was developed here, to fit the data points as a function of energy  $E$  and incident angle  $\theta$ . The aim is to obtain a formula for use as a quick reference in planning experiments or detector design, in the absence of a Monte Carlo run or experimental study. It is also necessary to interpolate between the data points of figure 4.20, especially as there are only 5 angles plotted. The formula could also be used (with caution) to extrapolate the results to higher



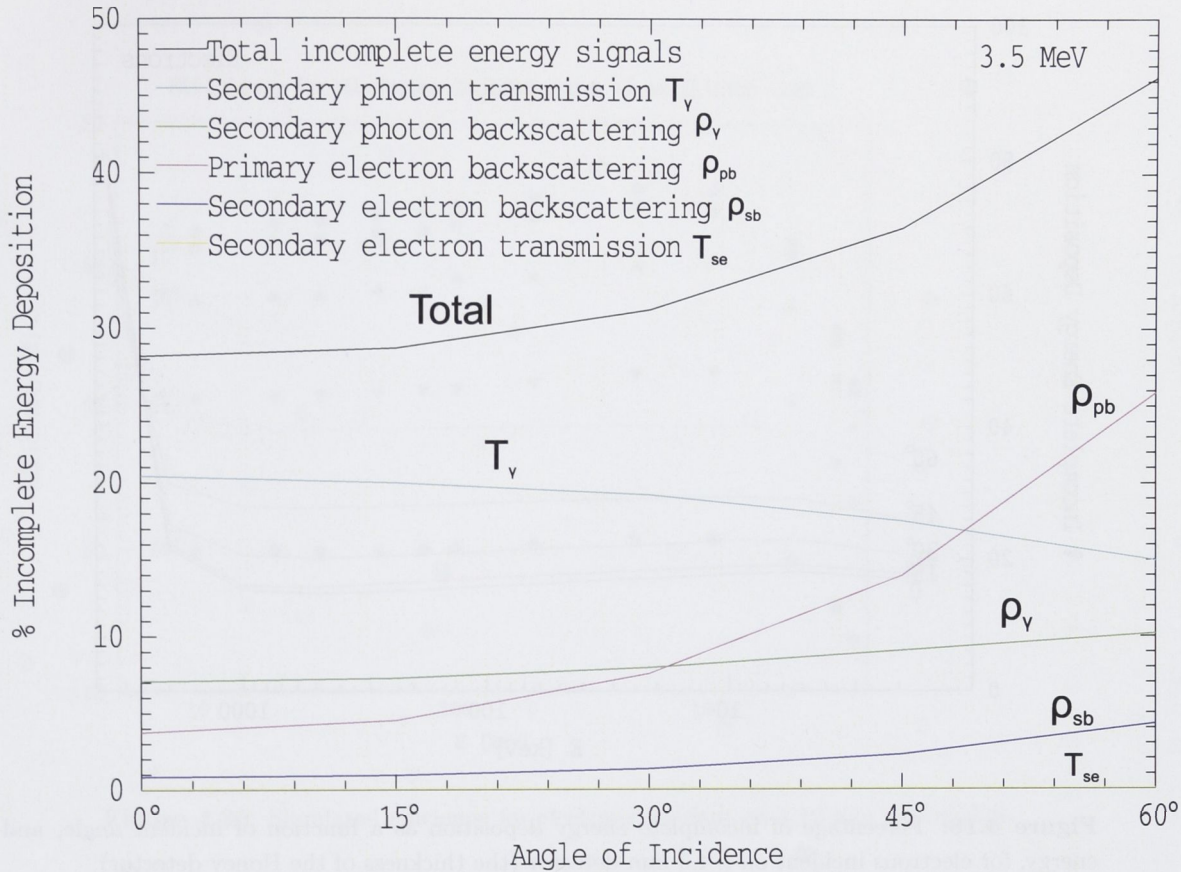


**Figure 4.17:** Sources of efficiency loss plotted as a function of angle for an energy of 3.5 MeV.

energies. Plotted in figure 4.20 are the same results of figure 4.11, shown in data point form.

To obtain an empirical formula, the energy dependence of figure 4.20 was divided into two regions:

1. the first, ranging from 10 keV up to 200 keV, where the function is roughly linear, and proportional to energy, as shown in figure 4.21;
2. the second ranging from 200 keV to 3.5 MeV, where the efficiency decreases with the incident energy in a quadratic nature, is shown in figure 4.23.

The first region was fitted as a linear function of energy:

$$\eta(E) = a_1 + a_2E, \tag{4.2}$$

see figure 4.21.

The values of the fitting parameters are shown in table 4.3. The parameter  $a_1$  was

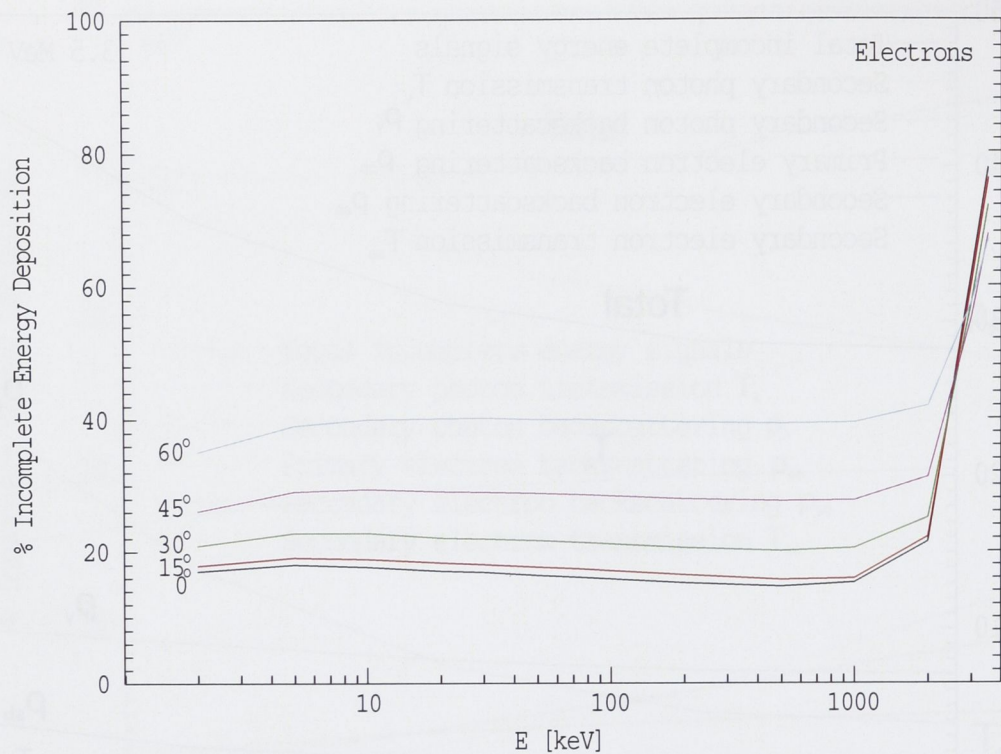


**Figure 4.18:** Percentage of incomplete energy deposition as a function of incident angle, and energy, for electrons incident on a 4.3 mm detector (the thickness of the Honey detector).

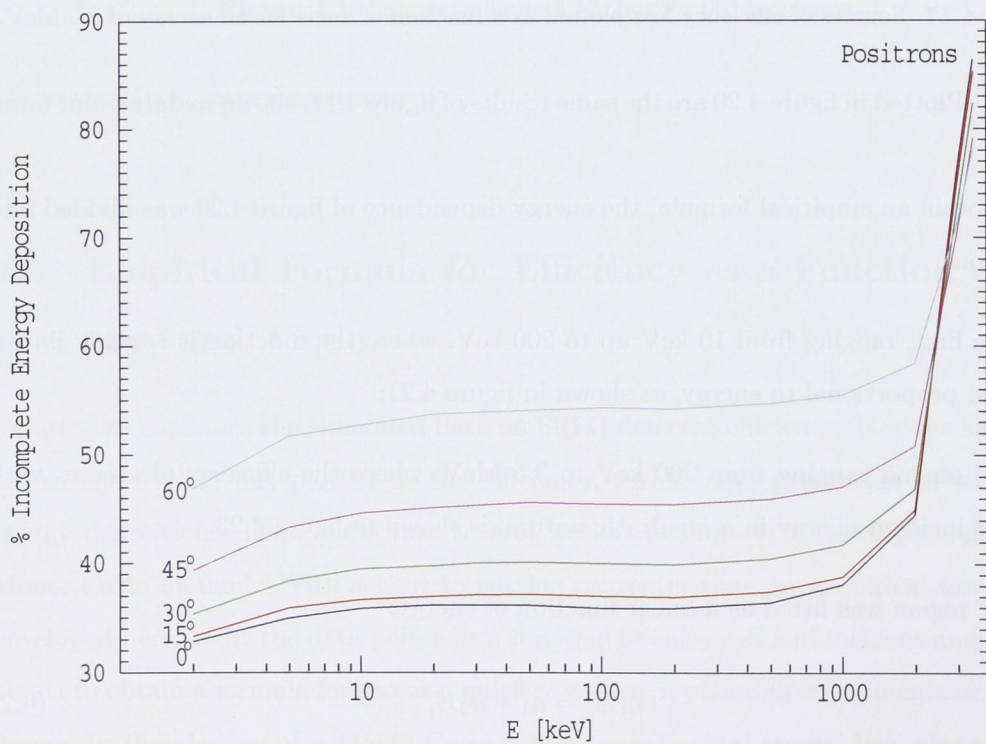


**Figure 4.19:** Same as figure 4.18, but for positrons.

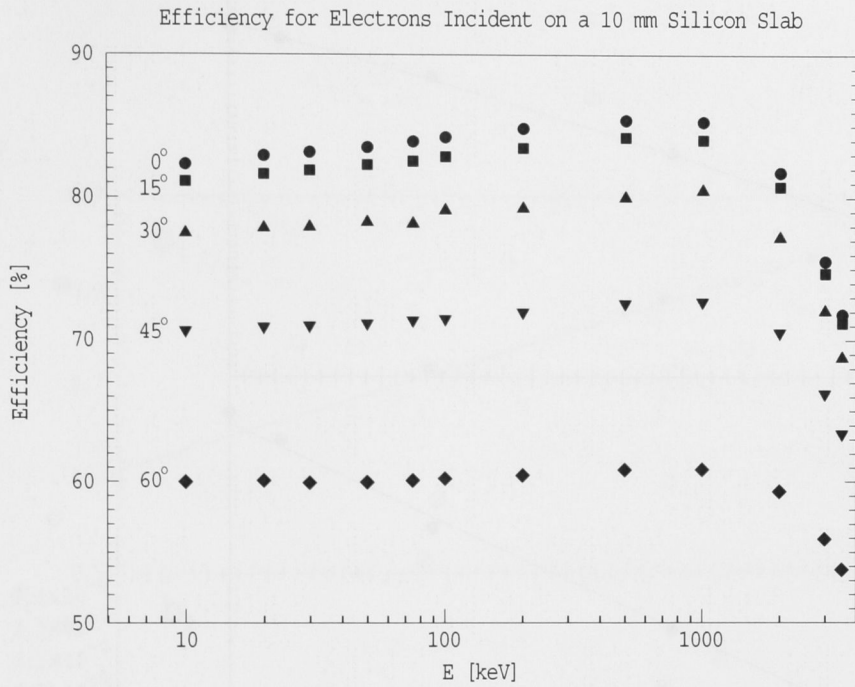


Figure 4.20: Simulated efficiency for electrons incident on a 10 mm silicon slab.

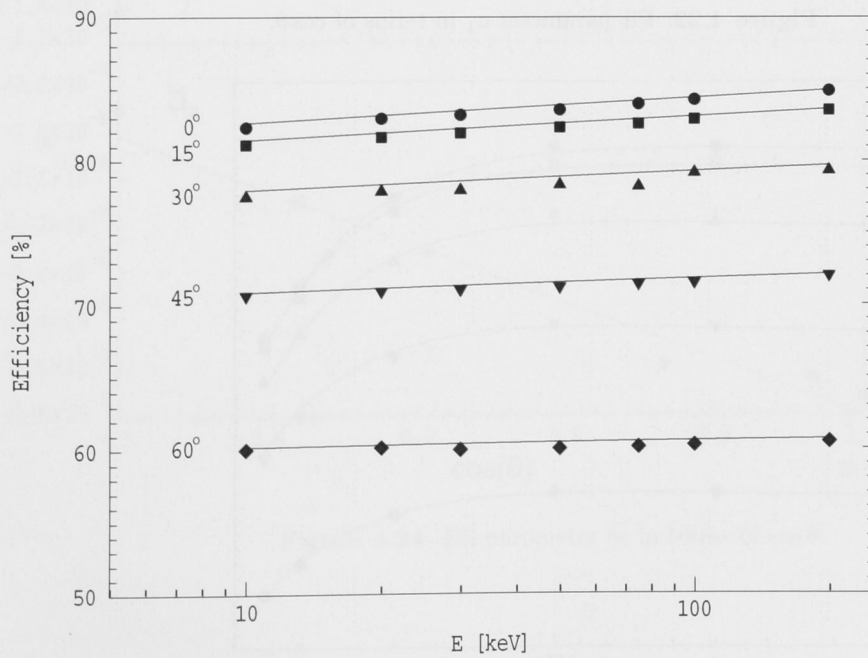


Figure 4.21: Fit to simulation data, from 10 keV to 200 keV.

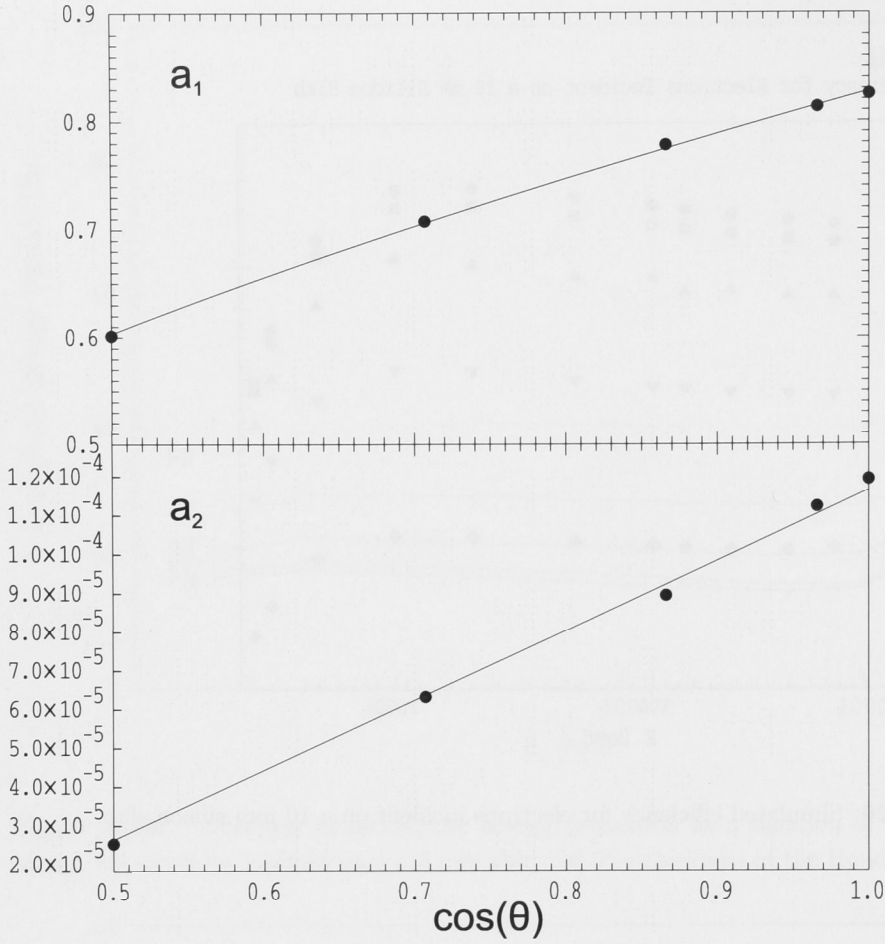


Figure 4.22: Fit parameter  $a_1$  in terms of  $\cos \theta$ .

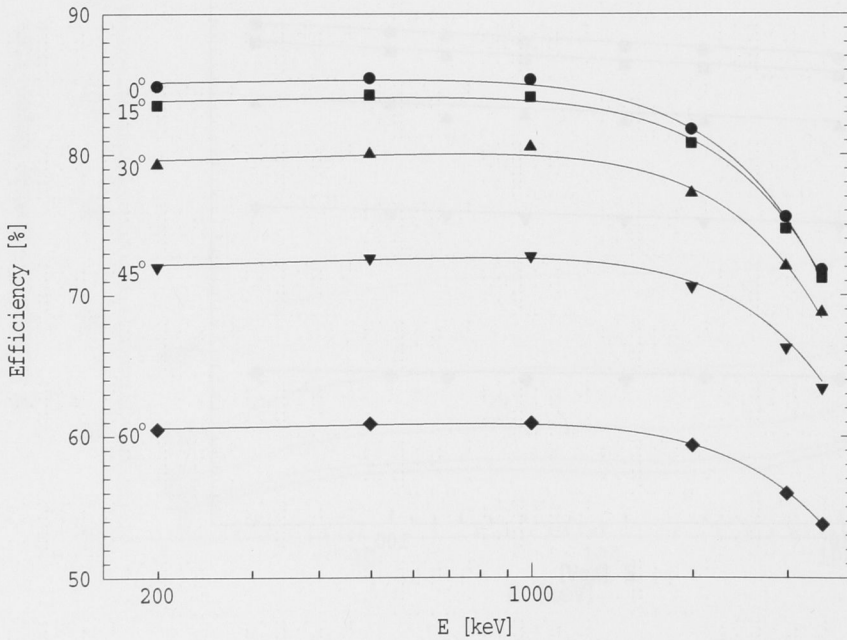


Figure 4.23: Fit to simulation data, from 200 to 3500 keV.

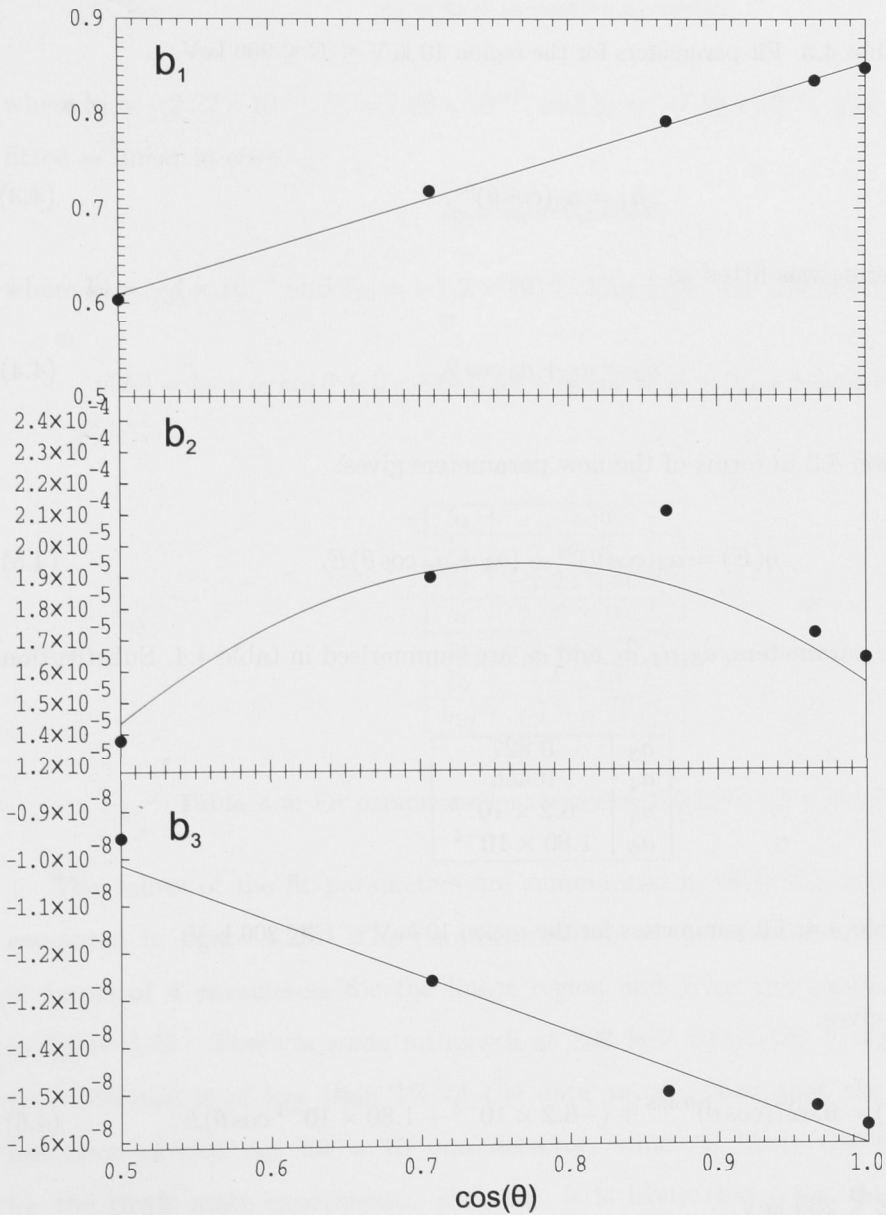


Figure 4.24: Fit parameter  $b_3$  in terms of  $\cos \theta$ .

$\theta$	$a_1$	$a_2$
$0^\circ$	0.8251	$1.206 \times 10^{-4}$
$15^\circ$	0.81326	$1.135 \times 10^{-4}$
$30^\circ$	0.77580	$9.12 \times 10^{-5}$
$45^\circ$	0.707997	$6.49 \times 10^{-5}$
$60^\circ$	0.60137	$2.70 \times 10^{-5}$

**Table 4.3:** Fit parameters for the region  $10 \text{ keV} \leq E \leq 200 \text{ keV}$ .

then fitted as:

$$a_1 = a_3(\cos \theta)^{a_4} \quad (4.3)$$

and the parameter  $a_2$  was fitted as

$$a_2 = a_5 + a_6 \cos \theta. \quad (4.4)$$

Re-writing equation 4.2 in terms of the new parameters gives:

$$\eta(E) = a_3(\cos \theta)^{a_4} + (a_5 + a_6 \cos \theta)E. \quad (4.5)$$

The values of the parameters,  $a_3, a_4, a_5$  and  $a_6$  are summarised in table 4.4. Substitution

$a_3$	0.827
$a_4$	0.456
$a_5$	$-6.2 \times 10^{-3}$
$a_6$	$1.80 \times 10^{-4}$

**Table 4.4:** Fit parameters for the region  $10 \text{ keV} \leq E \leq 200 \text{ keV}$ .

into equation 4.5 gives

$$\eta(E) = 0.827(\cos \theta)^{0.456} + (-6.2 \times 10^{-3} + 1.80 \times 10^{-4} \cos \theta)E, \quad (4.6)$$

where  $10 \text{ keV} \leq E \leq 200 \text{ keV}$ .

Region two ( $200 \text{ keV} \leq E \leq 3.5 \text{ MeV}$ ) was fitted, see figure 4.23, as:

$$\eta(E) = b_1 + b_2E + b_3E^2, \quad (4.7)$$

where  $b_1, b_2$  and  $b_3$  are the quadratic fit parameters. The parameter  $b_1$  was then fitted as

a linear function of  $\cos \theta$ :

$$b_1 = b_4 + b_5 \cos \theta, \quad (4.8)$$

with  $b_4 = 0.36$  and  $b_5 = 0.49$ . The parameter  $b_2$  was fitted as a quadratic in  $\cos \theta$  as

$$b_2 = b_6 + b_7 \cos \theta + b_8 \cos^2 \theta, \quad (4.9)$$

where  $b_6 = -2.22 \times 10^{-5}$ ,  $b_7 = 1.09 \times 10^{-4}$ , and  $b_8 = -7.10 \times 10^{-5}$ . The parameter  $b_3$  was fitted as linear in  $\cos \theta$ :

$$b_3 = b_9 + b_{10} \cos \theta, \quad (4.10)$$

where  $b_9 = -4 \times 10^{-9}$  and  $b_{10} = -1.2 \times 10^{-8}$ . This gives, for  $200 \text{ keV} \leq E \leq 3500 \text{ keV}$ :

$$\eta(E) = b_4 + b_5 \cos \theta + (b_6 + b_7 \cos \theta + b_8 \cos^2 \theta)E + (b_9 + b_{10} \cos \theta)E^2. \quad (4.11)$$

$b_4$	0.36
$b_5$	0.49
$b_6$	$-2.22 \times 10^{-5}$
$b_7$	$1.09 \times 10^{-4}$
$b_8$	$-7.10 \times 10^{-5}$
$b_9$	$-4 \times 10^{-9}$
$b_{10}$	$-1.2 \times 10^{-8}$

**Table 4.5:** Fit parameters for the region  $200 \text{ keV} \leq E \leq 3.5 \text{ MeV}$ .

The values of the fit parameters are summarised in table 4.5, and data and fit are compared in figure 4.25. The parameterisation of the detector efficiency is achieved in terms of 4 parameters for the linear region and 7 for the quadratic region shown in figure 4.25. There is some mismatch at 200 keV where the 2 regions overlap, but the difference is of less than 1% of the data value. Note that the parameterisation has been carried out for a 10 mm detector, which is likely the thickness required for the Hoyle state experiment. However, it is likely that other thicknesses could be parameterised with a similar expression. The empirical formula provides a means of interpolating between the data points in angle and energy. It also provides a fast method of computing efficiency for a given energy and angle. This becomes important when the experimental detection system of the  $^{12}\text{C}$  is simulated as a whole, including the angular distribution of emitted radiations, the transport through the magnetic field of the lens, and finally, the interaction with the Si(Li) detector. As the complexity of

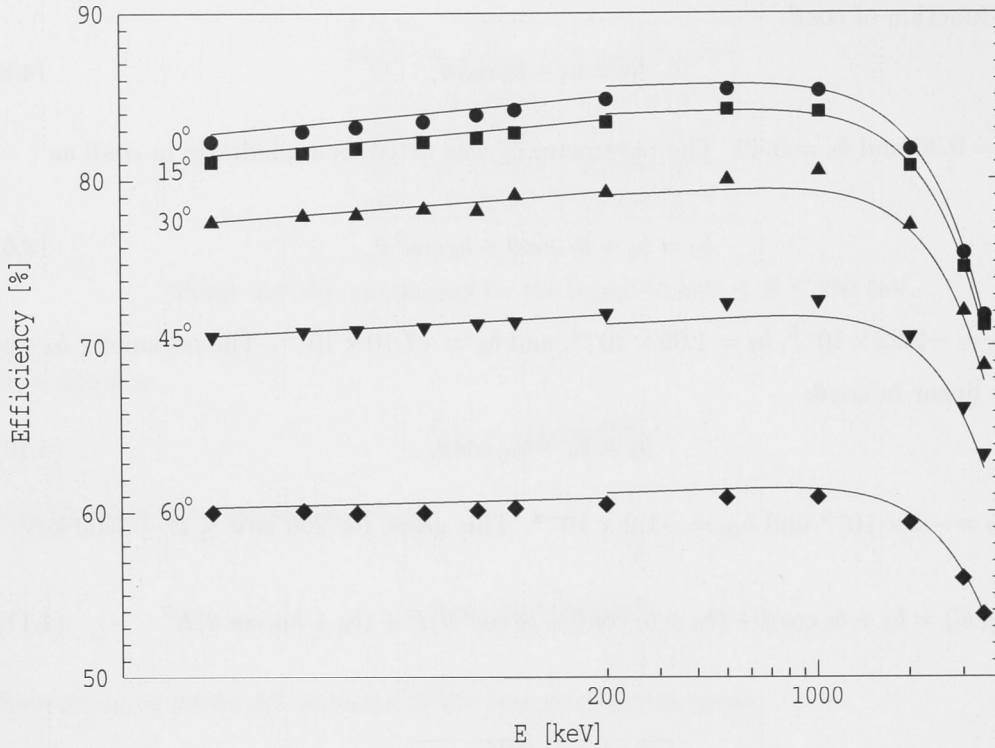


**Figure 4.25:** Fit to efficiency as a function of energy and angle for electrons incident on a 10 mm silicon slab.

the simulated system increases, the empirical formula is a useful tool to improve the simulation speed, and still provides the necessary information. It will also be a goal of future work to integrate the full PENELOPE routine with source and transport simulations.

## 4.6 Future Directions

To improve the agreement between the experimental and simulated  $^{133}\text{Ba}$  spectra, it may be necessary to take a radiograph of the detector, to get a more accurate knowledge of the detector geometry, similar to the approach applied by Mesradi *et al.* [20]. Specifically that would allow us to get a clearer idea of the thickness of the dead layer of silicon and the gold window. Similar methods could also be applied to the source, to get a more accurate source distribution. Also, the accuracy of the simulations could be improved by adding more detail to the geometry file. Several aspects of the geometry were left out to improve simulation speed, such as the cold finger on the back of the detector, electrical connections, and the stainless steel chamber that the



---

apparatus was mounted in. Of these, the vacuum chamber is most likely to have an effect, as all the others are behind the detection area, *i.e.* behind too much material for keV electrons to penetrate through. It is likely though, that some radiations will backscatter from the chamber wall and strike the detector with a depleted energy. The effect would be to raise the background, *i.e.* to lower the peak to background ratio. To simulate this geometry would however require the angle of radiation emission to be increased, preferably to  $360^\circ$ , which would reduce simulation speed by a factor of six.

The empirical formula for the efficiency as a function of energy and angle could be extended to include the detector thickness, which would make the results more widely applicable. As two thicknesses have already been simulated, 3 or 4 more thicknesses could be enough to allow the trend to be characterised. This would increase the complexity of the formula, but widen its relevance. It would allow the formula to be used as a quick reference for the design of new detectors, in the absence of a detailed Monte Carlo or experimental study. The number of parameters would increase significantly, but an empirical formulation would remain much faster than a full Monte Carlo simulation. While the empirical formula can be judged as adequate by inspection of figure 4.25, future applications may require a more quantitative evaluation of its accuracy.

Other properties of the detection system could be investigated, such as the magnitude of “cross talk” between the detector segments of the Honey array. The Hoyle state measurement will rely on the ability to detect when radiations strike the detector in coincidence, *i.e.*, when two detector segments are stimulated in quick succession. The principle is that electrons and positrons (which are emitted simultaneously in pair production) of equal energy will take essentially the same time to travel through the transporter and strike the detector within a narrow time window. Radiations which do not satisfy the time conditions will be rejected. Cross talk occurs when a particle strikes one detector and then another detector, depositing some of its energy in each. These events will satisfy the time conditions, but are unwanted background. Simulations could investigate the magnitude of this effect by throwing radiation at only one detector, and counting events in the adjacent detectors. Other properties of interest could be investigated, such as the ability of photons to reach the detector through the lens system.

To investigate further the simulation's reproduction of the experimental lineshape, a measurement could be taken of a single monoenergetic electron line, such as that produced by a synchrotron. The lineshape would be more visible in the absence of background from other source radiations. The setup could be reproduced in the simulations.

This thesis can be regarded as a significant step in the overall project of detector characterisation in order to measure the radiative width of the Hoyle state in  $^{12}\text{C}$ . The scope is the electron detector, and its response to electrons, photons, and positrons. In order to characterise the spectrometer, these results must be combined with the characterisation of transport through the Lens transporter, and with accurate energy and angular correlations of electron-positron pairs. These projects, together with further experimental studies of the system, are being compiled by the research group at the ANU.

---

# Conclusions

---

The outcomes and conclusions of the present studies are summarised as follows:

- *Review of the PENELOPE Monte Carlo program.* A review of the physics of electron, positron and photon interactions in the PENELOPE Monte Carlo program has been completed. Key aspects identified include the rise of the radiative stopping power above 1 MeV.
- *Reproduction of  $^{133}\text{Ba}$  experimental spectra.* The lineshapes, background and efficiencies of an experimental spectrum were reproduced successfully using Monte Carlo methods. The PENELOPE simulations were enhanced by the inclusion of a routine to sample a cylindrical source distribution, and to reproduce the line-broadening effects of semiconductor charge collection effects and electronic noise, allowing accurate reproduction of experimental spectra for both electrons and photons. The modifications have been incorporated in a computationally efficient way, allowing fast and reliable Monte Carlo detector calibration and characterisation. The simulations showed that the inclusion of a silicon dead layer is necessary to reproduce the experimental results. A mismatch of up to 4 keV was seen in the simulated and experimental peak energies at around 45 keV. The origins of this mismatch require further investigation. The excellent agreement at higher energies, though, shows that the simulation system is appropriate for calibration of the pair spectroscopy measurement on  $^{12}\text{C}$ . The agreement for photon radiations was excellent throughout the studied energy range.
- *Incomplete energy deposition simulations and  $^{56}\text{Co}$  spectrum.* As well as demonstrating the accuracy of the modified PENELOPE routine, the  $^{133}\text{Ba}$  spectrum provided insight into the detector response, resolving the overall spectrum into its electron and photon contributions. The characterisation was extended to higher energies through a  $^{56}\text{Co}$  measurement and a series of simulations. Two unexpected and im-

portant results followed from this investigation: first, that the efficiency drops off alarmingly fast above 1 MeV for both 4.3 mm and 10 mm thick detectors; second, that the cause of this efficiency loss is by the transmission of secondary photons, not backscattering. This suggests that electron detectors should be made significantly thicker than the few millimetres needed to stop the electrons, when studying MeV radiations. Specifically, the results show that the 4.3 mm detector (Honey) proposed for the Hoyle state measurement is not ideal, and a much thicker detector would be preferable. As the lens transporter screens most of the photon background, the maximum thickness that could reasonably be achieved would be preferable. The results also raise the possibility of new innovative detector arrays, perhaps using multiple detectors to ‘add back’ signals from escaping photons.

- *Semi-empirical formula for efficiency as a function of energy.* The efficiency of electrons incident on a 1 cm silicon slab was fitted as a function of incident energy and the cosine of the angle of incidence. The fitting was divided into two regions, a region from 10 keV to 200 keV, where the efficiency was fitted as a linear function of energy, and from 200 keV to 3.5 MeV, where the efficiency was fitted as a quadratic function of energy. The fit for the linear region was  $\eta(E) = a_3(\cos\theta)^{a_4} + (a_5 + a_6 \cos\theta)E$ , where  $a_3$ ,  $a_4$ ,  $a_5$  and  $a_6$  are constants summarised in table 4.4. The quadratic region was fitted as

$$\eta(E) = b_4 + b_5 \cos\theta + (b_6 + b_7 \cos\theta + b_8 \cos^2\theta)E + (b_9 + b_{10} \cos\theta)E^2 \quad (5.1)$$

where  $b_4$ ,  $b_5$ ,  $b_6$ ,  $b_7$ ,  $b_8$ ,  $b_9$ , and  $b_{10}$  are constants summarised in table 4.5. The empirical formula can be used to interpolate between the simulated angles of incidence of  $0^\circ$ ,  $15^\circ$ ,  $30^\circ$ ,  $45^\circ$  and  $60^\circ$ . It can also be developed for use as a quick reference for detector design in the absence of a full Monte Carlo run.

To summarise, the research has given deeper insights into silicon detector response to energetic electrons and positrons. Quantitative analysis of detector response, both efficiency and lineshape, was performed. An empirical characterisation of the efficiency response was achieved, to replace time consuming Monte Carlo calculations in future, which will assist in detailed planning for pair spectroscopy with the Honey detector and Lens transporter at the ANU.

---

# Bibliography

---

- [1] J. Baró, J. Sempau, J.M. Fernández-Varea, F. Salvat, *Nucl. Inst. and Meth. in Phys. Res. B* **100**, 31 (1995).
- [2] P.A. Butler, et al., *Phys. Rev. Lett.* **89**, 202501 (2002).
- [3] R.D. Humphreys, et al., *Phys. Rev. C*, **69**, 064324 (2004).
- [4] S.M. Austin, *Nucl. Phys. A*, **758**, 375 (2005).
- [5] P. Navratil, J.P. Vary and B.R. Bassett, *Phys. Rev. Lett.* **84**, 5728 (2000).
- [6] T. Kibédi, R.H. Spear *Atomic Data and Nuclear Data Tables* **89**, 77 (2005).
- [7] T. Kibédi, A.E. Stuchbery, A.N. Wilson, E.B. Norman, and F.E. Wietfeldt, *Australian Research Council DP1096136 Proposal* (2007).
- [8] F. Salvat, J.M. Fernández-Varea, and J. Sempau, *PENELOPE-2006*, OECD, NEA, No. 6222 Barcelona, Spain (2006).
- [9] S. Agostinelli, et al., *Nucl. Inst. and Meth. in Phys. Res. A* **506**, 250 (2003).
- [10] R. Brun, et al., *GEANT3 Users Guide*. CERN, Geneva, (1987).
- [11] J.F. Briemeister, *MNCP-A General Monte Carlo Code for N-Particle Transport*. CERN, Los Alamos, 2nd edition, (1993).
- [12] M. Vilches, S. Garcia-Pareja, R. Guerro, M. Anguino, and A.M. Lallena, *Nucl. Inst. and Meth. in Phys. Res. B* **254**, 219 (2007).
- [13] T. Kibédi, G.D. Dracoulis, A.P. Byrne, and M. Marie-Jeanne, *A multi-detector electron-electron coincidence spectrometer*, to be published.
- [14] Societe D'etude Physique, detector fabrication company, Evry, France.
- [15] L.A. Kulchitsky and G.D. Latyshev, *Phys. Rev.* **61**, 254 (1942).
- [16] A.O. Hanson, L.H. Lanzl, E.M. Lyman, and M.B. Scott, *Phys. Rev.* **84**, 634 (1951).

- [17] W. Palmberg and T.N. Rhodin, *J. Appl. Phys.* **39**, 2425 (1968).
- [18] M.P. Seah, *Surf. Sci.*, **32**, 703 (1972).
- [19] I.O.B. Ewa, D. Bodizs, S. Czifrus, and Z. Molnar, *App. Rad. and Iso.* **55**, 103 (2001).
- [20] M. Mesradi, A. Elanique, A. Nourreddine, A. Pape, D. Raiser, and A. Sellam, *App. Rad. and Iso.* **66**, 780 (2008).
- [21] A. Jablonski and C.J. Powell, *Surf. Sci.* **601**, 965 (2007).
- [22] C.J. Powell, *Prog. Surf. Sci.* **74**, 357 (2003).
- [23] A. Dubus and A. Jablonski, *J. Phys. Chem. Ref. Dat.* **28**, 19 (1999).
- [24] C. Tur, et al., *Nucl. Inst. and Meth. in Phys. Res. A* **594**, 66 (2008).
- [25] R.D Page, et al., *Nucl. Inst. and Meth. in Phys. Res. B* **204**, 634 (2003).
- [26] P.A Butler, et al., *Nucl. Inst. and Meth. in Phys. Res. A* **381**, 433 (1996).
- [27] M.P. Metlay, J.X. Saladin, I.Y. Lee, and O. Dietzsch *Nucl. Instr. and Meth. in Phys. Res. A* **336**, 162 (1993).
- [28] R.D. Herzberg, et al., *Phys. Rev. C* **65**, 014303 (2001).
- [29] J.E. Bastin, et al., *Phys. Rev. C* **73**, 024308 (2006).
- [30] P.T. Greenless, et al., *Eur. Phys. J. A* **20**, 87 (2004).
- [31] W. Shockley, *Jour. of Appl. Phys.* **9**, 635 (1938).
- [32] G.F. Knoll, *Radiation Detection and Measurement* Wiley & Sons, New York, 3rd edition (2000).
- [33] J. Kantele, *Handbook of Nuclear Spectrometry* London and Academic Press (1995).
- [34] T. Kibédi, G.D. Dracoulis, and A.P. Byrne, *An improved high voltage barrier*, to be published.
- [35] T. Kibédi, G.D. Dracoulis, and A.P. Byrne, *Nucl. Inst. and Meth. in Phys. Res. A* **294**, 523 (1990).
- [36] C.M. Baglin and T.D. MacMahon, Bnm-lnhb/cea-table de radionucléides (2005).

- 
- [37] J. Huo, *Nucl. Data Sheets A* **86**, 315 (1999).
- [38] V.P. Chechev and N.K. Kuzmenko, BNM-LNHB/CEA - Table de Radionucléides (2004).
- [39] S. Rab, *Nucl. Data Sheets* **75**, 491 (1995).
- [40] T. Kibédi, T.W. Burrows, M.B. Trzhaskovskaya, P.M. Davidson, and C.W. Nestor Jr, *Nucl. Instr. and Meth. in Phys. Res. A* **589**, 202 (2008).
- [41] E. Browne and R. B. Firestone, *Table of Radioactive Isotopes*, Wiley & Sons (1986).
- [42] ICRU Report 37 *Stopping Powers for Electrons and Positrons* (1984).
- [43] T. Kibédi, G.D. Dracoulis, and A.P. Byrne, *Nucl. Instrum. Methods in Phys. Res. A* **294**, 523 (1990).
- [44] C.M. Baglin and T.D. MacMahon, Bnm-lnhb/cea-table de radionucléides (2005).
- [45] N.F. Mott and Q.S.W. Massey, *The Theory of Atomic Collisions*, Oxford University Press, London (1965).
- [46] J.P. Desclaux, *Comp. Phys. Comm.* **9**, 31 (1975).
- [47] B. Hahn, D.G. Ravenhall, and R. Hopstadter, *Phys. Rev.* **101**, 1131 (1956).
- [48] F. Salvat, A. Jablonski, and C.J. Powell, *Comp. Phys. Comm.* **165**, 157 (2005).
- [49] A. Jablonski, F. Salvat, and C.J. Powell, *Surf. Int. An.* **37**, 1115 (2005).
- [50] D.W. Walker, *Adv. Phys.* **20**, 257 (1971).
- [51] M. Inokuti, *Rev. Mod. Phys.* **43**, 3 (1971).
- [52] R.M. Sternheimer, S.M. Seltzer, and M.J. Berger *Phys. Rev. B* **26**, 6067 (1982).
- [53] U. Fano, *National Bureau of Standards and Washington and D.C.* (1963).
- [54] E. Rutherford, *Phil. Mag.* **21**, 669 (1911).
- [55] E.J. Williams, *Rev. Mod. Phys.* **17**, 217 (1945).
- [56] U. Fano, *Ann. Rev. Nucl. Sci.* **13**, 1 (1963).
- [57] H.S.W. Massey and C.B.O. Mohr, *Proc. Roy. Soc. A* **132**, 605 (1931).

- [58] M.C. Walske, *Phys. Rev.* **88**, 1283 (1952).
- [59] N. Bohr, *Phil. Mag.* **30** (1915).
- [60] D. Liljequist, *J. Phys. D* **16**, 1567 (1983).
- [61] S.M. Seltzer and M.J. Berger, *J. Appl. Rad. Isot.* **33**, 11 (1982).
- [62] E. Shiles, T. Sazakai, M. Inokuti, and D.Y. Smith, *Phys. Rev. B* **22**, 1612 (1980).
- [63] F. Salvat and R. Mayol, *Comp. Phys. Comm.* **62**, 65 (1991).
- [64] D.E. Cullen, M.H. Chen, J.H. Hubbell, S.T. Perkins, E.F. Plechaty, J.A. Rathkopf, and J.H. Scofield. *Tables and graphs of photon-interaction cross sections from 10 eV to 100 GeV derived from the LLNL evaluated photon data library*. Technical report, EPDL (1989).
- [65] R. Hippler, *Phys. Lett. A* **144**, 81 (1990).
- [66] H.I. Tobehn, F. Ebel, and R. Hippler, *Phys. Rev. Lett.* **71**, 2707 (1993).
- [67] H.A. Bethe and W. Heitler, *Proc. R. Soc. A* **146**, 83 (1934).
- [68] Y.S. Tsai, *Rev. Mod. Phys.* **46**, 815 (1974).
- [69] M.J. Berger and S.M. Seltzer, *Stopping power of electrons and positrons, Report NBSI.*, pages 82–2550 (1982).
- [70] R.H. Pratt, H.K. Lee, C.M. Tseng, L. Kissell, C. MacCallum, and M. Riley, *At. and Nucl. Dat. Tab.* **20**, 175 (1977).
- [71] L. Kim, R.H. Pratt, S.M. Seltzer, and M.J. Berger, *Phys. Rev. A* **33**, 3002 (1986).
- [72] L. Kissel, C.A. Quarles, and R.H. Pratt, *Phys. Rev.* **28**, 92 (1983).
- [73] P. Kirkpatrick and L. Wiedmann, *Phys. Rev.* **67**, 321 (1945).
- [74] P.J. Statham, *X-Ray Spect.* **5**, 154 (1976).
- [75] W. Heitler, *The Quantum Theory of Radiation* Constable and Co., UK (1954).
- [76] W.R. Nelson, H. Hirayama, and D.W.O. Rogers, The EGS4 code system, *Report SLAC-265 Stanford Linear Accelerator Center and Stanford and CA* (1985).
- [77] M. Born, *Atomic Physics* Blackie & Son, London (1969).



- 
- [78] J. Barò, M. Roteta, J.M. Fernández-Varea, and F. Salvat, *Radiat. Phys. Chem.* **44**, 531 (1994).
- [79] C.M. Lederer and V.S. Shirley, *Table of Isotopes* Wiley & Sons, New York, 7th edition (1978).
- [80] E.B. Saloman, J.H. Hubbell and J.H. Scofield, *At. and Nucl. Data Tables* **38**, 1 (1988).
- [81] N. Bohr, *Xcom: Photon cross sections on a personal computer* (1987).
- [82] J.J. Thomson, *The Conduction of Electricity through gases* University Press (1906).
- [83] A. Grau-Carles and K. Kossert, *App. Rad. and Iso.* **67**, 192 (2009).
- [84] A.K. Inoyatov, D.V. Filosofov, L.L. Perevoschikov, A. Kovalik, V.M. Gorozhankin and T. Vylov, *J. El. Spec. and Rel. Phen.* **168**, 20 (2008).
- [85] M.J. Berger, *Monte Carlo calculation of the penetration and diffusion of fast charged particles*, volume 1, Academic Press, New York (1963).
- [86] P. Bratley, B.L. Fox and L.E. Schrage, *A Guide to Simulation* Springer-Verlag, New York N.Y., 2nd edition (1987).
- [87] T. Kibédi. *Fitek*, ANU (1997).
- [88] M. Mesradi, A. Elanique, A. Nourreddine, A. Pape, D. Raiser, and A. Sellam. *App. Rad. and Iso.* **66**, 780 (2008).
- [89] G. Kalinka, *Nuclear Instruments and Methods in Physics Research B* **88**, 470 (1994).





```
SURFACE ( 10) Plane Z=-0.00 Front
INDICES=( 0, 0, 0, 1, 0)
00000000000000000000000000000000000000000000000000000000000000000000
SURFACE ( 11) Cylinder R X=0.0+2e6
INDICES=( 1, 1, 0, 0,-1)
X-SCALE=( 3.300000000000000E+00, 0)
Y-SCALE=( 3.300000000000000E+00, 0)
00000000000000000000000000000000000000000000000000000000000000000000
SURFACE ( 12) Plane Z=-0.07 Cu Back
INDICES=( 0, 0, 0, 1, 0)
Z-SHIFT=( 1.250000000000000E+00, 0)
00000000000000000000000000000000000000000000000000000000000000000000
SURFACE ( 13) Plane Z=-.069998 Gold Plating (front)
INDICES=( 0, 0, 0, 1, 0)
Z-SHIFT=( 0.069998000000000E+00, 0)
00000000000000000000000000000000000000000000000000000000000000000000
SURFACE ( 14) Plane Z=-.28 Si side (front)
INDICES=( 0, 0, 0, 1, 0)
Z-SHIFT=( 0.280000000000000E+00, 0)
00000000000000000000000000000000000000000000000000000000000000000000
SURFACE ( 15) Plane Z=-.28 Si side (front)
INDICES=( 0, 0, 0, 1, 0)
THETA=( 9.000000000000000E+01, 0) DEG
00000000000000000000000000000000000000000000000000000000000000000000
SURFACE ( 16) Plane X=5.522319124 Gap A-B
INDICES=( 0, 0, 0, 1, 0)
THETA=( 9.000000000000000E+01, 0) DEG
PHI=(-6.000000000000000E+01, 0) DEG
00000000000000000000000000000000000000000000000000000000000000000000
SURFACE ( 17) Plane Z=-0.07 Back Source
INDICES=( 0, 0, 0, 1, 0)
Z-SHIFT=(-5.000000000000000E+00, 0)
00000000000000000000000000000000000000000000000000000000000000000000
SURFACE ( 18) Plane Z=-0.00 Front Source
INDICES=( 0, 0, 0, 1, 0)
Z-SHIFT=(-4.999995600000000E+00, 0)
00000000000000000000000000000000000000000000000000000000000000000000
SURFACE ( 19) Cylinder R X=0.0+2e6 Source
INDICES=( 1, 1, 0, 0,-1)
X-SCALE=( 2.000000000000000E-01, 0)
Y-SCALE=( 2.000000000000000E-01, 0)
00000000000000000000000000000000000000000000000000000000000000000000
SURFACE ( 20) Plane Z=-0.07003 Silicon Front
INDICES=( 0, 0, 0, 1, 0)
Z-SHIFT=( 0.070400000000000E+00, 0)
00000000000000000000000000000000000000000000000000000000000000000000
BODY ( 1) Silicon (active)
MATERIAL( 2)
SURFACE ( 20), SIDE POINTER=( 1)
SURFACE ( 2), SIDE POINTER=(-1)
SURFACE ( 3), SIDE POINTER=( 1)
SURFACE ( 4), SIDE POINTER=(-1)
SURFACE ( 5), SIDE POINTER=(-1)
00000000000000000000000000000000000000000000000000000000000000000000
BODY ( 2) Silicon (dead)
MATERIAL( 2)
SURFACE ( 1), SIDE POINTER=( 1)
SURFACE ( 20), SIDE POINTER=(-1)
SURFACE ( 3), SIDE POINTER=( 1)
SURFACE ( 4), SIDE POINTER=(-1)
SURFACE ( 5), SIDE POINTER=(-1)
BODY ( 1)
00000000000000000000000000000000000000000000000000000000000000000000
MODULE ( 3) GOLD
MATERIAL( 3)
SURFACE ( 2), SIDE POINTER=(-1)
SURFACE ( 13), SIDE POINTER=( 1)
SURFACE ( 3), SIDE POINTER=( 1)
SURFACE ( 4), SIDE POINTER=(-1)
SURFACE ( 5), SIDE POINTER=(-1)
```



```

BODY ( 1)
BODY
BODY ( 2) Silicon
MATERIAL ( 3)
SURFACE ( 4) SIDE POINTS= 1
SURFACE ( 5) SIDE POINTS= 2
SURFACE ( 6) SIDE POINTS= 3
SURFACE ( 7) SIDE POINTS= 4
SURFACE ( 8) SIDE POINTS= 5
SURFACE ( 9) SIDE POINTS= 6
BODY ( 10)
BODY
BODY ( 11) Cap
MATERIAL ( 12)
SURFACE ( 13) SIDE POINTS= 1
SURFACE ( 14) SIDE POINTS= 2
SURFACE ( 15) SIDE POINTS= 3
SURFACE ( 16) SIDE POINTS= 4
SURFACE ( 17) SIDE POINTS= 5
MATERIAL ( 18)
BODY ( 19)
BODY
BODY ( 20)
MATERIAL ( 21)
SURFACE ( 22) SIDE POINTS= 1
SURFACE ( 23) SIDE POINTS= 2
SURFACE ( 24) SIDE POINTS= 3
SURFACE ( 25) SIDE POINTS= 4
SURFACE ( 26) SIDE POINTS= 5
MATERIAL ( 27)
BODY ( 28)
BODY
BODY ( 29)
MATERIAL ( 30)
SURFACE ( 31) SIDE POINTS= 1
SURFACE ( 32) SIDE POINTS= 2
SURFACE ( 33) SIDE POINTS= 3
SURFACE ( 34) SIDE POINTS= 4
SURFACE ( 35) SIDE POINTS= 5
MATERIAL ( 36)
BODY ( 37)
BODY
BODY ( 38)
MATERIAL ( 39)
SURFACE ( 40) SIDE POINTS= 1
SURFACE ( 41) SIDE POINTS= 2
SURFACE ( 42) SIDE POINTS= 3
SURFACE ( 43) SIDE POINTS= 4
SURFACE ( 44) SIDE POINTS= 5
MATERIAL ( 45)
BODY ( 46)
BODY
BODY ( 47)
MATERIAL ( 48)
SURFACE ( 49) SIDE POINTS= 1
SURFACE ( 50) SIDE POINTS= 2
SURFACE ( 51) SIDE POINTS= 3
SURFACE ( 52) SIDE POINTS= 4
SURFACE ( 53) SIDE POINTS= 5
MATERIAL ( 54)
BODY ( 55)
BODY
BODY ( 56)
MATERIAL ( 57)
SURFACE ( 58) SIDE POINTS= 1
SURFACE ( 59) SIDE POINTS= 2
SURFACE ( 60) SIDE POINTS= 3
SURFACE ( 61) SIDE POINTS= 4
SURFACE ( 62) SIDE POINTS= 5
MATERIAL ( 63)
BODY ( 64)
BODY
BODY ( 65)
MATERIAL ( 66)
SURFACE ( 67) SIDE POINTS= 1
SURFACE ( 68) SIDE POINTS= 2
SURFACE ( 69) SIDE POINTS= 3
SURFACE ( 70) SIDE POINTS= 4
SURFACE ( 71) SIDE POINTS= 5
MATERIAL ( 72)
BODY ( 73)
BODY
BODY ( 74)
MATERIAL ( 75)
SURFACE ( 76) SIDE POINTS= 1
SURFACE ( 77) SIDE POINTS= 2
SURFACE ( 78) SIDE POINTS= 3
SURFACE ( 79) SIDE POINTS= 4
SURFACE ( 80) SIDE POINTS= 5
MATERIAL ( 81)
BODY ( 82)
BODY
BODY ( 83)
MATERIAL ( 84)
SURFACE ( 85) SIDE POINTS= 1
SURFACE ( 86) SIDE POINTS= 2
SURFACE ( 87) SIDE POINTS= 3
SURFACE ( 88) SIDE POINTS= 4
SURFACE ( 89) SIDE POINTS= 5
MATERIAL ( 90)
BODY ( 91)
BODY
BODY ( 92)
MATERIAL ( 93)
SURFACE ( 94) SIDE POINTS= 1
SURFACE ( 95) SIDE POINTS= 2
SURFACE ( 96) SIDE POINTS= 3
SURFACE ( 97) SIDE POINTS= 4
SURFACE ( 98) SIDE POINTS= 5
MATERIAL ( 99)
BODY ( 100)
BODY

```

---

# PENELOPE Input File for the <sup>133</sup>Ba Electron Measurement

---

```

TITLE 133Ba electron emissions with 4.3 mm Honey detector
      . Alan Devlin alan.devlin@anu.edu.au 6/6/2009
>>>>>>> Source definition.
SKPAR 1 [Primary particles: 1=electron, 2=photon, 3=positron]
      . Energies in eV
SPECTR 25.105e3 9.3 [Auger KLL E bin: lower-end and total probabill
SPECTR 25.105e3 -1.0e0
SPECTR 29.98e3 4.39 [Auger K LX]
SPECTR 29.98e3 -1.0e0
SPECTR 34.73e3 0.517 [Auger K XY]
SPECTR 34.73e3 -1.0e0
SPECTR 17.18e3 10.30 [53 K]
SPECTR 17.18e3 -1.0e0
SPECTR 47.61e3 1.8 [53 L]
SPECTR 47.61e3 -1.0e0
SPECTR 52.20e3 0.46 [53 M]
SPECTR 52.20e3 -1.0e0
SPECTR 43.63e3 3.96 [80 K]
SPECTR 43.63e3 -1.0e0
SPECTR 73.98e3 0.575 [80 L]
SPECTR 73.98e3 -1.0e0
SPECTR 78.62e3 0.147 [80 M]
SPECTR 78.62e3 -1.0e0
SPECTR 45.01e3 47.0 [81 K]
SPECTR 45.01e3 -1.0e0
SPECTR 75.38e3 7.04 [81 L]
SPECTR 75.38e3 -1.0e0
SPECTR 80.01e3 1.803 [81 M]
SPECTR 80.01e3 -1.0e0
SPECTR 124.63e3 0.149 [161 K]
SPECTR 124.63e3 -1.0e0
SPECTR 155.14e3 0.0300 [161 L]
SPECTR 155.14e3 -1.0e0
SPECTR 159.67e3 0.0078 [161 M]
SPECTR 159.67e3 -1.0e0
SPECTR 187.25e3 0.0379 [223 K]
SPECTR 187.25e3 -1.0e0
SPECTR 217.56e3 0.00500 [223 L]
SPECTR 217.56e3 -1.0e0
SPECTR 222.23e3 0.00127 [223 M]
SPECTR 222.23e3 -1.0e0
SPECTR 240.41e3 0.330 [276 K]
SPECTR 240.41e3 -1.0e0 [276 L]
SPECTR 270.90e3 0.0603 [276 M]
SPECTR 270.90e3 -1.0e0
SPECTR 275.44e3 0.0156 [276 M]
SPECTR 275.44e3 -1.0e0
SPECTR 266.87e3 0.684 [303 K]
SPECTR 266.87e3 -1.0e0
SPECTR 297.16e3 0.0887 [303 L]
SPECTR 297.16e3 -1.0e0

```

```

SPECTR 301.84e3 0.0225 [303 M]
SPECTR 301.84e3 -1.0e0
SPECTR 320.03e3 1.309 [356 K]
SPECTR 320.03e3 -1.0e0
SPECTR 350.47e3 0.215 [356 L]
SPECTR 350.47e3 -1.0e0
SPECTR 355.04e3 0.0553 [356 M]
SPECTR 355.04e3 -1.0e0
SPECTR 347.86e3 0.151 [384 K]
SPECTR 347.86e3 -1.0e0
SPECTR 378.29e3 0.0241 [384 L]
SPECTR 378.29e3 -1.0e0
SPECTR 382.88e3 0.00619 [384 M]
SPECTR 382.88e3 -1.0e0
FWHM 1.0E+3 [FWHM due to electronic noise]
SPOSIT 0 0 -5 [Coordinates of the source]
SRAD 0.15 [Radius of the source]
STHICK 4.4E-6 [Thickness of the source]
SDIREC 0 0 [Beam axis direction angles, in deg]
SAPERT 55 [Beam aperture, in deg]
EPMAX 400e3 [Maximum energy]

>>>>>> Material data and simulation parameters.
NMAT 4 [Number of different materials, .1e.10]
>>>>>> Copper
SIMPAR 1 10.0E+3 10.0E+2 10.0E+3 0.1 0.1 1.0E+3 10.0E+2 [M,EABS,C1,C2,WCC,WCR]
>>>>>> Silicon
SIMPAR 2 1.0E+3 1.0E+2 1.0E+3 0.1 0.1 1.0E+2 1.0E+2 [M,EABS,C1,C2,WCC,WCR]
>>>>>> Gold
SIMPAR 3 1.0E+3 1.0E+2 1.0E+3 0.1 0.1 1.0E+2 1.0E+2 [M,EABS,C1,C2,WCC,WCR]
>>>>>> Source
SIMPAR 4 1.0E+3 1.0E+2 1.0E+3 0.1 0.1 1.0E+2 1.0E+2 [M,EABS,C1,C2,WCC,WCR]
PFNAME Honey.mat [Material definition file, 20 chars]

>>>>>> Geometry definition file.
GEOMFN Sidead.geo [Geometry definition file, 20 chars]
DSMAX 1 1.0e-03 [IB, Maximum step length in body IB]
DSMAX 2 1.0e-08 [IB, Maximum step length in body IB]
DSMAX 3 1.0e-08 [IB, Maximum step length in body IB]
DSMAX 4 1.0e+11 [IB, Maximum step length in body IB]
DSMAX 5 1.0e+11 [IB, Maximum step length in body IB]
DSMAX 6 1.0e+11 [IB, Maximum step length in body IB]
DSMAX 7 1.0e-03 [IB, Maximum step length in body IB]
DSMAX 8 1.0e-08 [IB, Maximum step length in body IB]
DSMAX 9 1.0e-08 [IB, Maximum step length in body IB]
DSMAX 10 1.0e+11 [IB, Maximum step length in body IB]
DSMAX 11 1.0e+11 [IB, Maximum step length in body IB]
DSMAX 12 1.0e+11 [IB, Maximum step length in body IB]
DSMAX 13 1.0e-03 [IB, Maximum step length in body IB]
DSMAX 14 1.0e-08 [IB, Maximum step length in body IB]
DSMAX 15 1.0e-08 [IB, Maximum step length in body IB]
DSMAX 16 1.0e+11 [IB, Maximum step length in body IB]
DSMAX 17 1.0e-6 [IB, Maximum step length in body IB]
DSMAX 18 1.0e+11 [IB, Maximum step length in body IB]
DSMAX 19 1.0e-03 [IB, Maximum step length in body IB]
DSMAX 20 1.0e-08 [IB, Maximum step length in body IB]
DSMAX 21 1.0e-08 [IB, Maximum step length in body IB]
DSMAX 22 1.0e+11 [IB, Maximum step length in body IB]
DSMAX 23 1.0e+11 [IB, Maximum step length in body IB]
DSMAX 24 1.0e+11 [IB, Maximum step length in body IB]
DSMAX 25 1.0e-03 [IB, Maximum step length in body IB]
DSMAX 26 1.0e-08 [IB, Maximum step length in body IB]
DSMAX 27 1.0e-08 [IB, Maximum step length in body IB]
DSMAX 28 1.0e+11 [IB, Maximum step length in body IB]
DSMAX 29 1.0e+11 [IB, Maximum step length in body IB]

```



```
DSMAX 30 1.0e+11 [IB, Maximum step length in body IB]
DSMAX 31 1.0e-03 [IB, Maximum step length in body IB]
DSMAX 32 1.0e-08 [IB, Maximum step length in body IB]
DSMAX 33 1.0e-08 [IB, Maximum step length in body IB]
DSMAX 37 1.0e-10 [IB, Maximum step length in body IB]
.
>>>>>> Emerging particles. Energy and angular distributions.
NBE 1e3 400e3 800 [E-interval and no. of energy bins]
NBTH 45 [No. of bins for the polar angle THETA]
NBPH 18 [No. of bins for the azimuthal angle PHI]
.
>>>>>> Energy deposition detectors (up to 25).
ENDDET 1e3 400e3 800 [Energy window and number of channels]
EDSPC pm-spc-enddet-01.dat
EDBODY 1 [Active body; one line for each body]
EDBODY 7 [Active body; one line for each body]
EDBODY 13 [Active body; one line for each body]
EDBODY 19 [Active body; one line for each body]
EDBODY 25 [Active body; one line for each body]
EDBODY 31 [Active body; one line for each body]
ENDDET 1e2 1000e2 1000 [Energy window and number of channels]
EDBODY 37
.
>>>>>> Job properties
DUMPTO dump1.dat [Generate this dump file, 20 chars]
DUMPP 60 [Dumping period, in sec]
.
>>>>>>
NSIMSH 1e9 [Desired number of simulated showers]
TIME 1e8
```



# PENELOPE Output File

```
*****
**   Program PENMAIN. Results.   **
*****
```

```
Simulation time ..... 4.497899E+03 sec
Simulation speed ..... 2.223260E+02 showers/sec
```

```
Simulated primary showers ..... 1.000000E+06
```

```
Transmitted primary particles ..... 0.000000E+00
Backscattered primary particles ..... 1.632580E+05
Absorbed primary particles ..... 8.367420E+05
```

```
Fractional transmission ..... 0.000000E+00 +- 0.0E+00
Fractional backscattering ..... 1.689480E-01 +- 1.3E-03
Fractional absorption ..... 8.367420E-01 +- 1.1E-03
```

Secondary-particle generation probabilities:

	electrons	photons	positrons
transmitted	0.000000E+00 +- 0.0E+00	1.460000E-04 +- 3.6E-05	0.000000E+00 +- 0.0E+00
backscattered	5.690000E-03 +- 2.3E-04	6.381000E-03 +- 2.4E-04	0.000000E+00 +- 0.0E+00
absorbed	1.650730E+01 +- 1.7E-02	9.698800E-02 +- 9.4E-04	0.000000E+00 +- 0.0E+00

Average deposited energies (bodies):

```
Body 1 ..... 9.002142E+04 +- 7.2E+01 eV (effic. = 3.16E+03)
```

Average deposited energies (energy detectors):

```
Detector # 1 ... 9.002142E+04 +- 7.2E+01 eV (effic. = 3.16E+03)
```

```
Last random seeds = 1 , 2
```

The secondary particle probabilities should be multiplied by the number of simulated primary showers (in this case  $1 \times 10^6$ ) to obtain absolute particle numbers. It should be noted that a single shower may transmit or backscatter more than one secondary particle. The numbers of absorbed secondary particles are much higher than the input primary showers as in general a single primary particle will generate a multitude of secondary particles.

Appendix C

# PENELOPE Output File

\*\*\*\*\*  
\* PENELOPE OUTPUT \*  
\*\*\*\*\*

Simulation name : .....

Simulation time : .....

Simulation date : .....

Simulation path : .....

Particle	Energy (MeV)	Number	Weight
Electron	0.000000	10000000	1.000000
Positron	0.000000	10000000	1.000000
Neutron	0.000000	10000000	1.000000
Proton	0.000000	10000000	1.000000

Average deposited energy (keV/g) : .....

Average deposited energy (MeV/g) : .....

Average deposited energy (J/kg) : .....

Average deposited energy (Gy) : .....

The secondary particle multiplicities should be multiplied by the number of primary particles shown for the case 1 x 10<sup>7</sup> to obtain absolute particle numbers. It should be noted that a single event may produce an arbitrary number of secondary particles. The number of absorbed secondary particles are much larger than the event number shown so to control a large number of particles will generate a multiplicity of secondary particles.

---

# PENELOPE Output Spectrum File

---

This appendix is an example of a PENELOPE output spectrum file. In this case, there is a peak at 50 keV.

```
# Results from PENMAIN. Output from energy-deposition detector # 1
# WARNING: May be strongly biased if interaction forcing is used!
# 1st column: deposited energy (eV).
# 2nd column: probability density (1/(eV*particle)).
# 3rd column: statistical uncertainty (3 sigma).

5.000000E+02 1.995000E-06 1.338625E-07
1.500000E+03 2.394000E-06 1.466097E-07
2.500000E+03 2.704000E-06 1.557889E-07
3.500000E+03 3.173000E-06 1.687198E-07
4.500000E+03 3.388000E-06 1.743235E-07
5.500001E+03 3.873000E-06 1.863384E-07
6.500001E+03 4.260000E-06 1.953885E-07
7.500001E+03 4.622000E-06 2.034840E-07
8.500001E+03 4.972000E-06 2.110107E-07
9.500001E+03 5.191999E-06 2.156047E-07
1.050000E+04 5.525999E-06 2.223942E-07
1.150000E+04 5.661999E-06 2.250988E-07
1.250000E+04 5.851999E-06 2.288226E-07
1.350000E+04 5.913999E-06 2.300244E-07
1.450000E+04 6.122999E-06 2.340290E-07
1.550000E+04 6.121999E-06 2.340100E-07
1.650000E+04 5.914999E-06 2.300437E-07
1.750000E+04 5.911999E-06 2.299857E-07
1.850000E+04 5.781999E-06 2.274579E-07
1.950000E+04 5.786999E-06 2.275557E-07
2.050000E+04 5.380999E-06 2.194730E-07
2.150000E+04 5.328999E-06 2.184157E-07
2.250000E+04 5.257999E-06 2.169635E-07
2.350000E+04 5.082999E-06 2.133412E-07
2.450000E+04 4.754000E-06 2.063555E-07
2.550000E+04 4.551000E-06 2.019222E-07
2.650000E+04 4.237000E-06 1.948626E-07
2.750000E+04 4.030000E-06 1.900627E-07
2.850000E+04 3.879000E-06 1.864821E-07
2.950000E+04 3.588000E-06 1.793771E-07
3.050000E+04 3.409000E-06 1.748611E-07
3.150000E+04 3.196000E-06 1.693283E-07
3.250000E+04 2.889000E-06 1.610151E-07
3.350000E+04 2.694000E-06 1.555014E-07
3.450000E+04 2.449000E-06 1.482802E-07
3.550000E+04 2.215000E-06 1.410349E-07
3.650000E+04 2.016000E-06 1.345638E-07
3.750000E+04 1.845000E-06 1.287414E-07
3.850000E+04 1.575000E-06 1.189650E-07
```

---

3.950000E+04	1.429000E-06	1.133253E-07
4.050000E+04	1.295000E-06	1.078884E-07
4.150000E+04	1.126000E-06	1.006111E-07
4.250000E+04	9.889999E-07	9.429844E-08
4.350000E+04	8.259999E-07	8.618502E-08
4.450000E+04	7.249999E-07	8.074818E-08
4.550000E+04	6.439999E-07	7.610694E-08
4.650000E+04	5.319999E-07	6.917696E-08
4.750000E+04	4.600000E-07	6.432802E-08
4.850000E+04	5.216999E-06	2.161204E-07
4.950000E+04	8.226189E-04	1.145972E-06
5.050001E+04	1.000000E-35	1.000000E-35
5.150001E+04	1.000000E-35	1.000000E-35
5.250001E+04	1.000000E-35	1.000000E-35
5.350001E+04	1.000000E-35	1.000000E-35
5.450001E+04	1.000000E-35	1.000000E-35
5.550001E+04	1.000000E-35	1.000000E-35
5.650001E+04	1.000000E-35	1.000000E-35
5.750001E+04	1.000000E-35	1.000000E-35
5.850001E+04	1.000000E-35	1.000000E-35
5.950001E+04	1.000000E-35	1.000000E-35